



HAL
open science

Environmental degradation of nuclear materials: the use of advanced characterization techniques to understand physical and chemical phenomena

Kimberly Colas

► **To cite this version:**

Kimberly Colas. Environmental degradation of nuclear materials: the use of advanced characterization techniques to understand physical and chemical phenomena. Physics [physics]. Université Paris - Saclay, 2022. tel-04551360

HAL Id: tel-04551360

<https://cea.hal.science/tel-04551360>

Submitted on 18 Apr 2024

HAL is a multi-disciplinary open access archive for the deposit and dissemination of scientific research documents, whether they are published or not. The documents may come from teaching and research institutions in France or abroad, or from public or private research centers.

L'archive ouverte pluridisciplinaire **HAL**, est destinée au dépôt et à la diffusion de documents scientifiques de niveau recherche, publiés ou non, émanant des établissements d'enseignement et de recherche français ou étrangers, des laboratoires publics ou privés.



Distributed under a Creative Commons Attribution - NonCommercial - NoDerivatives 4.0 International License



Université Paris-Saclay

Habilitation à Diriger des Recherches

par

Kimberly COLAS

CEA Saclay

Département de Physico Chimie

Service d'Etudes Analytiques et de Réactivité des Surfaces

Laboratoire d'Analyse en Soutien aux Exploitants

Environmental degradation of nuclear materials:
the use of advanced characterization techniques to
understand physical and chemical phenomena

Acknowledgements

Ce paragraphe est en français, car la plupart des personnes avec qui j'ai eu la chance de travailler lors de ces 10 années de recherche au CEA sont en France ou francophones.

Lors de la rédaction de ce manuscrit d'HDR, j'ai eu le sentiment de revivre mes 10 années de recherche au Service d'Etude des Matériaux Irradiés, un peu comme on voit sa vie défiler devant soi. Ça a été l'occasion de me remémorer d'excellents moments ainsi que des passages plus compliqués. Je souhaite, par ce paragraphe, remercier les personnes qui ont rendu ces moments si particuliers ! Au Laboratoire de Microscopie et d'Etude de l'Endommagement, j'ai eu la chance d'être recrutée par Philippe Bossis qui m'a confié des actions de recherche très intéressantes et avec qui les échanges sont toujours passionnants (que l'on parle de zirconium ou de football). J'ai fait de belles rencontres dans ce labo, notamment celles de la SAT-Team : Anabelle Lopez, Coraline Hossepied et Véronique Clouté-Cazalaa, qui sont des personnes que je suis heureuse d'avoir comme amies. Quelle aventure cette SAT ! Je voudrai aussi remercier le soutien moral sans faille de Fabienne Chamiot et de Bénédicte Verhaeghe ainsi qu'à l'énergie rayonnante de Caroline Bisor. Merci à la fine équipe de métallo et microscopie pour tout ce que vous m'avez appris : Olivier Rabouille, Hawa Bouyssou, Catherine Dessrouer, Marie Azera, Caroline Mallet, Barbara Dhé, Didier Bossu. Merci à mes compagnons de la corrosion pour tous les échanges et les projets passionnants dans lesquels on s'est embarqués ensemble (je ne suis pas prête d'oublier les manipis synchrotron enceinte à Chicago ni les longues nuits au Synchrotron Soleil !) : Marc Tupin, Michaël Jublot et Pierre Billaud. Merci à Bénédicte Kapusta qui m'a tant appris sur l'aluminium ! Merci également aux collègues du DMN avec qui les échanges étaient toujours enrichissants : Estelle Meslin, France Dalle, Denis Menut, Raphaëlle Guillou, Jean-Luc Béchade, Fabien Onimus, Jean-Christophe 'Chrome' Brachet, Claire Ritter, Thomas Le Jolu, Quentin Auzoux, Matthew Bono, Philippe Grange, Damien Schildknecht, Lionel Séjourné, Justin Pageot, Luc Belin, Elodie Rémy, Laurent Veiller.

Bien sûr, rien de ce qui est dans ce manuscrit n'aurait été possible sans les thésards avec qui j'ai pu travailler. Ils m'ont tant appris, apporté de l'enthousiasme, de l'envie, des découvertes. C'était un privilège de vous côtoyer : Sarah L'Haridon-Quaireau (et sa phase mystère), Victor Garric (et sa souris verte trempée dans l'huile et dans l'eau), Diana Nabhan (et le surnom de Google), Romain Verlet (et ses cartes Magic) et Tom Petit (et son énergie infatigable !).

Merci également au groupe NFIR et aux partenaires de l'I3P ainsi que du projet RJH pour les échanges intéressants et la guidance pour les avancées du projet.

Enfin, je voudrais remercier Roland, mes deux enfants et ma mère pour leur soutien sans faille lors de ces 10 années passées. Ça n'a pas été de tout repos mais on en a vécu des choses !

Table of Content

1	Introduction.....	4
2	Hydriding and corrosion of fuel cladding material.....	7
2.1	Corrosion under irradiation.....	8
2.2	Back-end issues.....	21
2.3	Summary and perspectives of work on zirconium alloys.....	28
3	In-reactor degradation of aluminum alloys.....	31
3.1	Corrosion.....	31
3.2	Evolution of the microstructure of 6061-T6 alloy with thermo-mechanical processing and impact of irradiation. ...	42
3.2.1	Characterization of the nanostructure of the 6061-T6 alloy and impact of ion-irradiation (C. Flament)	44
3.2.2	Impact of Si enrichment on 6061-T6 microstructure and swelling behavior (K. Buchanan)	47
3.2.3	Impact of quenching rate on microstructure and study of void swelling (V. Garric)	52
3.2.4	Understanding the fracture toughness evolution with aging duration and irradiation (T. Petit).....	62
3.2.5	Conclusions on the impact of thermo-mechanical treatment and irradiation on the microstructure and mechanical properties of the 6061-T6 alloy	64
3.3	Conclusions on studies on aluminum alloys	65
4	Conclusions and Perspectives.....	68
5	References.....	72
6	Appendices	76
6.1	Detailed Curriculum Vitae	76
6.2	List of publications and communications.....	77

1 Introduction

Many different types of nuclear reactors are currently operating in the world. Nuclear reactors used for civil applications have two main purposes: electricity generation and research. The operating conditions in these reactors vary greatly in terms of temperature, pressure, environment (gaseous, liquid). Thus, the choice of the materials used in these reactors is directly influenced by the conditions in-reactor and eventually the purpose of the reactor itself.

Electricity generating reactors have the purpose of heating a fluid in order to collect the heat produced to activate turbines, which in turn will produce electricity. The large majority of electricity-generating reactors in operation today use water as the fluid that will carry the heat produced by the reaction inside the reactor core. This heat comes from the fission of nuclear fuel, mainly of uranium atoms, which generates heat but also many other types of radiation, X-rays, beta rays, gamma rays, as well as particle emissions such as alpha particles and neutrons for example. The materials used inside a reactor core must withstand very extreme conditions of temperature and irradiation. For the nuclear power plants used in France and in the USA, the two countries where I have conducted most of the research presented in this manuscript, the reactor fuel is made of fuel pellets (uranium or a mix of uranium and plutonium) clad in zirconium rods. These rods are organized in fuel assemblies as illustrated in Figure 1. These fuel assemblies are mostly composed of zirconium components. Approximately 157 fuel assemblies are inserted in the reactor core which is composed of stainless steel alloys. The reactor core is contained in a confinement vessel typically made of austenitic stainless steel as illustrated schematically in Figure 2. Two types of light water reactors exist: pressurized water reactors (PWRs) which operate with circulating water at 315°C and 155 bars and boiling water reactors (BWRs) which operate with circulated water at 285 °C and 75 bars. The entirety of the French fleet of operating reactors today is composed of PWRs while the US fleet is a mixture of both reactor types [1]. My research as a research assistant in graduate school in the US has been focused on material issues occurring in zirconium alloys used in nuclear fuel once the fuel is taken out of the reactor for cooling, transportation and storage. During my time at CEA in the Section for the Study of Irradiated Materials I have also dedicated part of my research on the study of zirconium alloys in particular on in-reactor corrosion and also on the transportation and storage of used nuclear fuel. I will present some of the main finding from this research in Part 2 of this manuscript.

A second purpose of nuclear reactors that was mentioned above is research. This purpose is also combined with the production of isotopes for medical applications. Research reactors can be used to test new materials in order to design safer and more efficient components for electricity-generating reactors. These research reactors are often called Materials Test Reactors (MTRs). Other research reactors are used to study matter by producing neutron fluxes that are guided to experimental stations where the neutrons are used to probe matter. These reactors are used mainly for nuclear physics and studies on the fundamental laws of nature. At the CEA center of Saclay, an MTR, Osiris, was in operation until 2015. A new MTR is currently under construction at the CEA center in Cadarache, the Jules Horowitz Reactor (JHR). A large part of my work while at CEA has been devoted to understanding the behavior of the alloys selected to be used as core components in the JHR. Indeed since research reactors do not have the same purpose than electricity-generating reactors, they also operate under very different conditions. An MTR must have a relatively easily accessible core in order to insert complex experiments (corrosion loops, power ramps, stress devices, etc). They must also irradiate material more intensely and in a shorter time than nuclear power plants in order to observe materials in the most extreme conditions they would meet in operation or under accidental conditions. Finally, since these reactors will not produce electricity, they must be cheaper than nuclear power plants. All these conditions have led to the choice

of operating conditions for the JHR to be: 70°C, 15 bars in the core [2]. The selected material for the fuel is a combination of AlFeNi aluminum-based alloy rolled with U_3Si_2 fuel first then UMo fuel during the following core changes of the reactor. The core internals are in 6061-T6 aluminum alloy. An illustration of the JHR reactor and its key components is presented in Figure 3. The main results from the research performed on this subject at CEA are presented in Part 3 of this manuscript. Most of this work has been done by PhD students, post-doctoral fellows and interns I have supervised or co-supervised.

From the previous paragraph, it can be seen that the operating conditions in a nuclear reactor are varied, depending on the reactor type. Nuclear materials undergoing time in an operating nuclear reactor are subjected to large temperature variations, strain and stress from the environment, and irradiation which lead to microstructural changes and variations in local chemistry. Thus studying nuclear materials will lead to delving into a wide variety of fields of science to answer various questions:

- **Characterization:** what are we looking at? And also how best to look at it? How to protect oneself from radiation and contamination?
- **Mechanical behavior:** will this component break? How long before it breaks and how will it break?
- **Metallurgy and chemistry:** how has the material we are studying changed during its time in reactor?
- **Irradiation and nuclear physics:** what is going through the material in reactor and how is it interacting with the material itself?

From these questions, the problem of characterizing nuclear material arises as one of the main challenges for nuclear material scientists. In my research, many various advanced characterization techniques have been used depending on the problem at hand. In particular, using large user facilities such as synchrotrons and other particle accelerators can be key to study small-scale phenomena with the relevant time and space resolution. Throughout the manuscript, I will emphasize the use of advanced characterization techniques in how they have brought critical information in order to study material behavior for nuclear applications.

The first part of the manuscript focuses on zirconium alloys used as nuclear fuel cladding for light-water reactors. The second part of the manuscript focuses on aluminum alloys used as core internals or fuel cladding for research reactors.

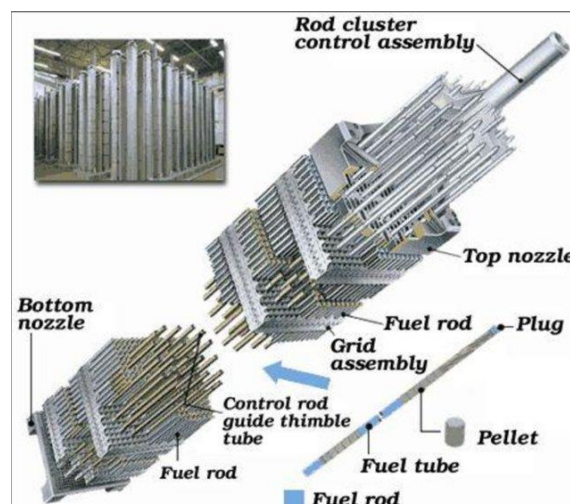


Figure 1 PWR fuel assembly (Mitsubishi Nuclear Fuel) [3]

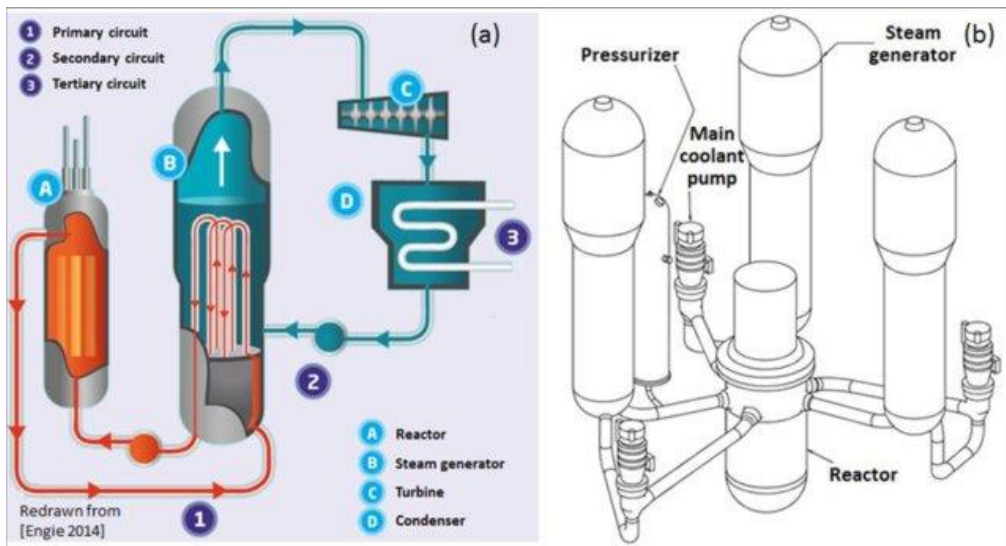


Figure 2 Schematic of a PWR reactor core [4].

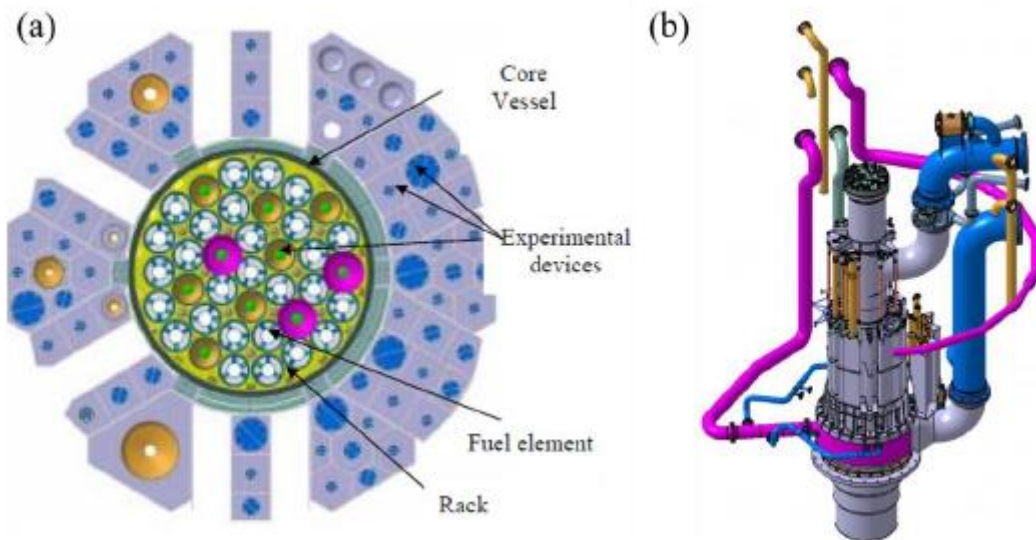


Figure 3 Schematic of JHR reactor core: (a) top cross-section, (b) 3D model [5].

2 Hydriding and corrosion of fuel cladding material

During in-reactor operation, fuel cladding undergoes corrosion. The corrosion reaction takes place at the outer surface of the cladding material where the coolant circulates as illustrated in Figure 4. This corrosion reaction leads to the formation of zirconium oxides as well as the formation of hydrogen following the reaction:



Both corrosion of the cladding and absorption of the formed hydrogen within the cladding impact reactor operation in terms of safety and efficiency. Indeed, the corrosion layer that forms at the surface of fuel rods will degrade the heat transfer between the fuel pellets where the fission reaction occurs and degrade the overall mechanical integrity of the rods. Large corrosion layers can lead to fuel failure and contamination of the primary water circuit in the reactor. The cladding being the first confinement layer from the radioactive fuel, its integrity is crucial for reaction safety. As such, the French Nuclear Safety Authority (ASN) have stated that, for Zircaloy-4 alloys, the maximum oxide thickness acceptable is 100 μm and the maximum hydrogen absorbed into the cladding is 600 wt.ppm.

Part of the hydrogen that has entered the cladding will also diffuse through the cladding and precipitate as zirconium hydrides (see Figure 4). These hydrides are a fragile phase and can significantly embrittle the cladding during operation but mostly once the fuel is removed from the reactor since it is when the fuel is cooled down that most of the hydrogen is precipitated as brittle hydrides.

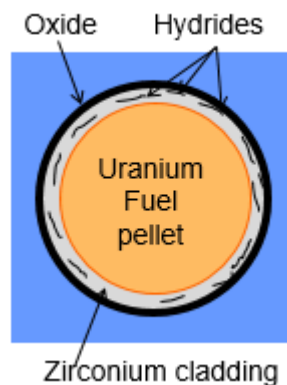


Figure 4 Schematic cut of a fuel rod.

My studies on zirconium fuel cladding have thus concerned two issues occurring at different times in the life of a fuel rod: corrosion during in-reactor operation and hydrogen embrittlement of used fuel during transportation and storage. During the first paragraph of the section, I will present the work performed with PhD students and colleagues at CEA studying corrosion of zirconium alloys and understanding how irradiation during corrosion can affect the corrosion kinetics of the cladding. These studies were performed in partnership with partners from the French nuclear industry with the objective to better predict corrosion behavior but also to develop new zirconium alloys that can minimize this issue in reactor.

The second paragraph of this work will focus on the fuel cladding once it has been removed from the reactor core and cooled. This area of work was my main research focus during my graduate work (Master of Science and PhD) working on unirradiated fuel cladding using synchrotron diffraction to characterize hydriding phenomena. Once at CEA, taking advantage of the ability

to study neutron irradiated fuel, I have continued these studies and will present the work that has been published on this subject during my time as a research engineer and project manager.

2.1 Corrosion under irradiation

As mentioned in the introduction of this paragraph, the corrosion process (oxidation and hydriding) of zirconium alloy cladding is one of the limiting factors of fuel rod lifetime, particularly for Zircaloy-4. The corrosion rate of this material shows a significant acceleration at high burnup in light water reactors as illustrated in Figure 5 [6]. Four major assumptions are proposed in the literature in order to explain this acceleration [7]. The first one is that the hydrides precipitated beneath the metal/oxide interface in the metallic part of the cladding, resulting from the hydrogen uptake by the matrix, may be corroding at a faster rate than the metal itself [8-12]. This assumption may explain only a part of the high burnup acceleration of the alloy. A second assumption assigned the accelerated corrosion to the amorphization and the dissolution of the $Zr(Fe,Cr)_2$ precipitates under irradiation [7, 12, 13]. Other authors suggest that the kinetic acceleration is due to the tin distribution in the alloy in service [14-16]. Indeed, the reduction of tin content in Zircaloy-4 seems to be correlated with a lowering of the corrosion rate of the alloy in PWRs. However, the high burnup corrosion acceleration is also observed on low tin containing samples of Zircaloy-4 which suggests additional mechanisms may play a role. Finally, studies carried out at CEA showed that irradiation in PWR has a strong effect on the oxidation kinetics of Zircaloy-4 claddings. In these studies, irradiation affects all the components: the metal, the oxide layer and the primary coolant. The effect of irradiation of each component on the corrosion rate is not well known up to now. Thus several studies were carried out at CEA to understand the role of irradiation in particular on the oxide and the metal of the cladding. However, studying neutron irradiation effects on corrosion kinetics is very expensive especially if various experiments are to be conducted. Thus the choice of ion irradiation was made, in particular in order to tailor experiments in order to study various phenomena and separate the contributions to oxide kinetic acceleration.

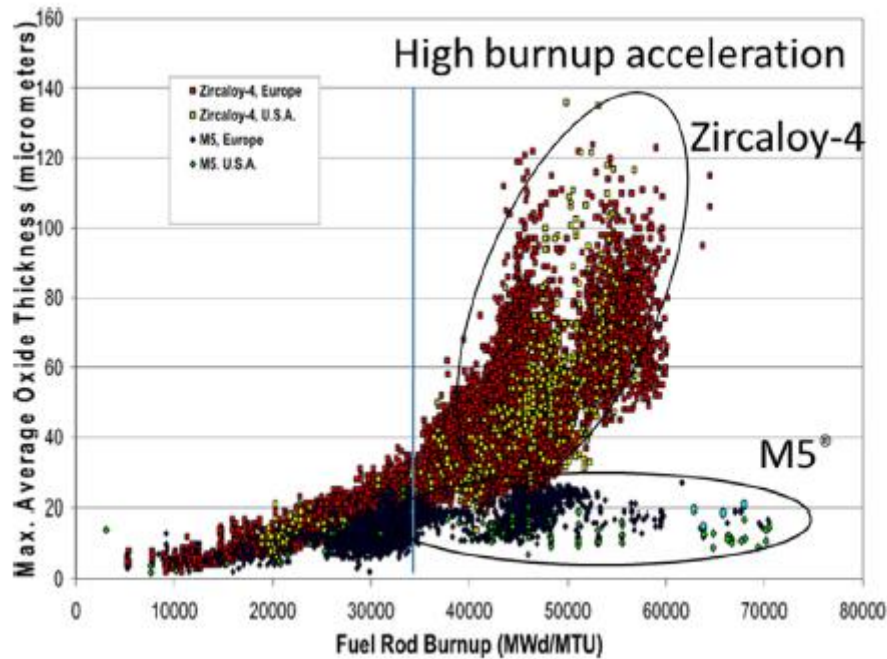


Figure 5 Corrosion performance of alloy M5TM and Zircaloy-4 fuel rods in PWR from [17].

The choice of ion type, energy, and irradiating particle flux will have an impact on the damage created by ion irradiation. Several studies have provided insight on this aspect and allowed us to choose the irradiation conditions to create irradiation damage in the metal without dissolving or amorphizing second-phase precipitates (SPPs) and defects in the oxide without inducing phase transformation.

The first study conducted during Romain Verlet's PhD thesis, focused on the influence of light irradiation of the oxide layer on the oxidation rate of Zircaloy-4 [18, 19]. For this experiment, He ions irradiated the oxide layer uniformly without inducing phase transformation of the oxide. The effect of irradiation on the oxide itself was examined in particular using Raman spectroscopy. The most significant change observed was the emergence of two new vibration bands linked to irradiation defects. Using a specific technique of isotopic exchange of ¹⁸O in the oxide layer followed by SIMS, the diffusion flux could be followed. It has been shown that the flux after irradiation increases with ion fluence leading to an oxygen diffusion rate around 3 times higher than for the non-irradiated material. This modification persists also after at least 10 days in PWR simulated conditions. These results show the existence of a link between the intensities of the two new Raman bands and the flux of ¹⁸O and therefore, the oxidation rate after irradiation. The acceleration of the oxidation rate after irradiation using the kinetic curves has been confirmed as seen in Figure 6. This acceleration lasts up to 23 days and then comes back to the oxidation rate of the non-irradiated Zircaloy-4 alloy when the irradiation defects have been annealed. Finally, a simple model was proposed which describes the kinetic results relatively well as seen in Figure 6.

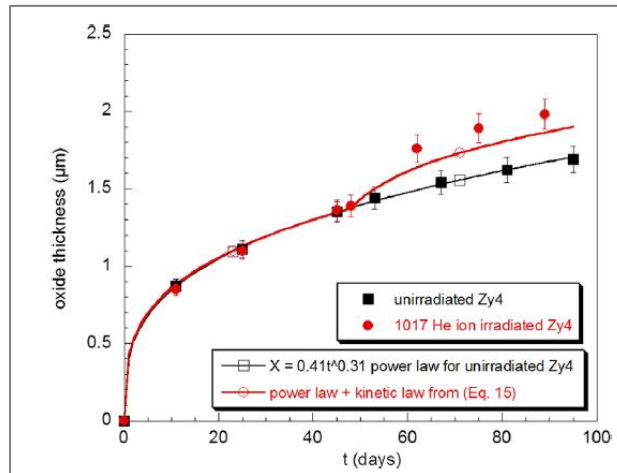


Figure 6 Oxidation kinetics of Zircaloy-4 with (full circles) or without (full squares) irradiation. The black curve with empty squared is a power law fitting of the unirradiated Zy4 kinetics. The red one with empty circles is deduced from the model developed in the paper [18].

The following study focused on the effect of the metal irradiation on the oxidation rate of Zircaloy-4 [20]. Three different types of ion irradiation experiments were conducted in order to separate the effects that may increase the corrosion rate. Thus proton irradiations were performed at 350°C in order to produce $\langle a \rangle$ -type dislocation loops with size and density of the same order than those found in cladding from PWRs. An illustration of the proton irradiation profile, the corrosion kinetics and the corrosion rate for these samples is presented in Figure 7 [20, 21]. As can be seen from this figure, the oxidation rate of the damaged matrix is in this case significantly higher compared to that measured on the unirradiated material.

Zirconium ion irradiation of one sample was carried out at room temperature in order to totally amorphize intermetallic precipitates. In this case, $\langle a \rangle$ -loops were also created but the size and density of the loops are theoretically different (of smaller size and higher density) than those generated by protons at high temperature. Zr ion irradiation at room temperature induces mainly an amorphization of the SPPs. The modification of the crystalline state of the precipitates does not induce a significant change of the oxidation rate of Zircaloy-4.

Finally, iron enrichment in α -Zr matrix was simulated by iron implantation since iron depletion from the SPPs cannot be reproduced with ions. Two fluences of iron ions were chosen to enrich the iron concentration to 0.1 and 0.2 at.% at a depth of 2 μm from the surface. Iron implantation in the matrix does not seem to play a strong role on the corrosion rate.

In the end, three tracks of interpretation of proton irradiation effects have been discussed (chemical effect, mechanical impact and an irradiation effect on the crystal state of the oxide). To validate one of these interpretations, loop size, loop density, irradiation hardening as well as the crystal state of the oxide have to be investigated in more details.

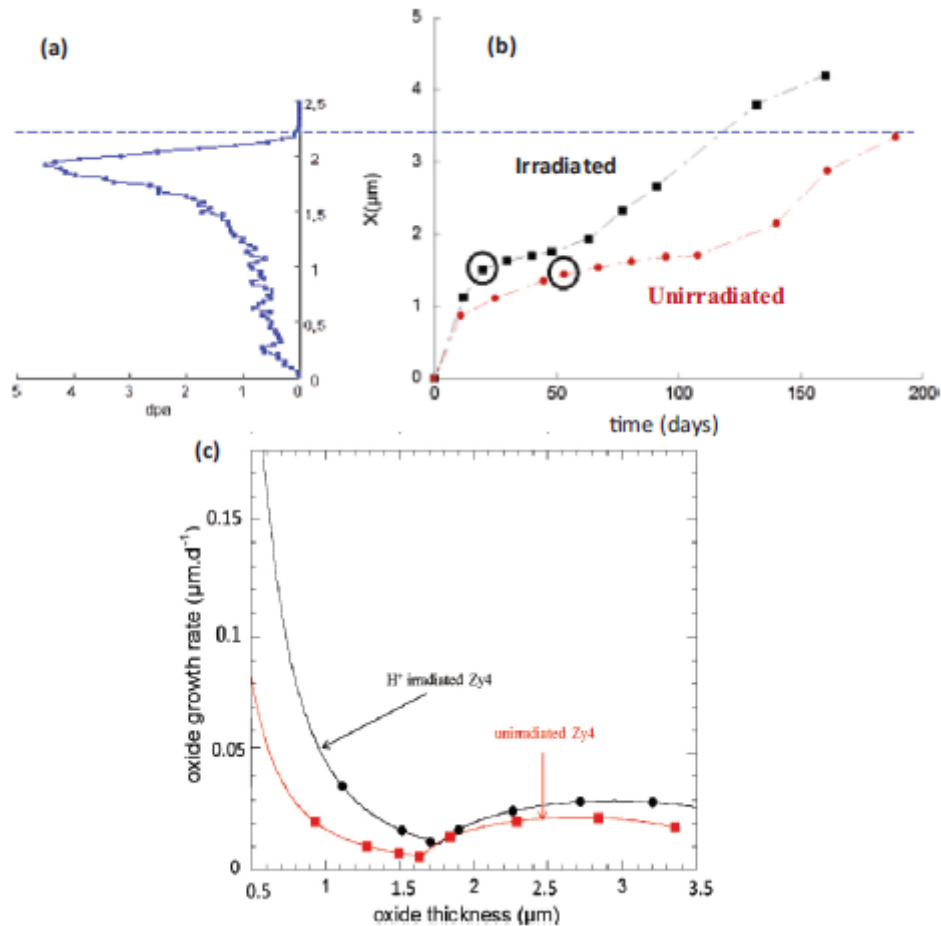


Figure 7 (a) Damage profile in the metal matrix of a Zircaloy-4 sample irradiated with 300-keV protons at a fluence of 10^{18} cm^{-2} at 360°C , (b) corrosion kinetics of Zircaloy-4 at 360°C for the unirradiated and the irradiated samples (the circles samples correspond to the ones observed in TEM), and (c) corrosion rate of Zircaloy-4 at 360°C for the unirradiated and irradiated samples [21].

In parallel of these studies on zirconium corrosion using Raman spectroscopy, the monitoring of corrosion kinetics using weight gain as well as SIMS studies after isotopic exchanges, the microstructure of the zirconium matrix and oxide layer was investigated using TEM and synchrotron microdiffraction. Indeed, the diffusion rate of oxygen through the oxide layer, which is the rate-limiting step of zirconium corrosion [22-24] depends on many things, e.g., the diffusion mechanism (vacancy or interstitial mechanism), phase composition of the layer, microstructure (grain size, grain boundary surface fraction), texture and crystal orientation, compressive stress level, etc. In particular, previous synchrotron X-ray diffraction (XRD) experiments performed on corroded prehydrided Zircaloy-4 have yielded information on the acceleration of corrosion due to hydride accumulation [11]. In this microdiffraction study, the tetragonal content decrease for the prehydrided sample was observed to be correlated to a higher corrosion rate. In addition, oxide and metal texture have been shown to affect the corrosion behavior of prehydrided and reference samples [25]. We focused in this study on the phase composition of the layer, the microstructure (grain size, grain boundary surface fraction), texture and crystal orientation, and compressive stress to determine the difference between the oxides investigated. Two main microstructural characterization techniques were used in these studies: conventional transmission electron microscopy (TEM) and synchrotron microdiffraction and fluorescence. It is clear from previous synchrotron XRD studies that the variations in the oxide structure occur at the submicron scale, and the use of microdiffraction

provides unique information not obtainable by other means. The objective of these studies was to obtain detailed information on the role that microstructural changes play in the metal and in the oxide because of corrosion resistance and to use that information to improve models of oxide growth that take into account the irradiation effect of the matrix on the corrosion rate.

TEM observations of the samples corroded 30 days in autoclave but not irradiated are presented in Figure 8. Those obtained on irradiated samples after 14 days of corrosion are presented in Figure 9 and Figure 10. The oxide grown on the irradiated matrix is heavily cracked. The oxide thickness is approximately 1.2 μm after 30 days of oxidation for the unirradiated sample, whereas that of the irradiated sample is approximately 1.5 μm after 14 days of oxidation. This confirms the accelerated corrosion kinetics of the irradiated sample as seen in Figure 7. The oxide grown on the irradiated matrix exhibits features that could be identified as nanosized pores up to 100 nm below the outer oxide surface which differs from the unirradiated oxide that did not exhibit any nanopores. This observed oxide microstructure of the irradiated sample suggests either a less passive oxide layer or diffusion short circuits through the oxide thickness that could play a role in terms of accelerating the corrosion kinetics.

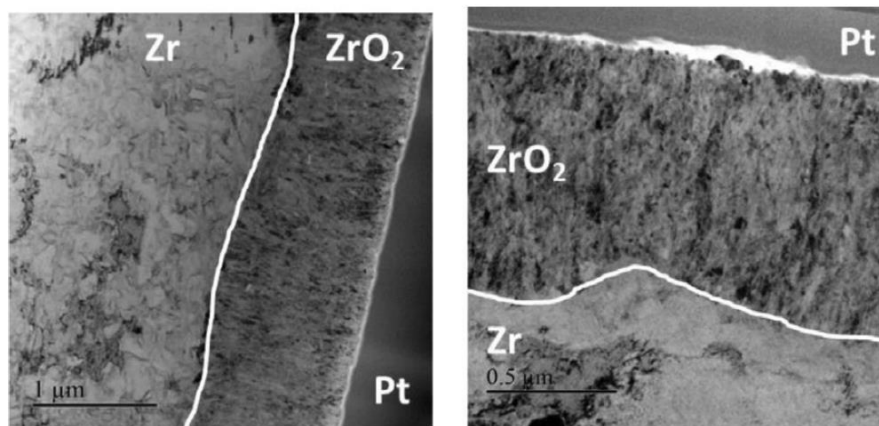


Figure 8 TEM images of the oxide microstructure formed after 30 days of corrosion of an unirradiated metal sample of Zircaloy-4.

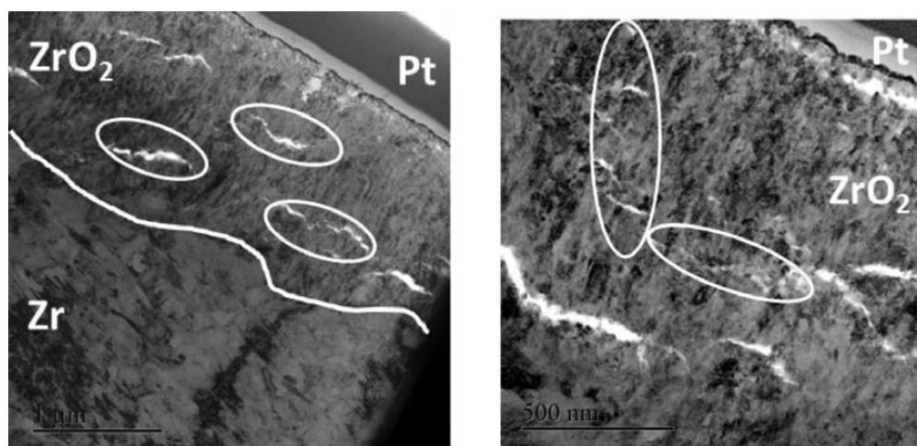


Figure 9 TEM images of the oxide microstructure formed after 14 days of corrosion at 360°C of an irradiated sample of Zircaloy-4 (irradiation conditions: 30 keV protons and fluence of 10^{18} cm^{-2} at 360°C).

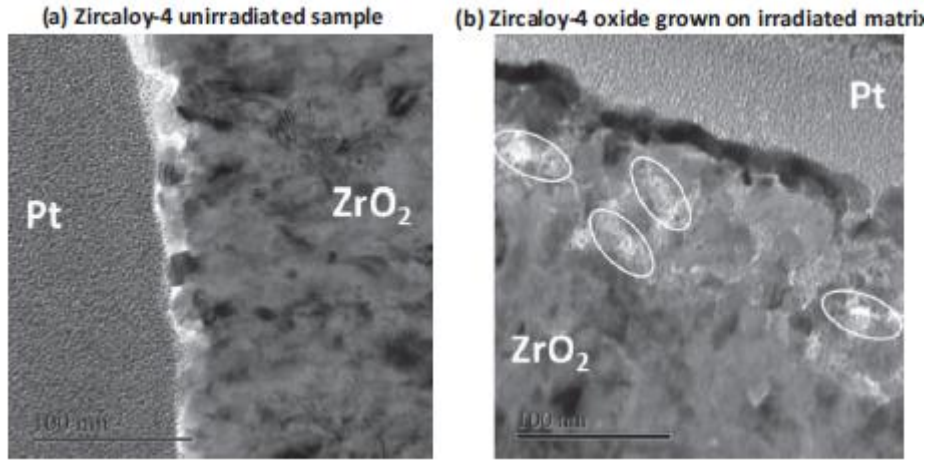


Figure 10 Higher magnification TEM images of (a) oxide formed on an unirradiated Zircaloy-4 sample after 30 days of corrosion at 360°C and (b) oxide formed on an irradiated sample after 14 days of corrosion at 360°C (irradiation conditions: 30 keV protons and fluence of 10^{18} cm^{-2} at 360°C).

To further study the impact of metal irradiation on the oxide layer microstructure, a careful analysis of microdiffraction and microfluorescence data was undertaken. A schematic of the sample set-up for these synchrotron micro-fluorescence experiments is presented in Figure 11. An example of typical diffraction patterns obtained for the unirradiated and irradiated samples is presented in Figure 12. The diffraction patterns were all taken at a similar distance, close to the respective oxide-metal interface. The diffraction patterns presented here were a selection of the larger d-spacing range studied with our sample-detector geometry. As seen in Figure 12, the signal-to-noise ratio was very good and allowed the identification of the various oxide peaks with good confidence. Two main oxide phases were identified: the monoclinic phase (noted M), which was the main expected phase given our conditions of temperature and pressure, and the tetragonal phase (noted T), which is known to appear in oxides grown on zirconium alloys. Two main monoclinic peaks, $M(111)$ and $M(-111)$, and one tetragonal peak, $T(101)$, were more closely studied in the following XRD analyses. These peaks were chosen because they are the main peaks in the Garvie-Nicholson tetragonal phase fraction formula [26] and because the tetragonal phase is sufficiently separated from the monoclinic phase to be fitted with good confidence. The Garvie-Nicholson formula is presented below:

$$t = \frac{I(T(101))}{I(T(101)) + I(M(111)) + I(M(\bar{1}11))}$$

(Equation 2)

Where : $I(X)$ = integrated intensity of the chosen diffraction peak and

t = tetragonal phase fraction

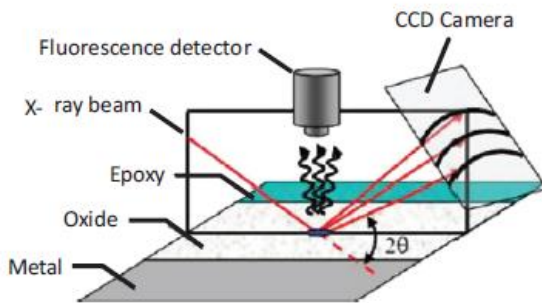


Figure 11 Schematic of the experimental setup for the synchrotron microdiffraction and microfluorescence experiments conducted at the 2-ID-D beamline at the Advanced Photon Source (similar setup as in [27]).

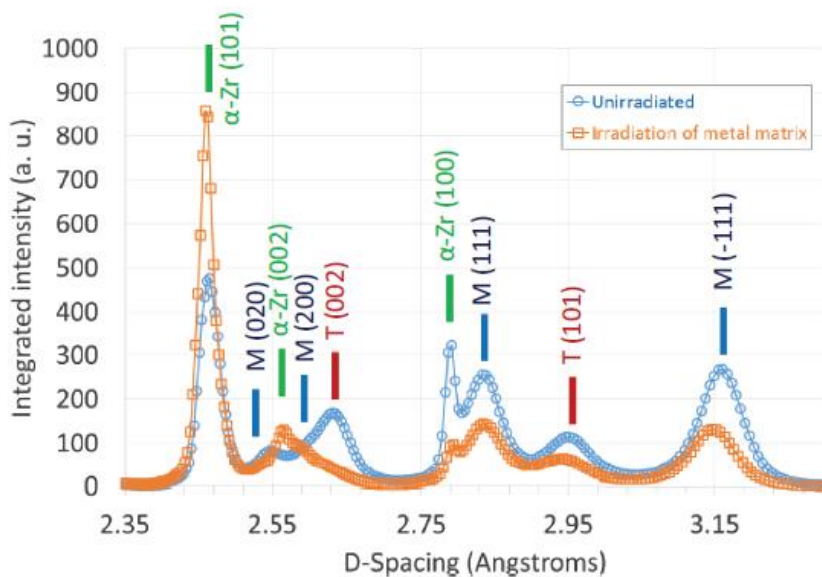


Figure 12 X-ray diffraction pattern close to the oxide-metal interface for the unirradiated sample and for the oxide grown on an irradiated matrix (irradiation conditions : 300 keV protons and fluence of 10^{18} cm^{-2} at 360°C).

Studying the synchrotron diffraction and fluorescence data, several parameters were investigated such as the intensities of the zirconium oxide peaks, the tetragonal phase fraction and the texture of the oxides. Example of such data for the unirradiated and the irradiated samples are presented in Figure 13 and Figure 14. From this figure it can be seen that the tetragonal phase fraction increased across the oxide layer and was maximum at the oxide-metal interface, which corresponds with results from previous studies [27-29]. The average tetragonal phase fraction for this oxide layer was approximately 27 %. Results from previous studies of Zircaloy-4 oxide layers have ranged from 10 % to 60 % [29-33]. The variations of the tetragonal phase across the oxide layer were more uneven than for the unirradiated sample. This was true both for the T(101) peak intensity and for the tetragonal phase fraction. The average tetragonal phase fraction for this oxide layer was approximately 18 %. This value was much lower than the one obtained for the unirradiated sample. The main conclusion from the peak intensity and tetragonal phase fraction analysis is that metal irradiation seems to lower the tetragonal phase fraction. Several scans were analyzed both on the unirradiated and irradiated samples, allowing a large sampling of the oxide, and this result was confirmed for all observed locations. The position

of the three main oxide peaks studied was also investigated to observe potential different stress state and stoichiometry effects. Results from these investigations are not shown here for the sake of brevity.

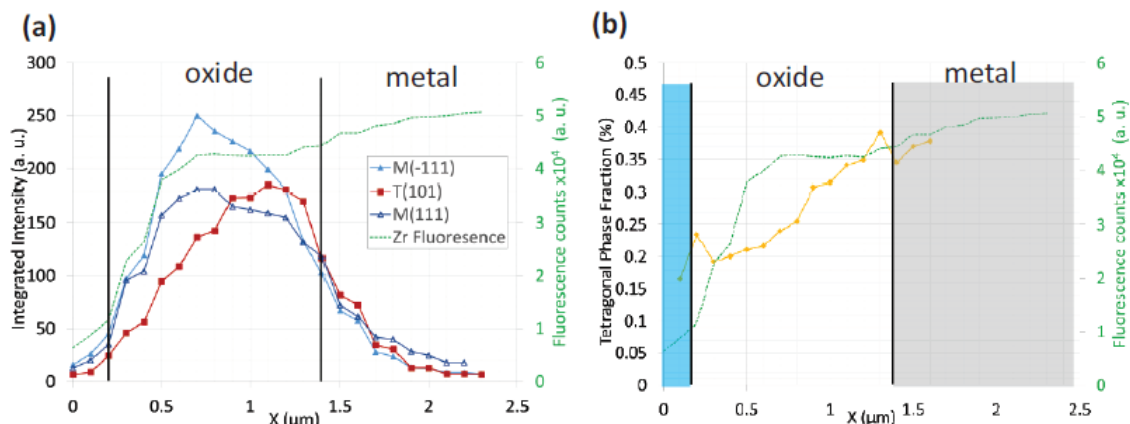


Figure 13 (a) Integrated intensity of the monoclinic (111), ($\bar{1}\bar{1}\bar{1}$) and tetragonal (101) oxide peaks and (b) tetragonal phase fraction through the thickness of an oxide formed on an unirradiated Zircaloy-4 samples after 30 days of corrosion at 360°C.

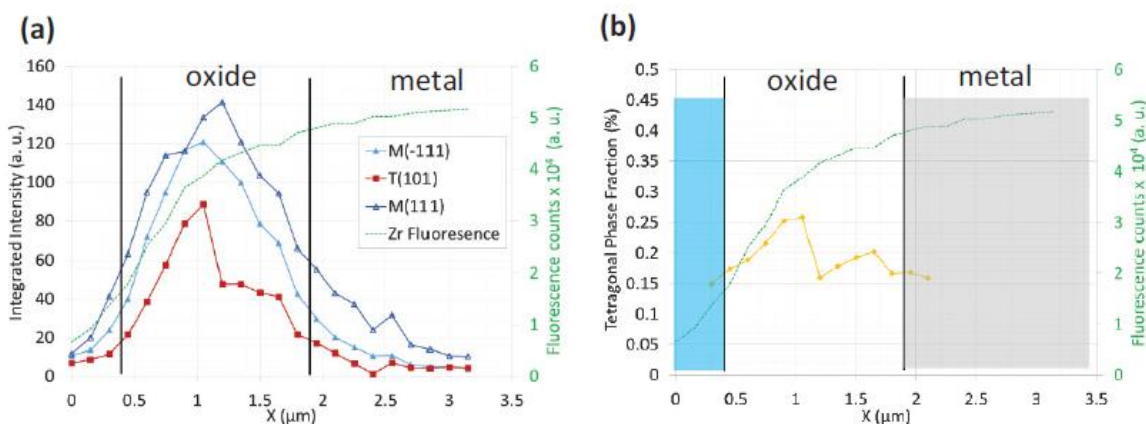


Figure 14 (a) Integrated intensity of the monoclinic (111), ($\bar{1}\bar{1}\bar{1}$) and tetragonal (101) oxide peaks and (b) tetragonal phase fraction through the thickness of an oxide formed on an irradiated sample after 14 days of corrosion at 360°C (irradiation conditions: 30 keV protons and fluence of 10^{18} cm^{-2} at 360°C).

Additional investigations were carried out using synchrotron diffraction on post-transition oxide layers. This had two objectives: to investigate the metal matrix irradiation on post-transition kinetics and the oxide microstructure and the impact of the implantation peak and a varying damage profile on the oxide microstructure. The integrated intensity of the main oxide peaks and tetragonal phase fraction as calculated by the Garvie-Nicholson formula are presented for the unirradiated sample in Figure 15. As can be seen from the oxide peak intensity profile across the oxide layer, there were two distinct layers with varying oxide peak intensity. In particular, given the transition thickness of 1.7 μm as given by the kinetic curve in Figure 7, it can be observed that there was a decrease of the tetragonal phase fraction at the kinetic transition. The tetragonal phase fraction was the lowest around the transition thickness. In the second sublayer, the increasing tetragonal profile close to the oxide-metal interface (as already observed in the pretransition layers) was observed. The average tetragonal phase fraction in this scan was 27.3 %, which was close to the pretransition value. The oxide peak intensities and tetragonal phase fraction for the irradiated sample corroded for 150 days exhibit results similar to the unirradiated sample: the oxide layer is divided into two sublayers, with an increase of

the tetragonal phase fraction close to the transition thickness of 1.7 μm . The average tetragonal phase fraction in this scan was 24.8 %, which was higher than the irradiated pretransition sample.

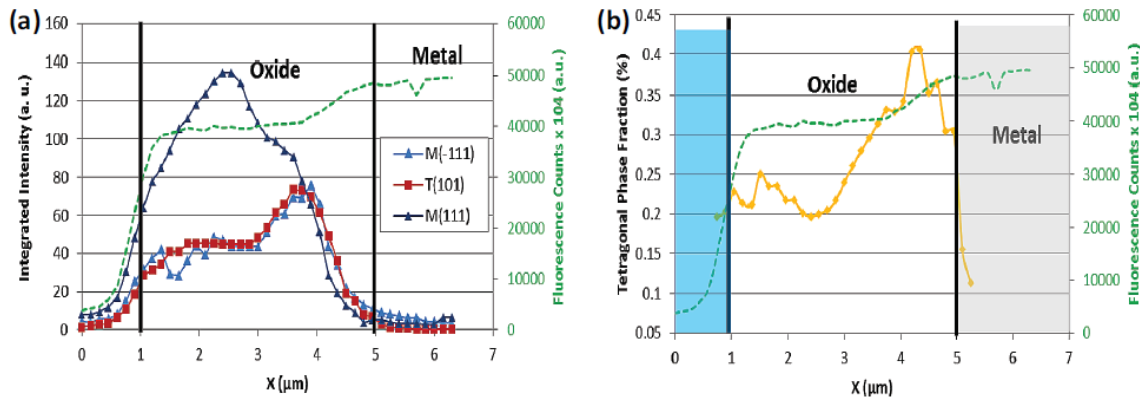


Figure 15 (a) Integrated intensity of the monoclinic (111), ($\bar{1}\bar{1}1$) and tetragonal (101) oxide peaks and (b) tetragonal phase fraction through the thickness of an oxide formed on an unirradiated Zircaloy-4 samples after 180 days of corrosion at 360°C (post-kinetic transition).

Using advanced characterization techniques involving many separated facilities and instruments, the impact of irradiation on the corrosion kinetics and oxide microstructure using TEM and synchrotron microdiffraction of ion-irradiated samples was studied. The effects of the irradiation of the metal matrix and of the oxide layer were studied separately. Common observations between metal irradiation and oxide irradiation were that (1) ion irradiation of the metal matrix and of the oxide layer both led to an acceleration of the corrosion kinetics and (2) irradiation induced a decrease of the tetragonal phase fraction. Differences observed between metal irradiation and oxide irradiation were that (1) the oxide formed on irradiated metal was severely cracked and presented a lower d-spacing that could have been caused by higher compressive stresses and/or stoichiometry variations; (2) irradiation of the oxide released some of the compressive stresses in the monoclinic phase (no differences were observed in TEM; defects formed were likely point defects); and (3) the impact of irradiation of the metal and of the oxide was different in terms of oxide microstructure but similar in terms of corrosion kinetics. The main result from this paper is that, even though the different oxide layers, characterized using detailed, advanced characterization techniques, showed few differences in microstructure, the corrosion kinetics of these samples were very different. This stresses the importance of studying and taking into account point defects when understanding and predicting corrosion behavior as seen in the first part of this paragraph.

Using similar experimental principles and methods than those used for Zircaloy-4, the corrosion kinetics of the M5 alloy was studied as well. The M5 alloy has been developed by Framatome in order to increase fuel performance and safety and is currently in used in several PWRs in the world. In PWRs, the oxidation rate of M5 remains quite constant up to 70 GWd/tU—unlike Zircaloy-4. The M5 alloy exhibits thus a good resistance, even at high burnups [15, 17]. In this sense, it has been recently observed that the ion irradiation of the oxide-metal interface at a low damage level results in a significant decrease of the oxidation rate of this alloy [34]. For this experiment, the M5 samples were corroded in static autoclaves in light primary water (H_2O) at 360°C and 18.7 MPa of pressure with 2 ppm in mass of lithium and 1,000 ppm in mass of boron from the lithium hydroxide and boric acid added to the water. The choice of irradiation conditions was guided by the simulation software SRIM2008 [35]: it was found that 1.3-MeV helium ion irradiations provided the desired uniform distribution of irradiation defects in the oxide. The irradiations were performed at the University Paris-Saclay CSNSM JANNUS Orsay facility with a 1.8-MeV tandem-accelerator called ARAMIS. The samples were irradiated at 60°C, at two doses: 0.036 and 0.36 dpa (flux of 5×10^{12}

$\text{cm}^{-2}\cdot\text{s}^{-1}$). The oxidation kinetics were followed by weight gain, then the oxide layers were characterized using Raman spectroscopy, isotopic exposure and SIMS as well as TEM. As seen in Figure 16, the oxidation kinetics are reduced by irradiation in the chosen conditions for M5: the oxidation rate is reduced after irradiation by a factor of approximately 2 compared with the unirradiated material, and this effect remained beyond 100 days.

Figure 17 shows the microstructure of the unirradiated oxide layer formed on M5, including the precipitates embedded within it. The oxide thickness was approximately 1.5 μm , as expected after 20 days of corrosion. The usual columnar structure is observed in Figure 17, and the average columnar grain diameter was close to the common value of approximately 50 nm for this material [18]. Figure 18 shows an amorphized precipitate and the niobium distribution map obtained by the energy-filtered transmission electron microscopy (EFTEM) showing that this element was localized inside the precipitate. According to its size (~150 nm), it was likely an intermetallic precipitate, $\text{Zr}(\text{Nb}, \text{Fe})_2$. Figure 19 presents the microstructure of the oxide layer irradiated up to 10^{17} helium/ cm^2 and then annealed for 24 h under PWR conditions. The microstructure was roughly similar to that shown for the reference material. At a finer scale, the columnar microstructure may appear less marked and regular than on the unirradiated oxide; however, this feature should be supported by further characterizations. EFTEM performed on the irradiated layers (Figure 20) revealed large niobium enriched areas which are unfortunately not typical of neutron irradiated samples.

Finally using data from the SIMS experiment, a model was developed to simulate irradiated M5 corrosion kinetics, the model is plotted in Figure 16. This model satisfactorily simulates the kinetic curve and is thus compatible with our experimental results. However, this modeling needs to be improved further or validated by specific studies on electric field effects which is the subject of further studies led by M. Tupin's group in particular.

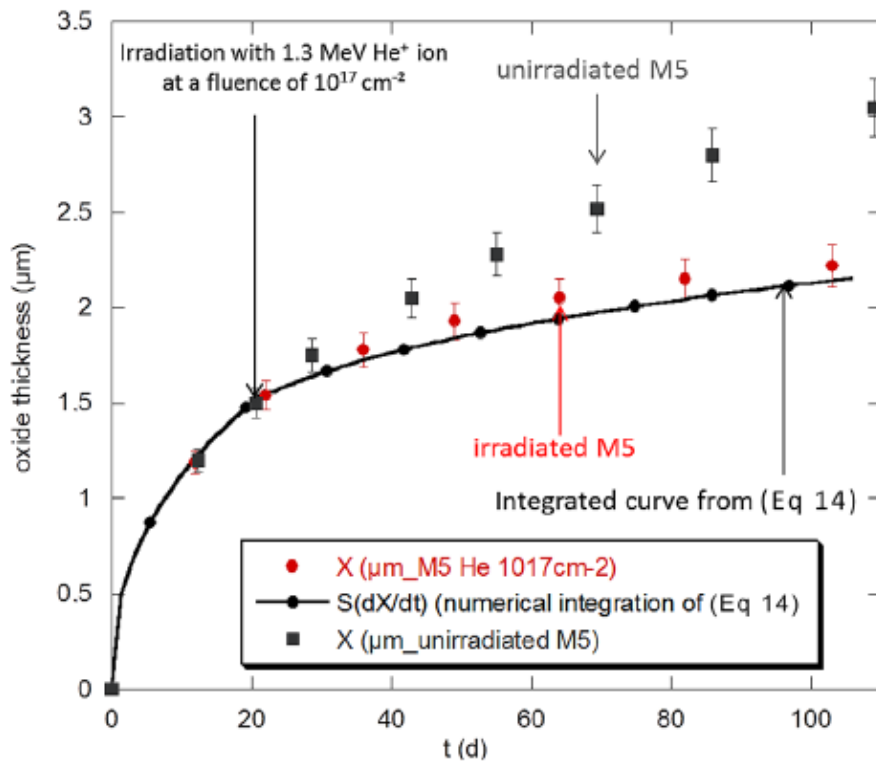


Figure 16 Oxidation kinetics with (full circles) or without (full squares) irradiation. The black curve with dark circles is the simulation from [20].

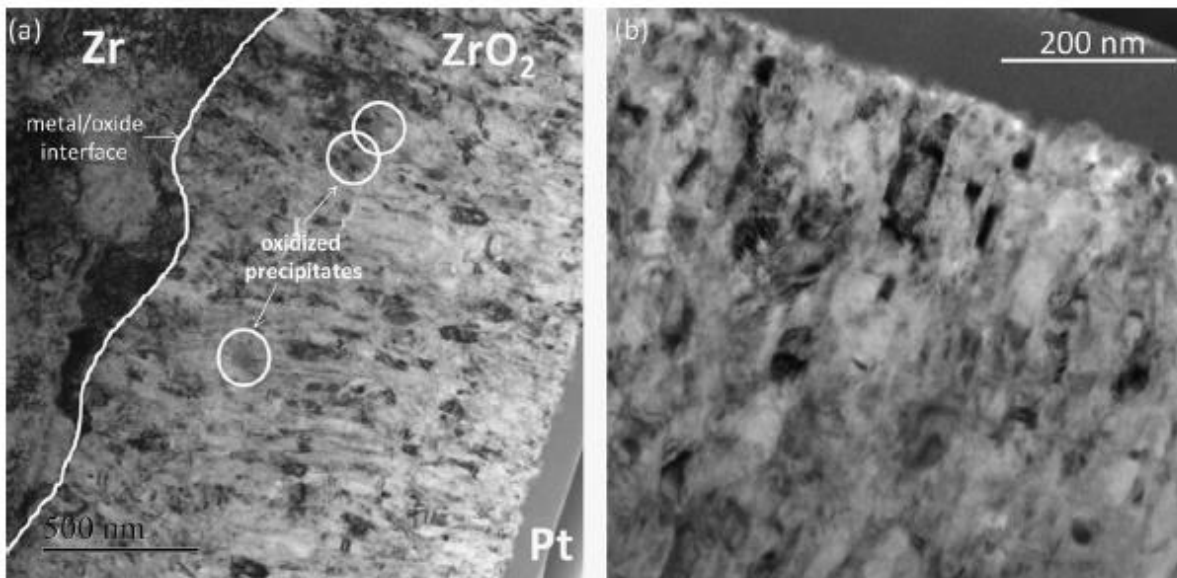


Figure 17 (a) TEM micrograph of the unirradiated oxide layer formed on M5 after 20 days of oxidation in PWR conditions. Three precipitates are observable (white circles). (b) TEM micrograph of the columnar microstructure of the unirradiated oxide layer formed on M5.

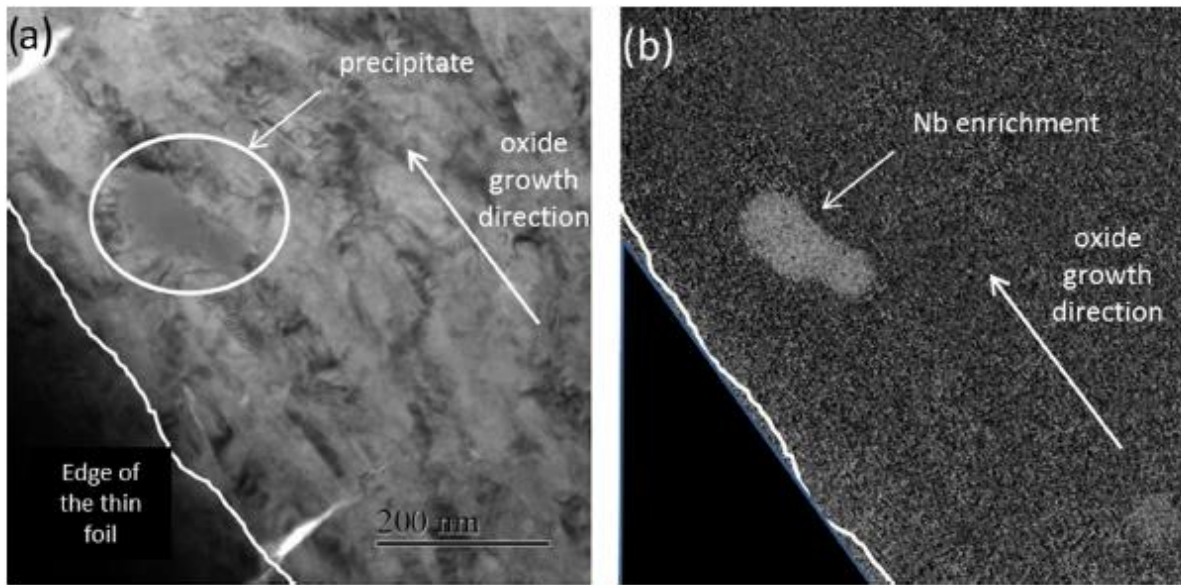


Figure 18 (a) TEM micrograph of the oxide layer with amorphized precipitate. (b) Niobium distribution around the precipitate using EFTEM mapping.

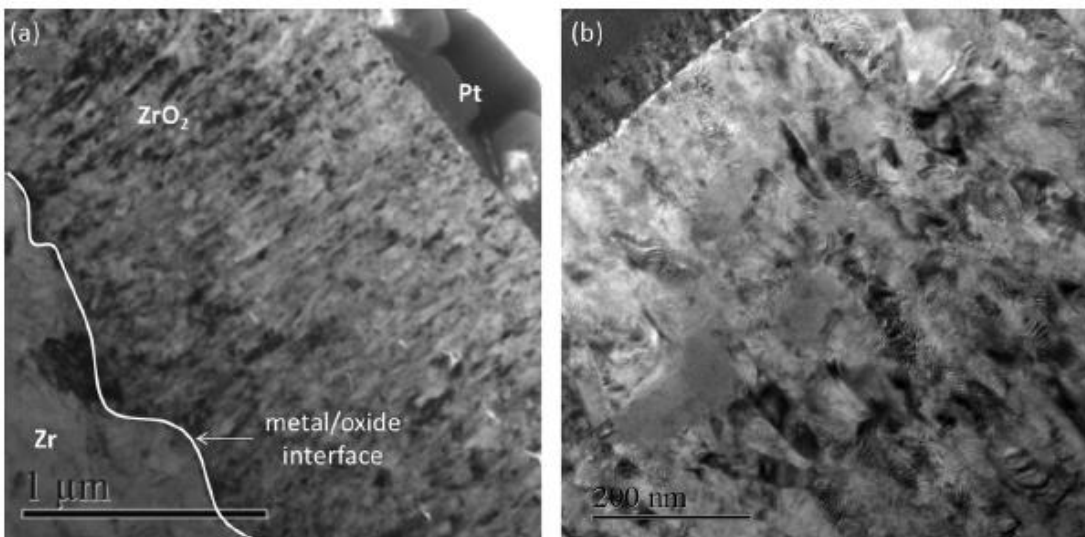


Figure 19 (a) TEM micrograph of the irradiated oxide layer (helium : 1.3 MeV up to 10^{17} cm^{-2}) formed on M5 after 20 days of oxidation and reoxidized 24h in PWR conditions after irradiation. (b) TEM micrographs of the irradiated oxide layer formed on M5 (helium: 1.3 MeV up to 10^{17} cm^{-2}).

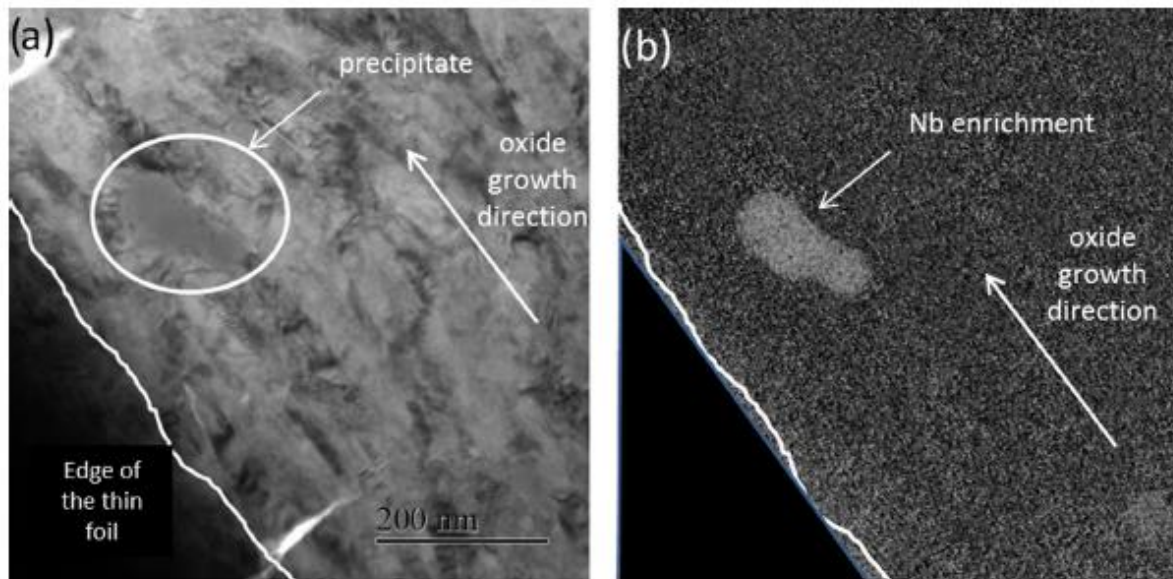


Figure 20 (a) TEM micrograph of the irradiated oxide layer with an enriched-grain niobium (irradiation condition helium: 1.3 MeV up to 10^{17} cm⁻²). (b) EFTEM analysis of the niobium distribution.

Summary of studies on zirconium alloy corrosion

In this paragraph, I have presented the work I have performed or contributed to during my 8 years of research at the CEA Saclay hotlab in collaborations notably with M. Tupin. I participated in the supervision of one of his PhD student, R. Verlet and led some of the experiments myself. Most of the research was cofounded by CEA, EDF and Framatome. From the studies presented in this paragraph, it becomes clear that, in order to understand a complex phenomenon such as corrosion under irradiation of zirconium cladding, several means of characterization are necessary. Firstly, the use of accelerators in order to simulate neutron irradiation and allow separate effects studies without dealing with the cost and complexity of radioactive samples was the basis for many of our studies. At different steps of the process the samples are corroded and in autoclaves and their corrosion is followed by measuring their weight gain. It was shown by Raman spectroscopy that point defects play an important role in the corrosion kinetics. Isotopic exposure (changing O¹⁶ in O¹⁸) coupled with SIMS also allowed us to calculate diffusion coefficients that served as the basis for corrosion models implemented on Zircaloy-4 and M5 alloys. Microstructural characterization techniques were also key in order to understand which of the hypotheses explaining high burnup acceleration of corrosion plays a major role. From TEM observations, nanopores may be a key to understanding this acceleration for Zircaloy-4. TEM examinations have also shown that, in our studies and our irradiation conditions, Nb segregation and precipitation does not necessarily seem to be the most influential parameter in the good corrosion resistance of M5 under irradiation. Finally synchrotron experiments showed some variations in the tetragonal phase fraction and compressive stresses that could be further studied in order to understand post transition behavior and what may then to destabilize zirconium oxide layers.

As mentioned previously, the corrosion reaction lead to the formation of hydrogen atoms at the cladding surface. Part of this hydrogen is adsorbed into the cladding, diffuses and precipitates as zirconium hydrides. Zirconium hydrides can be significantly damaging for used fuel. Most of my PhD work was based on used fuel issues but I have also continued this work at CEA. Some of the publishable results from this work are presented in the following paragraph.

2.2 Back-end issues

The main issues discussed in this paragraph occur during the drying, transportation and storage of used nuclear fuel. The fuel cladding is corroded, hydride once it is removed from the reactor core and yet it must maintain good mechanical properties in order to keep the fission gases inside the cladding and act as the first confinement barrier. The used fuel must also present good retrievability until a more permanent storage solution is found or recycling of the fuel assemblies occur.

The hydrides present in the fuel cladding and their capacity to embrittle the cladding are the focus of the studies presented in this paragraph. The hydrides form as platelets oriented with the platelet face in the circumferential-axial plane of the tube, thus circumferential hydrides. When subjected to temperature cycles and applied stress such as can happen during preparation for dry-storage of used fuel, these hydride platelets can dissolve and reorient in the axial-radial plane perpendicular to the hoop stress. This phenomenon, present as a result of fission gas pressure, is called hydride reorientation, and leads to loss of ductility of the cladding and is thus an important issue for used fuel safety. Hydrides can also precipitate at pre-existing stress concentrations such as flaws and lead to early cladding failure by the repetitive cracking process called Delayed Hydride Cracking (DHC). Such processes depend on the hydrogen mobility and precipitation under temperature and stress.

The main results from my PhD work on hydride reorientation [36], from which part of my work at CEA was based upon, are summarized in the following paragraph.

The current available data in the literature on hydrogen and hydride behavior usually comes from studies conducted *post-facto*, thus suffering both from a scarcity of data points and from the confounding effects of studying only the resulting hydride microstructure at room temperature, rather than what is present at higher temperature. In my PhD work, an *in-situ* X-ray diffraction technique using synchrotron radiation was used to follow directly the kinetics of hydride dissolution and precipitation during thermo-mechanical cycles as illustrated in Figure 21. This technique was combined with conventional microscopy (optical, SEM and TEM) to gain an overall understanding of the process of hydride reorientation. Thus this part of the study emphasized the time-dependent nature of the process, studying large volume of hydrides in the material.

In the study of the kinetics of hydride precipitation and dissolution in bulk samples, it was found that the precipitation and dissolution temperatures (T_p and T_d) corresponded well to the values obtained with differential scanning calorimetry as seen in Figure 21. The applied stress, when sufficiently high to reorient the hydrides, lowered the T_p .

The samples used showed hydride reorientation at 200 MPa for cold-worked Zircaloy-4, 80 MPa for recrystallized Zircaloy-4 and below 75 MPa for recrystallized Zircaloy-2 for samples with 200-600 wt.ppm of hydrogen. The degree of reorientation and the hydride connectivity increased with the number of thermo-mechanical cycles. The hydride elastic strains from peak shift and size and strain broadening were studied as a function of time for precipitating hydrides. Some of the main results from this analysis are presented in Figure 22. The hydrides precipitate in a very compressed state of stress, as measured by the shift in lattice spacing. As precipitation proceeds the average shift decreases, indicating average stress is reduced, likely due to plastic deformation and morphology changes. When nucleation ends the hydrides follow the zirconium matrix thermal contraction. When stress is applied below the threshold stress for reorientation, hydrides first nucleate in a very compressed state similar to that of unstressed hydrides. After reducing the average strain similarly to unstressed hydrides, the average hydride strain reaches

a constant value during cool-down to room temperature. This could be due to a greater ease of deforming the matrix due to the applied far-field strain which would compensate for the strains due to thermal contraction. Finally when hydrides reorient, the average hydride strains become tensile during the first precipitation regime and remain constant in the tensile direction during the second precipitation regime. This could be due to the fact that the face of reoriented hydride platelet is in compression once these platelets have grown to a sufficient size.

When studied with TEM, reoriented hydrides were observed to be approximately 300 nm thick and made of a single large precipitate. Circumferential hydrides were also about 300 nm thick and the individual hydrides stacked on top of each other. The orientation relationship for both circumferential and reoriented hydrides was found to be approximately $\delta(111) // \alpha(0002)$.

A phase-field model was developed to attempt the modeling of hydride precipitation in bulk single crystal and poly-crystalline zirconium. The model was found to successfully predict the stacking of circumferential hydrides and the expected orientation relationship between the hydride and the matrix. The effect of stress was also studied and found to lead to partial hydride reorientation.

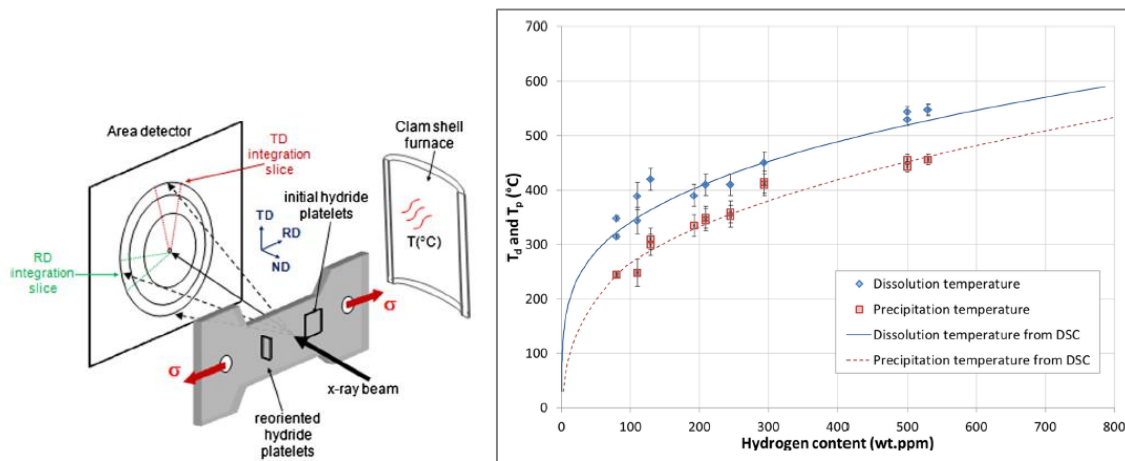


Figure 21 Schematic representation of in-situ synchrotron XRD experiment to study hydride dissolution and precipitation kinetics ; Dissolution and precipitation temperatures (T_d et T_p) as a function of hydrogen content [37].

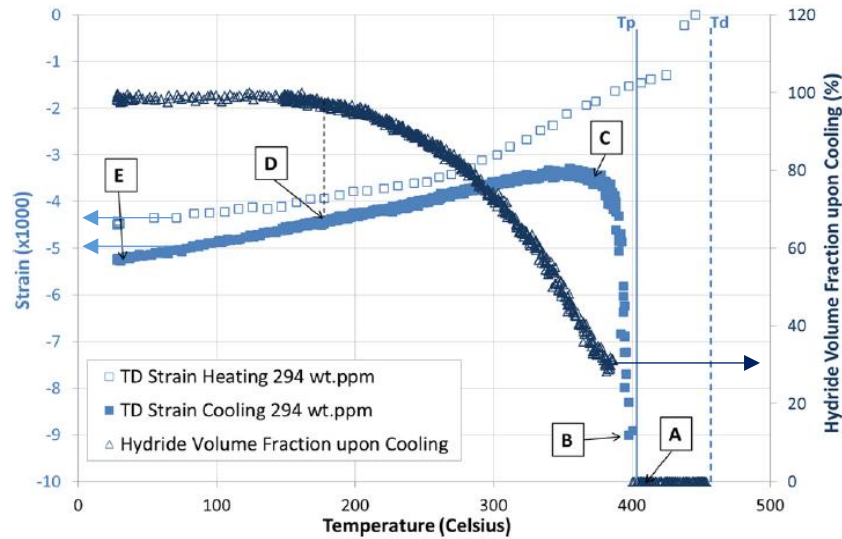


Figure 22 Evolution of strain and hydride volume fraction followed in-situ by synchrotron XRD during a heating cycle followed by a cooling cycle [38].

The work on the phase-field model was continued by T. W. Heo after the end of my PhD and our collaboration continued. The main results from this phase-field modeling of hydrides are presented in this paragraph. In this study, a comprehensive phase-field model was developed for investigating hydride formation and their morphologies involving large volume expansion in single and polycrystalline metals employing the δ -hydride formation in α -Zr as a model system [39]. More specifically, the model developed permitted performing controlled simulations for exploring the morphological stability of multi-variant hydrides upon interfacial coherency variation. This behavior was explained by referring to the identified habit plane modes for the different coherency states. Phase field simulations incorporating random fluctuations of field variables to observe the behaviors of naturally nucleated δ -hydrides in single- and bi-crystals of α -Zr were also carried out. An example of a polycrystalline simulation conducted during this study is presented in

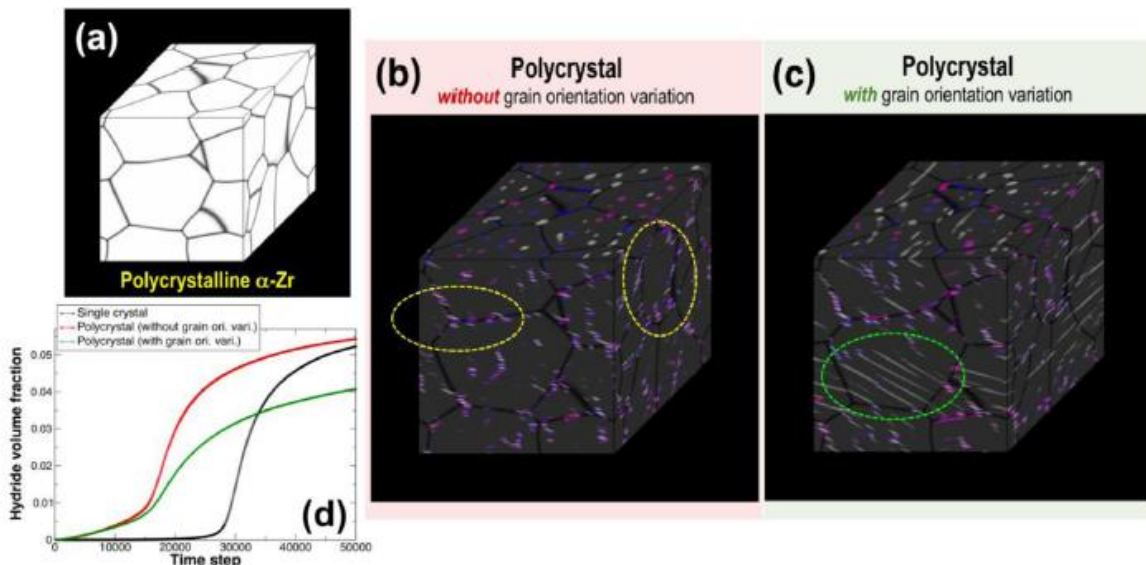


Figure 23 (a) Prepared polycrystalline α -Zr for simulating δ -hydride formation; (b) simulated δ -hydride microstructure in a polycrystal without grain orientation variation (at $t=40\ 000\Delta t$); (c) simulated δ -hydride microstructure in a polycrystal with grain orientation variation (at $t=40\ 000\Delta t$); (d) Hydride volume fraction vs Time step for different simulation conditions.

polycrystal with grain orientation variation (at $t=40\ 000\Delta t$) ; (d) hydride volume fraction as a function of time for single and polycrystals [39].

By analyzing the obtained phase-field simulation results during different sets of calculations, three possible hydride re-orientation mechanisms are proposed:

- **Mechanism 1:** The applied load may induce structural defects at hydride/metal interfaces, which cause interfacial coherency loss along the c -axis. The corresponding coherency state variation affects the growth direction of individual hydride variants and eventually enhances hydride stacking behavior, leading to the effective growth of the macro-platelets of the hydrides more aligned along the c -axis.
- **Mechanism 2 :** The possible shear component of the applied stress, which may arise from grain texture or sample geometry, causes the selection of certain variants of hydrides due to inter- actions between the shear stress and the shear component of the transformation strain. This variant selection behavior coupled with coherency loss along the c -axis induces more compact stacking behaviors of the selected variants, resulting in the growth of the macro-platelets more aligned along the c -axis.
- **Mechanism 3:** Individual hydride variants with fully coherent hydride/metal interfaces tend to independently grow and be more aligned along the basal plane. These fully coherent variants interact more strongly with and segregate to grain boundaries aligned along the basal plane. On the other hand, according to the proposed Mechanism 1, the coherency loss along the c -axis enhances the stacking tendency of the hydride variants, leading to the growth of the macro-platelet aligned along the c -axis. These macro-platelets tend to segregate at grain boundaries aligned along the c -axis. Therefore, the re-orientation tendency due to coherency loss is enhanced by those hydride-grain boundary interaction behaviors.

The model developed in this study can also be employed to simulate the hydride formation in generic polycrystalline α -Zr containing multiple grains. The simulations demonstrated that the kinetics of hydride formation is strongly affected by the grain texture and the internal stress arising from the precipitated hydrides themselves.

This work illustrated, in my opinion, the essential link between characterization and modeling. Indeed, during my PhD work, I contacted Dr Chen's research group which Dr Heo was part of in order to try and modeling hydride microstructure and better understand some of the results I obtained during my in-situ synchrotron experiments. Their work has then led so several theories explaining hydride reorientation that could be investigated further using TEM (conventional and in-situ) as well as EBSD for example. Some of these studies are currently being conducted at CEA.

My work at the CEA hotlab on hydride reorientation also focused on neutron irradiated fuel cladding which was something inaccessible during my PhD work at a university. Partially funded by EDF, CEA and EPRI's Nuclear Fuel Industry Research program, some work was performed on commercial fuel cladding irradiated in existing PWRs and BWRs. The goal of some of these studies was to understand the mechanical behavior of the cladding as a function of hydride reorientation in order to assess the key safety parameters for the safe transportation and storage of fuel cladding.

The published work from this research investigated hydride reorientation and its impact on ductility in unirradiated and irradiated recrystallized Zircaloy-2 cladding with an inner liner (cladding for BWRs) subjected to hydride reorientation treatments [40]. Cooling from 400°C, hydride reorientation occurs in recrystallized Zircaloy-2 with liner at a lower effective stress in irradiated samples (below 40 MPa) than in unirradiated specimens (between 40 and 80 MPa). Despite significant hydride reorientation,

unirradiated recrystallized Zircaloy-2 with liner with ~200 wppm hydrogen shows a high diametral strain at fracture (>15%) during burst tests at ambient temperature. This ductile behavior is due (1) to the lower yield stress of the recrystallized cladding materials in comparison to hydride fracture strength (corrected by the compression stress arising from the precipitation), and (2) the hydride or hydrogen depleted zone generated by the liner's segregation effect.

In irradiated Zircaloy-2 with liner cladding containing ~340 wppm hydrogen, the conservation of some ductility (as seen in Figure 24) during ring tensile tests at ambient temperature after reorientation treatment with cooling rates of ~60 °C/h (Type B) is also attributed to the existence of a hydride-depleted zone (see Figure 25 middle column for reoriented hydride microstructure). Treatments at lower cooling rates (~6 °C/h and 0.6 °C/h, Type C-Transport Scenario and Type C-Storage Scenario respectively) promotes irradiation defect annealing and hydrogen segregation by the liner, which results in a significant increase in ductility as seen in Figure 24 and Figure 25. Consistent with results reported in previous investigations, the liner impedes the formation of any hydrides in the zone adjacent to the liner. The extent of the hydride-depleted zone increases as the cooling rate decreases. Given the very low cooling rates typical of dry storage systems, the thermal transient associated with dry storage should not degrade, and more likely should actually improve, ductility of recrystallized Zircaloy-2 cladding with inner liner with such hydrogen content. Due to the hydrogen segregation action by the liner, hydride reorientation is not an active degradation mechanism during dry storage of such fuel claddings. In addition to the liner's segregation effect, the comparison in performance of recrystallized, unirradiated vs. irradiated cladding shows the potential beneficial effect of irradiation defect annealing in lowering the yield stress of the as-irradiated cladding, which in turn, decreases its susceptibility to radial hydrides embrittlement. Indeed, the degree of radial hydrides embrittlement results not only from the radial hydrides characteristics (fraction, length and content distribution for example) but also from the matrix yield strength, which is related to the metallurgical state.

Consequently, to properly assess radial hydride embrittlement in spent fuel rod cladding requires testing of representative irradiated specimens. The extent of annealing and yield stress restoration largely depends on the characteristics of the thermal cycle that is imposed during the hydride reorientation treatment.

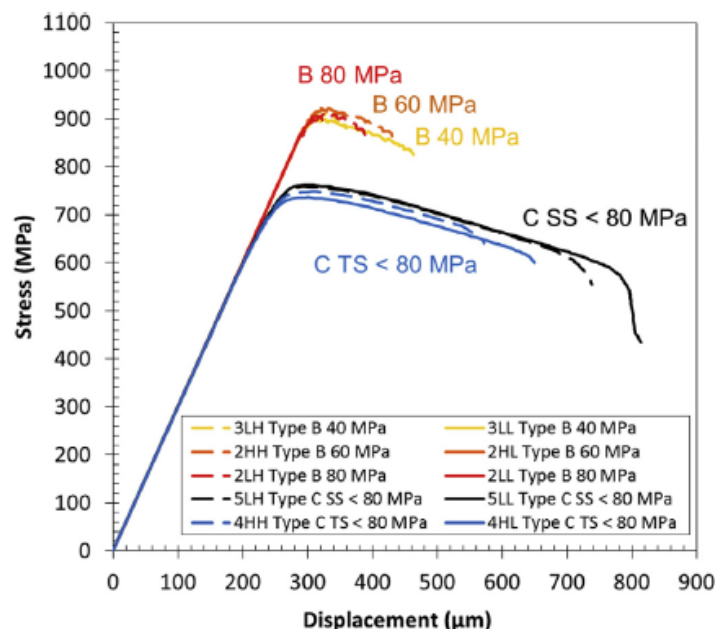


Figure 24 Ring tensile tests at ambient temperature on irradiated specimens after Type B and C treatments [40].

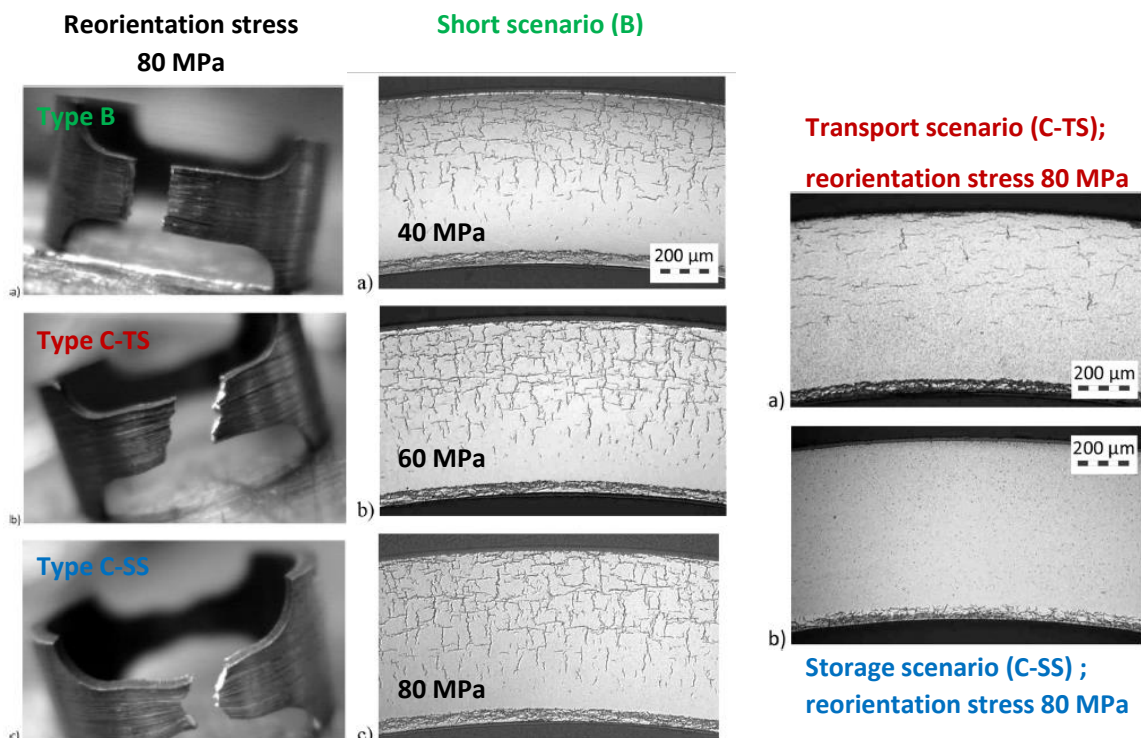


Figure 25 (Left column) : Pictures of fractured irradiated specimens after ring tensile testing at ambient temperature ; prior to tensile testing, the specimens had been subjected to treatment at 80 MPa effective stress: a) Type B (short duration, constant pressure) treatment, b) Type C-TS treatment (longer treatment, transportation scenario), c) Type C-SS treatment (longer duration, storage scenario). **(Middle column):** Etched metallographic cross section of irradiated specimens after Type B treatment at: a) 40MPa, b) 60 MPa and c) 80 MPa treatment ; **(Right column)** Etched metallographic cross section of irradiated specimen after treatment at 80 MPa effective stress, a) Type C-TS, b) Type C SS [40].

The work presented above was also performed on PWR cladding and is currently in its final steps before publication. The cladding investigated are Zircaloy-4 and Zirlo™ irradiated in French and American PWRs. The main conclusions from this work are that cold-worked, stress-relieved Zircaloy-4 and Zirlo™ behave very similarly, although irradiated Zirlo™ was found to be slightly more prone to hydride reorientation (HRO) than irradiated Zircaloy-4. No distinct irradiation-induced effect on the hydride reorientation (HRO) critical stress was detected. Depending on the initial high temperature that varied from 350 to 450 °C, HRO may cause a ductile-to-brittle transition when the cladding hoop stress, created by internal pressurization of the specimen, ranges from 70 MPa to 120 MPa . Cracking of the oxide layer caused local preferential radial hydride precipitation. The impact of the decreasing temperature and internal pressure during cool-down was also investigated: it has been found that samples undergoing decreasing temperature and pressure cycles are less prone to hydride reorientation.

From the work presented above, it can be seen that the characterization of the hydride microstructure in terms of orientation, length and also overall hydrogen content is essential in order to quantify and better understand hydride reorientation and the subsequent cladding embrittlement. A program was developed at CEA in order to do such a quantification based on micrographs of hydride cladding. This software called Hydruro is based on a CEA patent [41] and uses different steps of image processing that are represented in Figure 26. After the final skeletonization step, hydrides can be counted individually and their orientation can be determined. An example of the used of the Hydruro software on neutron irradiated cladding is presented below.

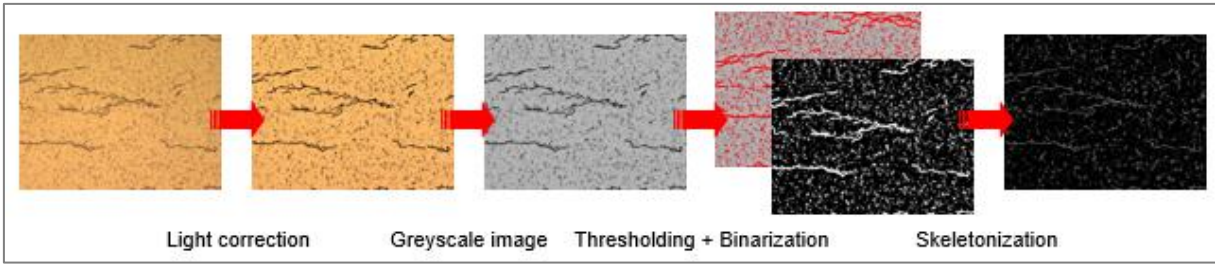


Figure 26 Image analysis steps used in Hydruro to analyze zirconium hydrides [41].

In the example shown here, a sample of CWSR Zircaloy-4 irradiated up to 50 GWd/tU in a PWR has undergone a post-irradiation thermo-mechanical treatment [42]. The goal of the treatment is to reorient partially the hydrides present in the sample and evaluate the impact of radial hydrides on the mechanical behavior of the cladding comparatively to circumferential hydrides. The rod samples undergo heating and cooling with internal pressure in order to reorient hydrides. The sample presented in Figure 27 has a global hydrogen content of ~350 wt.ppm as measured by Hydruro. The left-hand picture shows the sample after a 400°C, 120 MPa equivalent hoop stress reorientation treatment. From this figure, the hydride rim, present close to the outer diameter of the cladding (top part of the image) is visible. This rim is due to the gradient in temperature between the outer side of the cladding in contact with the coolant and the inner side of the cladding in contact with the fuel pellet. A mixture of circumferential and radial hydrides are present. The original image has been cut into several smaller images treated with Hydruro as illustrated by the central image of Figure 27. After analysis of the orientation of the hydrides present in this figure, a gradient of radial hydride fraction can be plotted as seen in Figure 27. As expected, in the rim region, the radial hydride fraction (RHF) is lower due to the high concentration of circumferential hydrides. This RHF increases as the distance from the outer diameter of the cladding increases. In this study, the metallography sample was a small ring taken from the reoriented rodlet allowing several mechanical tests to be performed on the reoriented rodlet.

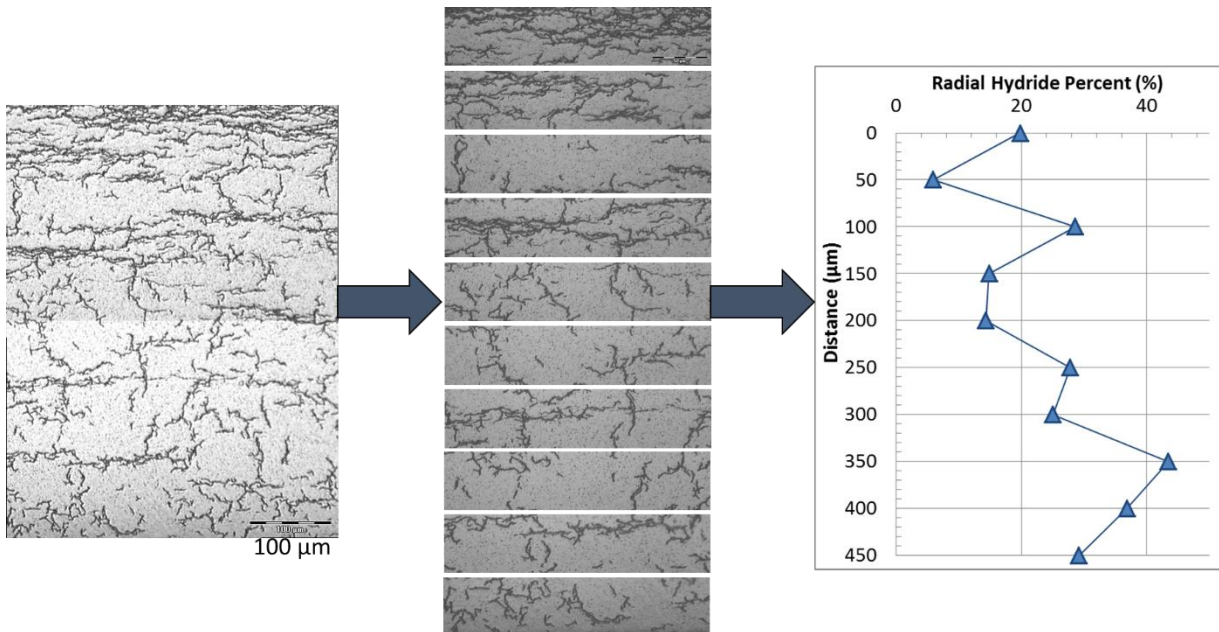


Figure 27 Example of application of Hydruro on irradiated Zircaloy-4 cladding after a reorientation treatment [42].

Summary of studies on used fuel and hydride reorientation

In this paragraph, I have presented the work that I have performed or contributed to on the subject of used fuel. First during my PhD work using synchrotron radiation on unirradiated Zircaloy-4 cladding, I have focused my work on understanding the kinetics of hydride reorientation. The use of synchrotron radiation diffraction has allowed me to follow in-situ the dissolution and the reprecipitation of hydrides and determine the terminal solid solubility limit of hydrogen in zirconium for my experimental conditions. This work was continued by a collaboration with a group of experts in phase field modeling in order to try and understand the physical mechanisms that lead to hydride reorientation in cladding.

Building up on my work on used fuel, as a project manager on used fuel and as a task leader in the NFIR program, I have studied the mechanical properties of irradiated zirconium cladding from BWR and PWR reactors. Using tools developed in house, such as the Hydrudo software, and experimental devices positioned inside hot cells, the conditions that lead to brittle cladding because of hydride reorientation have been determined. In particular, a ductile to brittle transition is observed when hydrides are highly reoriented in PWR cladding. This transition is not as stark for BWR cladding since the pure zirconium liner acts as a sink for hydrogen atoms in the cladding during a temperature excursion.

2.3 Summary and perspectives of work on zirconium alloys

This part of the manuscript was focused on the characterization of zirconium alloys used for cladding in LWRs reactors in order to understand some of the key phenomena affecting the behavior of the cladding in-reactor (corrosion and hydriding) and once the fuel is removed from the reactor (hydride embrittlement, hydride reorientation). The corrosion behavior was studied for Zircaloy-4 and M5TM alloys and the use of ion irradiation was key to conduct separate effect experiments. The effect of irradiation on the metal for example led to microstructural changes observed by TEM and using synchrotron micro-diffraction. The role of point defects created by irradiation and their evolution during subsequent corrosion tests were inferred from Raman spectroscopy on the corrosion layer. The corrosion kinetics were followed by classical weight gain studies and also using isotopic exchange combined with SIMS to observe oxygen diffusion in particular. Using the results from the kinetics studies, corrosion models were developed to better predict corrosion for the two alloys studied.

Future work on the subject of zirconium corrosion will include coated cladding and the complex corrosion behavior of multi-layered samples. Indeed, in order to develop safer nuclear fuel without impacting efficient operation, chromium coated fuel were developed at CEA in particular and are currently being irradiated in nuclear reactors. The behavior of this fuel cladding is the subject of many future studies. Additionally, the corrosion behavior presented in this manuscript is for uniform corrosion of the cladding. Localized corrosion can occur at very specific parts of the fuel assembly and could be the subject of future work in order to ensure the entirety of the fuel assemblies behaves, in terms of corrosion, in a safe and efficient way.

Issues concerning used fuel presented in this manuscript were first studied on unirradiated fuel using high energy synchrotron diffraction in order to follow the kinetics of hydrides dissolving, precipitating and reorienting under applied stress. Collaboration with a modeling team led to the development of a phase-field model in order to better predict hydride reorientation and also study what microstructural parameters could play an important role. The reorientation studies were continued on neutron irradiated used fuel using hotcell facilities in order to map out the impact of several thermo-mechanical cycles on hydride

reorientation. The impact hydride reorientation can have on the mechanical behavior of the fuel has also been studied using ring tensile tests and burst tests. The development of specific image characterization methods developed at CEA were also presented.

The final storage solution for used fuel is a subject of many research and debate for countries that have operating nuclear facilities or historical ones. Repository solutions are being investigated, in France in Bures for example with the Cigeo project, and until the solutions are final, the retrievability of used fuel that is currently stored in dry casks or in large spent fuel pools is key. Recycling used fuel is also a possibility, used in France with the La Hague facility, but is an expensive process and has thus not been chosen by many countries. Understanding and predicting the mechanical behavior of current spent fuel is key but also, by being able to better predict hydrogen redistribution and hydride reorientation, it could be envisioned that future claddings could be developed that would mitigate such phenomena. The M5™ alloy developed by Framatome already solves some of these issues by having a very low hydrogen pick-up fraction thus having less hydrides available to reorient and embrittle the cladding.

As can be seen from this summary, several complex characterization techniques were used that required large user facilities (particle accelerators for irradiation, synchrotrons), large facilities to handle radioactive samples (hotlab) and also very specific techniques (TEM, SIMS, Raman, computational modeling). All these studies were made possible by the experts that are responsible for these instruments since their use is often very complex. A summary of the techniques used and their typical characteristics are given in

Table 1. The application of these techniques in the work performed on zirconium in this manuscript are also mentioned in this table. This also goes to illustrate that current research projects in material science are best conducted by having a team of researchers from different backgrounds working together and reinforce the importance of collaboration within and outside of the original research institution.

Table 1 Summary of techniques used for zirconium alloys characterization [43].

Name of the technique	Information gathered from this technique	Approximate dimensions of analyzed area	Application to zirconium alloy characterization
SEM	Microstructure	Lateral resolution in the order of tens of nm	Oxide structure and thickness, hydride microstructure observation
EDS	Chemical information	Probed depth $\sim 1 \mu\text{m}^3$	Precipitate characterization
EBSD	Crystallography	Probed depth $\sim 100 \text{ nm}$	Grain boundary characterization, intra- inter-granular hydrides
FIB	Sample preparation and tomography	Dimensions of samples prepared $0.5 \times 5 \times 10 \mu\text{m}^3$ Analyzed volume \sim tens of microns	Samples prepared at specific locations (metal-oxide interface, implantation peak), APT sample preparation
TEM	Microstructure	Lateral resolution in the order of 0.2 nm (conventional TEM)	Characterization of irradiation damage, crystallographic structure of precipitates, hydrides and other phases
EDX/EDS	Chemical information	Lateral resolution in the order of tens of nm	Chemical identification of precipitates and other phases
TEM - EELS	Chemical information, thickness and coordinance	Lateral resolution comprised between 2 and 0.1 nm (depending on the TEM used)	Thickness information of TEM samples for calculation of dislocation density
TEM - ACOM	Crystallography	Area analyzed : $5 \times 5 \mu\text{m}$	Orientation of oxide grains (nm scale)
APT	Chemical information and nanostructure	Lateral resolution in the order of 0.1 nm, depth resolution in the order of the nm Analyzed volume : a few hundreds of nm^3	Observation of smallest precipitates and clusters, diffusion of elements in sample
Synchrotron XRD	Crystallography and stress state	Area probed : between a few microns to a few mm	Crystal structure, hydride dissolution and precipitation, stress-state of hydride/zirconium matrix
XANES	Oxidation state	Area probed : between a few microns to a few mm	Studying oxidation behavior of various zirconium alloys
EXAFS	Coordinance and nearest neighbors	Area probed : between a few microns to a few mm	Study of clusters and oxidation of zirconium alloys

3 In-reactor degradation of aluminum alloys

In order to develop better performing alloys for LWRs such as mentioned in the previous paragraph, new concepts must first be tested in research reactors, in particular in Material Test Reactors (MTRs) in order to understand their behavior under neutron irradiation. In France, the JHR is an MTR currently being built in the CEA Cadarache site in order to replace former MTRs that have reached their end of life such as Osiris which is located on the CEA Saclay site. The core of these reactors is made of aluminum components. In order to operate safely the reactor, the behavior of these aluminum components has to be understood and predicted. The research presented in this section focused on a few select issues that aluminum alloys used in MTRs can encounter.

The 6xxx aluminum alloy series (Al-Mg-Si(-Cu)) is one of the most widely used age-hardened alloy series due to its high specific strength, formability, weldability, corrosion resistance and relatively low cost. The alloy series is commonly used within the architectural, marine, automotive, aerospace, recreational and nuclear domains. The 6061-T6 aluminum alloy has been selected for the core vessel of the Jules Horowitz Materials Research Reactor (JHR), which is being constructed by CEA in France. Aluminum alloys are commonly used in water-cooled research reactors due to the alloy's high neutron transparency, low gamma ray induced heating and high thermal conductivity. Alloys from the 6000s series also have good mechanical properties. The widespread use of the 6xxx alloy series has led to an extensive research effort into optimizing the alloy series' mechanical properties with particular focus being placed on the nanometer-scale metastable phases that are present either prior to or at the "peak-hardness" aged condition. The number, size, morphology and type of precipitates that form during ageing is a complex function of the alloy composition and thermomechanical processing.

The material issues that are investigated in the following paragraph are a selection of all those that have to be considered when designing a reactor and choosing the optimal parameters for each component of the reactor core in terms of material science. The first issue discussed is aluminum corrosion, in particular corrosion of the core internals that could impact the capacity to cool the reactor and thus its safe and efficient operation.

The second part of this section will group several studies that attempt to link microstructural characterization of the material with understanding and predicting its behavior under irradiation. For these experiments, ion irradiation was extensively used to conduct separate effect experiments and fine-tune the parameters impacting the alloy in order to study specific phenomena. Among other, swelling of aluminum components, hardening and fracture toughness evolution under irradiation will be presented in section 3.2.

3.1 Corrosion

General corrosion of aluminum alloys used for nuclear applications

In this section, the chemical and physical phenomenon we are focusing on is the corrosion of the aluminum components of the reactor core. The work presented in this section has been mainly performed during S. L'Haridon-Quaireau's PhD thesis on the 6061-T6 alloy which I supervised as well as during D. Nabhan's PhD thesis on the AlFeNi alloy which I co-supervised. During

operation in material testing reactors (MTR), the AA-6061-T6 alloy used for core components is covered by aluminum hydroxide. At a temperature above 80°C, the main crystalline phase of aluminum hydroxide is boehmite (γ -AlOOH) [44, 45]. However, part of the core structures in MTR are at a lower temperature, below 70°C, where the main hydroxide phase is bayerite (α -Al(OH)₃). This change of hydroxide phase at 70/80°C has an effect on the corrosion and in particular on the corrosion rate of aluminum according to Hart [46]. Since the operating temperature envisioned for the core components of future MTRs is envisioned to be around 70°C, new quantitative measurements are required at these temperature to complete the available data in the literature in order to improve the application ranges of existing empirical models used to predict corrosion behavior. The effects of several parameters on pitting and uniform corrosion of the aluminum alloy 6061-T6 in the conditions found in MTR for the core structures are investigated, in particular: temperature (70-100 °C) and pH (5 and 7.5). The choice for these two main parameters was made after studying literature results on this subject [47] as well as based on previous studies on the AlFeNi alloy that can be used for fuel components [48, 49]. After corrosion experiments, conducted in an autoclave, characterization techniques are used to observe the formed hydroxide, its composition and crystallographic structure (TEM, SEM, EDX, XRD, micro-Raman spectroscopy and electron diffraction) and formulate hypotheses on the mechanisms of corrosion at play.

At temperatures that are at the lower end of our studied temperature range (70 °C), the film is composed of several layers of different aluminum hydroxide phases. Figure 28(a) presents a cross section of the film observed with a TEM. This film was obtained after a corrosion test at 70 °C for 10 days in 2.8L of solution at a constant pH of 5. The film is composed of three layers: an inner, an intermediate and an outer layer. To characterize further the hydroxide at 70°C, microanalyses are performed on each layer: μ -Raman analysis and/or electron diffraction. The outer layer is composed of micro-sized crystals. The inner layer in contact with the metal is compact as illustrated in Figure 28. The intermediate layer is composed of needle-shaped nanocrystallites. Selected Area Electron Diffraction (SAED) is performed on these two layers, the electron diffraction patterns are presented Figure 28b. and c. The two layers are composed of boehmite (γ -AlOOH). However, the presence of boehmite at 70°C is not in accordance with the phase diagram of aluminum hydroxide: according to Wefers and Misra [45], only bayerite should be present at 70°C, thus, boehmite is metastable in the conditions of this study. In addition, the micrometric precipitates of the alloy do not change the layered microstructure and the crystalline composition of the aluminum hydroxide as was confirmed by μ -Raman analyses performed at several points in aluminum hydroxide pits.

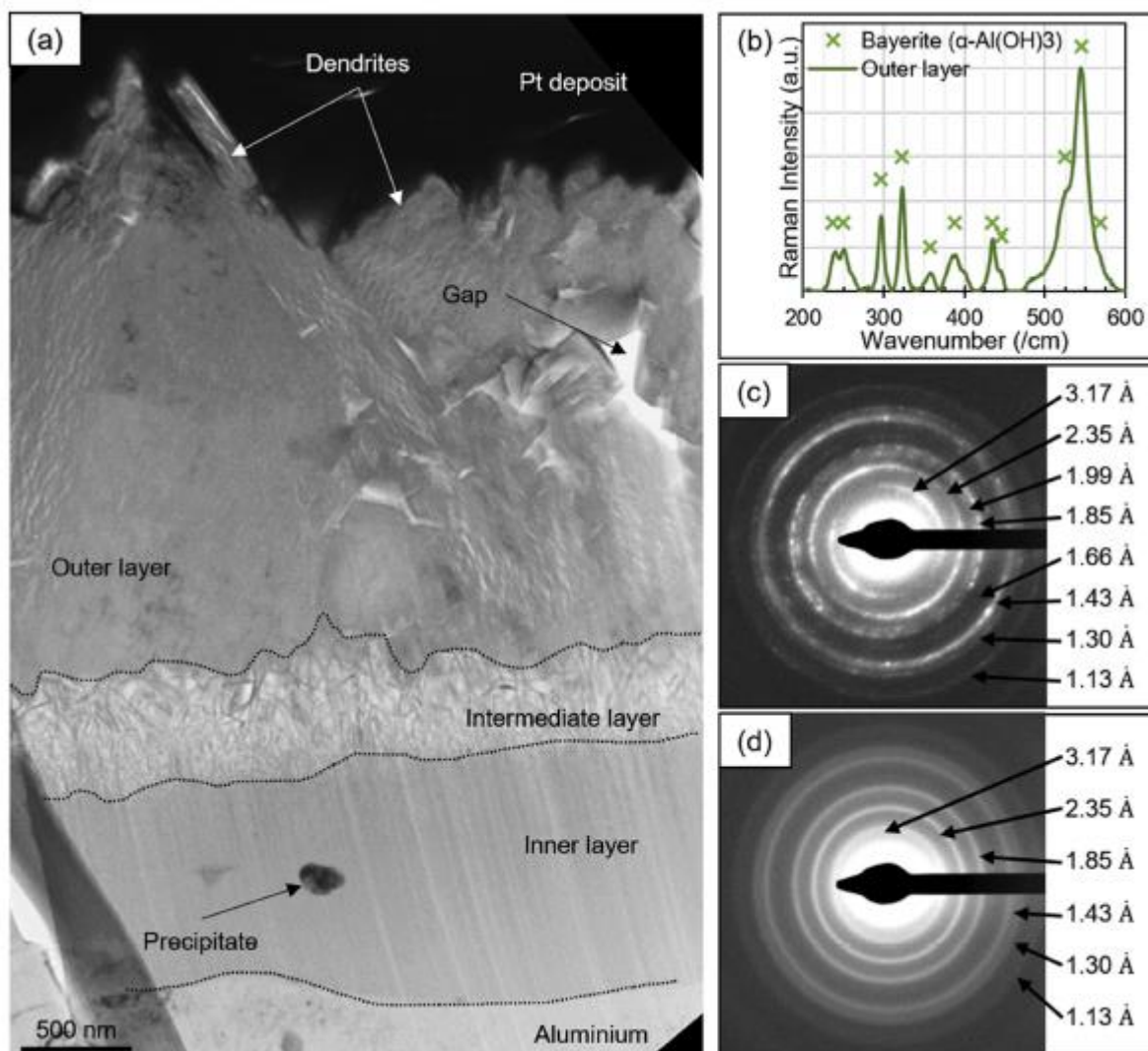


Figure 28 (a) Micrograph of a cross section of the aluminum hydroxide film in bright field imaging (TEM), (b) μ -Raman pattern obtained on the outer layer, and selected area electron diffraction patterns obtained from (c) the intermediate layer (TEM); obtained after corrosion at 70°C for 10 days in 2.8 L of solution at a constant pH value of 5 [50].

The detailed characterization presented above were made possible by the use of TEM and μ -Raman spectroscopy. Bayerite (outer layer) and boehmite (inner layer) do not have the same properties (density, hydration, solubility) thus, these two layers have different corrosion behaviors (dissolution, growth) depending on the parameters of corrosion). In particular the pH is likely to have a strong impact on the corrosion kinetics of the two aluminum oxide phases. Corrosion experiments were thus performed using two types of autoclaves (a small volume 0.065L autoclave and a large volume 2.8L autoclave) in order to study the pH effect. Using a combination of TEM, SEM (to observe corrosion pits), weight gain measurements, and μ -Raman spectroscopy, as well as chemical characterization of the autoclave media by ICP-AES (inductive coupled plasma atomic emission spectroscopy) it was observed that the pH has a strong impact on the outer layer but not on the inner layer.

The pH variations modify the stability of the aluminum hydroxide according to Equation (3).



The chemical equilibrium of precipitation/dissolution of aluminum hydroxide is determined by the solubility of bayerite. This solubility depends on pH and temperature. Figure 29a. presents the solubility of bayerite at 70 °C calculated by Chivot [51]. The aluminum concentration measured by ICP-AES during the corrosion tests in 0.065L and 2.8L are also reported in Figure 29a. According to Figure 29a., an increase of pH from 5 to 8 causes an increase of the solubility and thus, an increase of the concentration of ions Al(III) present in the autoclave medium. According to Wintergerst et al. [48], the outer layer of the hydroxide film is formed by precipitation of ions Al(III) on the surface of the samples. The increase of solubility with the pH has a strong impact on the precipitation of ions Al(III) and thus on the outer layer. Figure 29b. presents the thickness evolution of the outer layer as a function of the final pH. Regardless of corrosion time and volume of solution, this thickness increases linearly with pH.

To summarize, from this study we can infer that a pH of 5 limits aluminum corrosion compared to a pH of 7.5 for the 6061-T6 aluminum alloy. This corrosion difference is due to the evolution of solubility of aluminum hydroxide between the two pH: the high solubility at pH 7.5 decreases the stability of the film of aluminum hydroxide and thus, increases the aluminum corrosion.

The increase of pH during corrosion, observed in the smaller sized autoclaves, is due to the oxidation of the magnesium present in the alloy. This oxidized magnesium comes from the micrometric Mg₂Si particles present in the alloy initially. By releasing magnesium in solution, the corroded Mg₂Si particles increase the pH of the solution. The stability of aluminum hydroxides depends on the pH through their solubility. By increasing the pH, corrosion of the Mg₂Si particles increases the solubility of aluminum hydroxides and thus, aluminum corrosion.

Pitting corrosion was also studied and found to be linked to the corrosion of the iron-rich intermetallic inclusions present in this alloy. However, the effects of corrosion pits on the overall corrosion of the 6061-T6 alloys was found to be of a second order compared to the general corrosion behavior and does not need to be taken into account in the empirical models to predict corrosion behavior.

Corrosion models are used to predict the hydroxide thickness for a safe and efficient operation of MTRs. They are based on empirical correlations between hydroxide thicknesses, testing time and corrosion conditions (pH, temperature, heat flux and flow rate) [52-54]. The current models have the following general form:

$$X_{ox} = X_0 + k * t^p \quad \text{Equation 4}$$

Where X_{ox} and X₀ are the oxide thicknesses and t the time (X₀ is the thickness at t = 0). The coefficients p and k depend on pH, temperature, heat flux and flow rate. Depending on the observations done during corrosion tests, these parameters are adjusted using data obtained after corrosion tests at high temperature, above 100 °C [47, 52, 53, 55-57].

The data obtained from this study raises the question of the applicability of these models at low temperature (70 °C). In particular, a distinction between the two layers needs to be done in the empirical correlations used to predict the hydroxide thickness in MTR. However, additional corrosion tests at different temperatures inferior to 70°C are needed to adapt the coefficients of the empirical correlations.

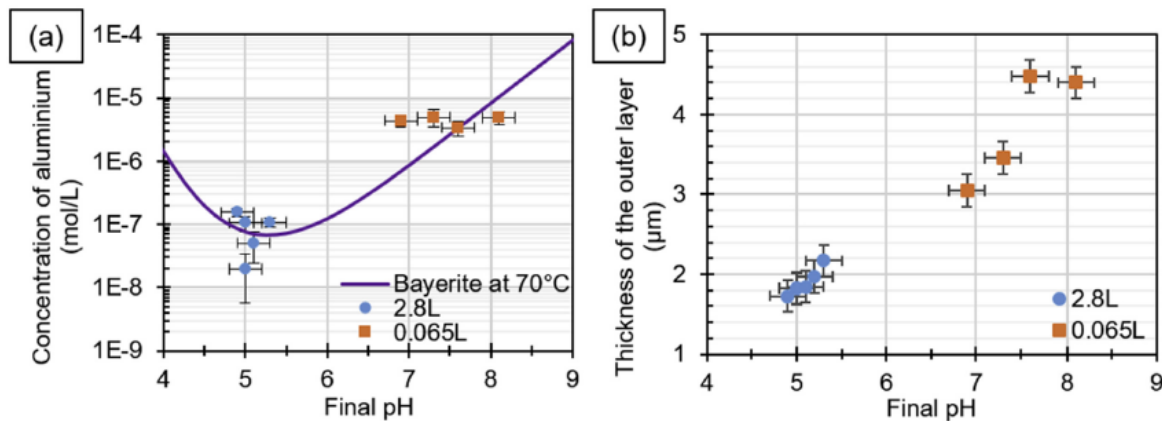


Figure 29 (a) Concentrations of aluminum measured in the two autoclave volumes, 0.065L and 2.8L, and solubility of bayerite calculated by Chivot [51] depending on the pH, and (b) thickness of the outer layer of the film depending on the final pH in the two volumes, 0.065L and 2.8L at 70°C [50].

Similar studies were conducted on the AlFeNi aluminum alloy which is envisioned to be used for fuel plates of MTRs such as JHR [49, 58]. The main difference with the 6061-T6 studies is that the temperature and irradiation conditions are likely to be much more severe for the fuel plates. The operating temperature of the water moderator can reach up to 250°C in incidental conditions and circulates with a high velocity between the AlFeNi aluminum fuel plates. The impact of pH of the water moderator, surface finish of the plates and various thermal treatments of the AlFeNi alloy have been studied in the small corrosion autoclaves (0.065L). The main results from this work are that, on all specimens tested, the only crystalline phase formed is boehmite. For short corrosion times (<25 days) the corrosion kinetics increase with increasing pH, which is in agreement with previous results obtained in a corrosion loop. However for long durations, beyond around 30 days, the effect of pH is harder to characterize due to the evolution of the pH in smaller autoclaves. The effect of the pH in this range appears to be reduced for the unpolished specimens. As generally observed in other alloys, unpolished specimens corrode faster than the polished ones however it is difficult to implement polishing of reactor core component or fuel plates from an industrial faisibility point of view. On the contrary, the thermal treatment (cold-rolled/annealed) of the unpolished samples had no impact on the corrosion kinetics, except after 34 days. It is explained by the fine surface layer microstructure resulting from the rolling step which was hardly affected by annealing.

An important parameter that was not studied in the two previous studies presented on 6061-T6 and AlFeNi alloy is the velocity of the moderator circulating in the reactor core. Indeed, above a certain flow rate, the erosion from the water is added to the natural dissolution of the aluminum alloy and may lead to higher corrosion kinetics and faster reduction of the remaining metal. The study of this parameter is envisioned for future research projects at CEA.

Effect of irradiation on aluminum corrosion

As seen for zirconium alloys, in reactor core, irradiation can also play an important role on corrosion kinetics. The study presented below focuses on the effect of irradiation in the corrosion of the core components of MTRs which are composed of the 6061-T6 alloy. In nuclear research reactors, aluminum alloys are corroded and an aluminum hydroxide film covers their surface. Defects created by neutron irradiation can have a detrimental effect on this corrosion. In the study led during S.

L'Haridon-Quaireau's PhD thesis [59, 60], the effect of both ion irradiation and neutron irradiation on aluminum corrosion have been studied. Two types of ion irradiations have been performed on a 6061-T6 aluminum alloy using the Jannus particle accelerator user facility located at the CEA-Saclay. The first irradiation experiment aimed at studying the effect of metal matrix irradiation on aluminum corrosion. The second irradiation experiment aimed at studying the effect of hydroxide irradiation on aluminum corrosion. A summary of the irradiation and corrosion experimental plan for this work is presented in Table 2.

The ion irradiation was chosen in order to perform various specific irradiation (on the metal or on the hydroxide) and adjust irradiation parameters to investigate relevant conditions. For the hydroxide film irradiated with Al ions of 1.2 and 5 MeV, the displacement per atom is at most 2.5 dpa. For the aluminum matrix irradiated with Al ions of 1.8 MeV, the maximum dose is at most 8 dpa as calculated with SRIM. The effects of ion irradiation are investigated by TEM and SEM observations. The crystalline structure of aluminum hydroxide is studied by electron diffraction, μ -Raman and X-rays diffraction. In the aluminum hydroxide film (composed of a mix of bayerite, α -Al(OH)₃, and boehmite, γ -AlOOH, before irradiation), ion irradiation causes the formation of voids and dehydrates the aluminum hydroxide (nanocrystallites of η -Al₂O₃ are observed in the irradiated film) as illustrated in Figure 30. In the aluminum matrix, irradiation increases the dislocation density as seen in Figure 31 and amorphizes dispersoids [60].

After ion irradiation, samples are corroded at 70 °C in 2.8L of demineralised water. The two irradiations increase aluminum corrosion quite significantly as seen by the oxide thickness measurements (from SEM micrographs) as well as the weight gain measurements (see Figure 32). This increase of aluminum corrosion could be due to the amorphization of dispersoids and to the increase of dislocation density. Similar observations have been made in corroded irradiated AlFeNi aluminum alloy [61]: uncorroded samples were irradiated with Al ions for 18 dpa and were then corroded at 140 °C, for 16 days in 0.065L of solution at pH 5.2. The irradiated samples were also more corroded in this case.

Table 2 Experimental plan used to study the effect of irradiation in aluminum corrosion [60].

Impact of ion irradiation on aluminium hydroxide	Step 1: corrosion 7 days, 70°C, Demineralized water	Step 2: ion irradiation 5 and 1.2 MeV, Max 2.5 dpa in the aluminium hydroxide, 20°C	Step 3: corrosion 4 days, 70°C, Demineralized water
Impact of ion irradiation on aluminium matrix	Step 1: ion irradiation 1.8 MeV, Max 8 dpa in the Al matrix, 20°C	Step 2: corrosion 4 days, 70°C, Demineralized water	
Impact of neutron irradiation	Neutron irradiation 272 and 383 days, 6.7 and 10 dpa in the Al matrix, + Corrosion 42°C, pH 6		

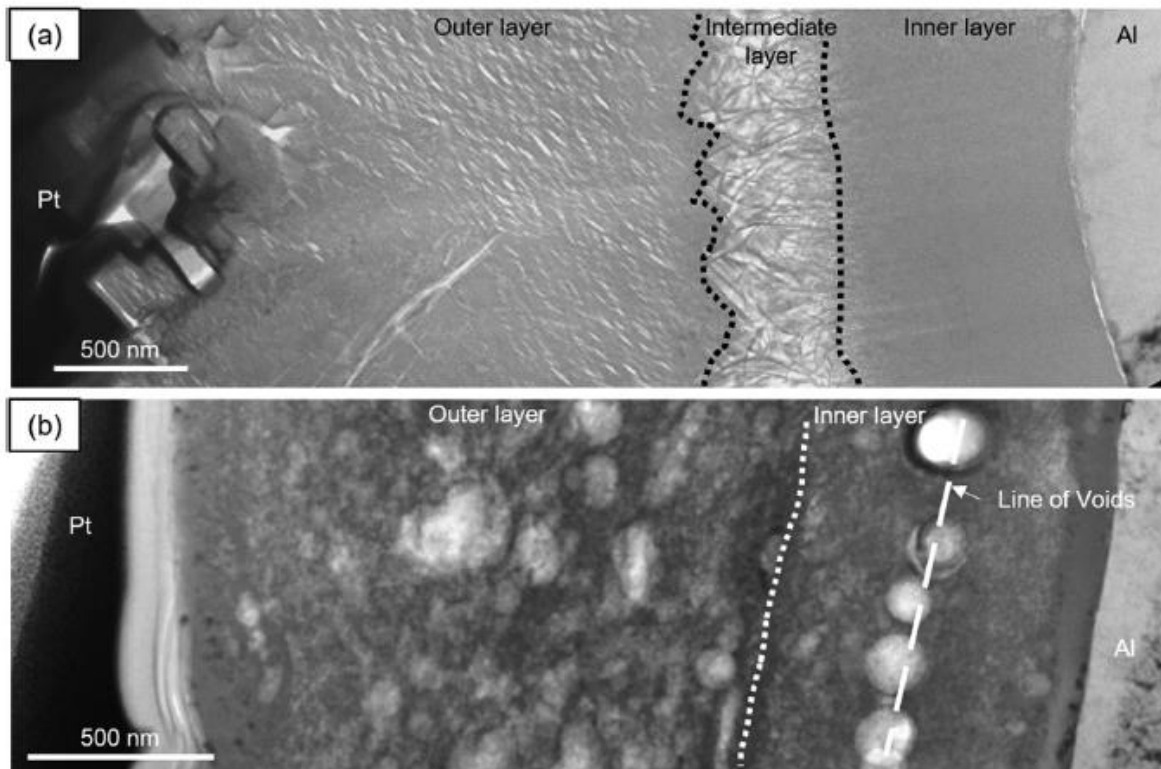


Figure 30 TEM micrographs of (a) a unirradiated film of aluminum hydroxide (obtained on samples corroded at 70°C, in 2.8L of demineralized water and for 7 days), (b) a film irradiated with Al ions of successive energies 5 MeV then 1.2 MeV [60].

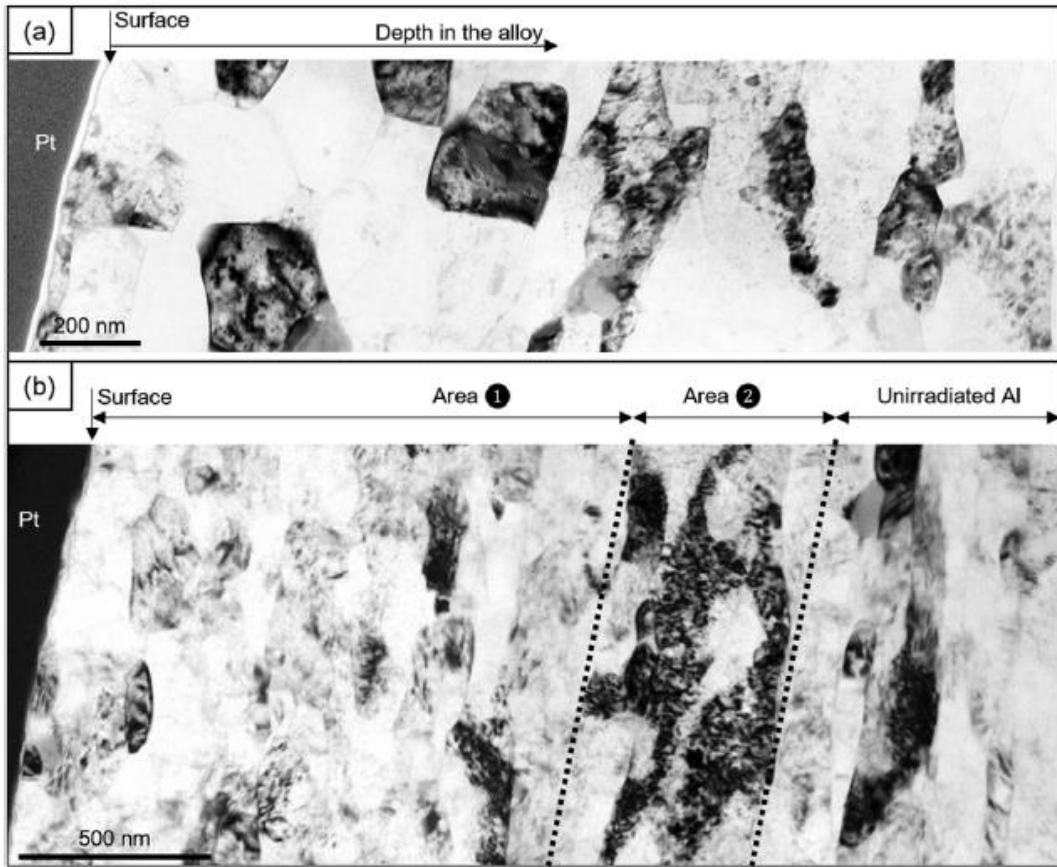


Figure 31 TEM micrographs of (a) an unirradiated matrix of 6061-T6 aluminum alloy and (b) irradiated matrix with Al ions of 1.8 MeV. The areas 1 and 2 correspond respectively to the area irradiated at 1-5 dpa (displacement per atom) and to the most irradiated area at 8 dpa. The boundary between area 1 and 2 is the start of the implantation peak (peak calculated with SRIM) [60].

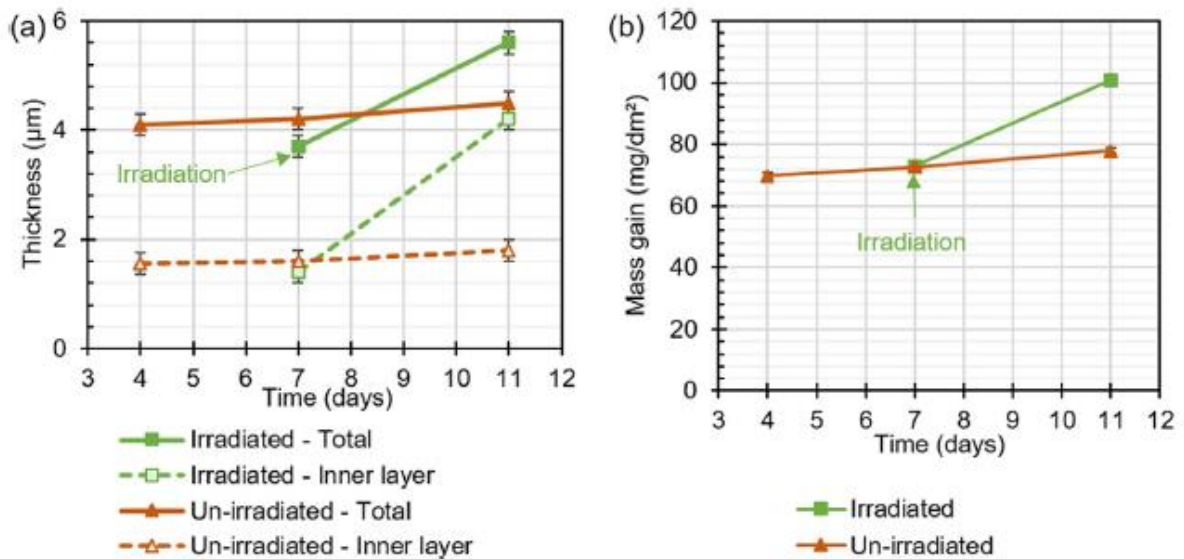


Figure 32 (a) Average thickness of the aluminum hydroxide film and (b) average mass gain of the samples unirradiated and irradiated with Al ions of successive energies 5 MeV then 1.2 MeV (the term ‘irradiation’ on the graphic indicates when the ion irradiation occurs) [60].

The second part of this work studied samples corroded in the Osiris nuclear research reactor located at CEA Saclay, in water at 42 °C, with a pH of 6 and for 18 months. The samples were prepared in a hotcell for SEM observation by fracturing the samples in order to perform fractography on the oxide surface. The aluminum hydroxide film observed on these samples and presented in Figure 33 has a layered microstructure composed of a compact inner layer, a thick intermediate layer and an outer layer of cuboid microcrystals. Silicon enrichment measured by EPMA is observed in the inner layer. TEM has not yet been performed on these samples due to the difficulty to prepare TEM thin film of aluminum in hotcells and gloveboxes (for the final polishing step). The sample preparation is still underway and has taken a longer time than the duration of the PhD work of S. L'haridon-Quaireau. This illustrates one of the complexity of working with neutron-irradiated material for fine characterization methods such as TEM.

The effects of ion and neutron irradiation on aluminum corrosion can however be compared in this study.

Some similarities are observed between ion and neutron irradiations. Films formed in nuclear reactor and obtained after ion irradiation and re-corrosion have a similar crystalline structure. Indeed, at 70 °C, the aluminum hydroxide film irradiated with Al ions and then re-corroded is composed of a mix of boehmite (γ -AlOOH) and bayerite (α -Al(OH)₃), and the main crystalline phase is boehmite. For a similar temperature (70/90 °C), the film obtained in MTRs has the same crystalline structure (i.e. the main crystalline phase in the XRD patterns is boehmite with traces of bayerite). In addition, the film has a similar layered microstructure after ion irradiation and re-corrosion, and during corrosion tests with neutron irradiation. The two types of irradiation increase aluminum corrosion and accelerate the aluminum hydroxide growth on the samples surface. Because of these similarities, ion irradiation can be used during un-activated corrosion tests in corrosion loops or in autoclave in order to be closer to the conditions found in MTRs. However, silicon enrichment is observed in the film obtained in nuclear reactor, this enrichment is not observed during unirradiated corrosion tests. Silicon ions can be used during ion irradiation in order to simulate the silicon enrichment in the film.

Nevertheless, in this study, we can observe some limitations to the use of ion irradiation to simulate the damage created by the fast neutron flux in reactor. Ion irradiation leads to a dehydration of the aluminum hydroxide. The damage due to this dehydration (nanocrystallites of η -Al₂O₃) may not be observed in aluminum hydroxide irradiated in a nuclear core (SAED should be performed on the samples corroded in the Osiris reactor to answer to this question). In addition, to irradiate the aluminum hydroxide film, the corrosion tests are interrupted and the samples are exposed to air during the break of corrosion tests. Wintergerst observed an effect of autoclave openings during corrosion tests: the hydroxide thickness is less important during interrupted corrosion tests than uninterrupted ones [48]. It means the thickness measured in this study may be underestimated because of the interruptions to irradiate the aluminum hydroxide.

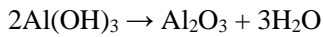
Based on the work performed during this PhD thesis, a mechanism for aluminum corrosion under irradiation was proposed and is illustrated in Figure 34. It should be noted that the proposed mechanisms apply to ion irradiation and not to neutron irradiation or to in-core irradiation in general.

1. Before ion irradiation, due to corrosion tests, the aluminum matrix is oxidized. At the interface hydroxide-metal, this oxidation reaction is accompanied by the reduction of water and dioxygen, and the production of OH hydroxide groups. A part of this oxidized aluminum reacts with the OH hydroxide groups to form boehmite (γ -AlOOH), the inner layer, at the hydroxide-metal interface (internal growth). The rest of the oxidized aluminum diffuses through the film and is released as ions Al(III) in the

corrosive solution. These ions then precipitate on the samples surface to form bayerite ($\alpha\text{-Al(OH)}_3$), the outer layer (external growth) as illustrated in Figure 34(a).

2. During ion irradiation, the former aluminum hydroxide is dehydrated and a change of microstructure is observed (Figure 34b).

3. After irradiation, during the re-corrosion of the samples, the irradiated film is a part of the new inner layer: at 70 °C, alumina obtained from dehydrated aluminum hydroxide is rehydrated by water to form boehmite, the crystalline phase of the inner layer. Due to the non-protective quality of this irradiated film, the matrix is oxidized and aluminum is released in solution. A new outer layer is formed by the precipitation of aluminum ions in solution on the samples surface (Figure 34c.). The proposed global reactions are:



When the samples are reintroduced in the autoclave containing water for the corrosion test after irradiation, the Al_2O_3 layer is firstly hydrated to AlO(OH) (formation of boehmite, the most thermodynamically stable specie) and the corrosion is observed again with the formation of Al(OH)_3 at the interface $\text{AlO(OH)}/\text{solution}$ following the mechanism previously described.

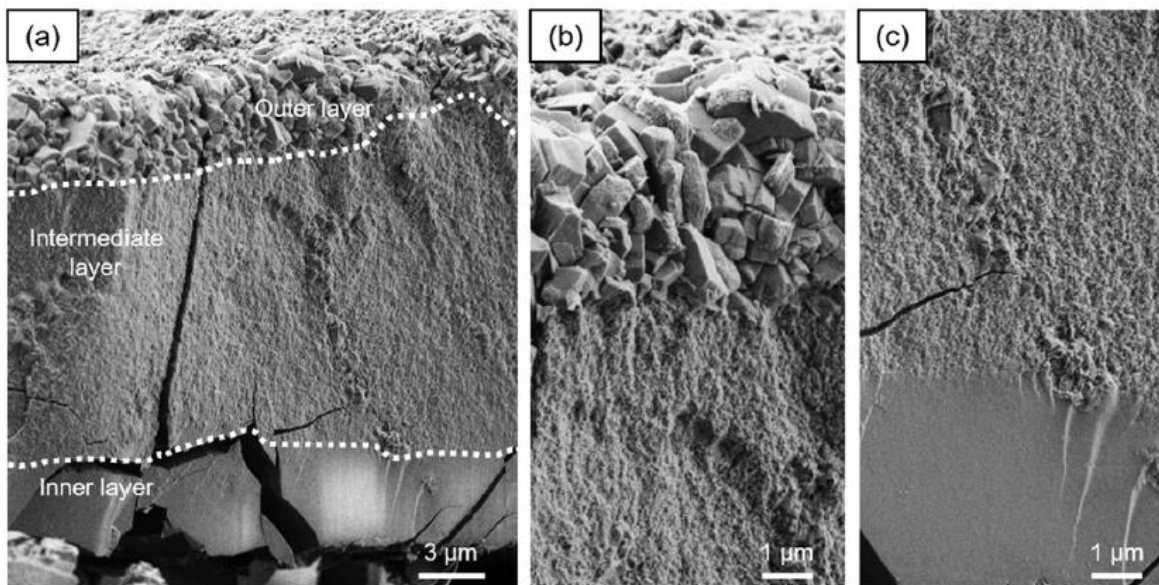


Figure 33 SEM micrographs of (a) the film obtained on a sample corroded for 560 days at pH 6 and at 42°C in the reactor Osiris ; zoom on (b) the outer and intermediate layers and on (c) the intermediate and inner layers [60].

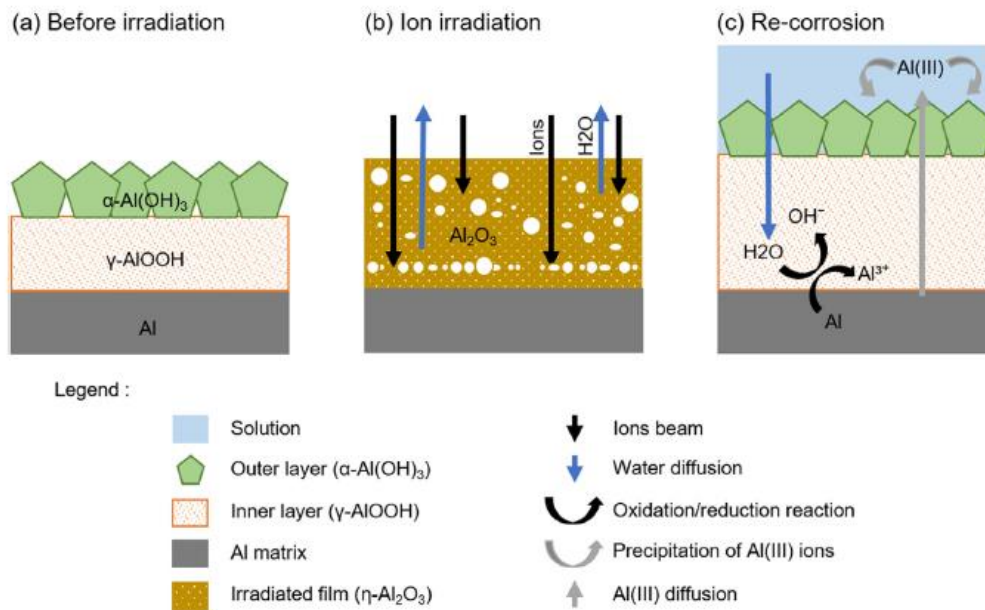


Figure 34 Schematic of the three steps of the proposed mechanisms of aluminum corrosion during corrosion tests coupled with ion irradiation [60].

Summary of studies on aluminum corrosion for nuclear applications

In this paragraph, several studies on the corrosion of aluminum alloys for MTRs have been presented. Firstly, the impact of various parameters on the corrosion of unirradiated samples has been studied. In particular, since most of the works published in the literature on the 6061-T6 alloy have been performed at higher temperatures, producing boehmite as the only hydroxide phase on the alloys, it was important to study corrosion at a lower temperature such as the one envisioned for the JHR (70°C). Corrosion of 6061-T6 at a lower temperature leads to the formation of bayerite in addition to boehmite and a multi-layered oxide structure. Bayerite behaves differently than boehmite and, in particular, can present faster corrosion kinetics than boehmite. It is thus necessary to perform additional corrosion experiments in order to adjust the existing corrosion empirical models used to predict the evolution of oxide thickness with time.

The second parameter of importance studied for both 6061-T6 and AlFeNi is the pH of the solution. For 6061-T6, it was observed that a lower pH is recommended to limit aluminum corrosion. The pH in autoclaves tends to vary with time due to the dissolution of the Mg₂Si particles. This is an important parameter to take into account when performing corrosion experiments. AlFeNi experiments, in particular were performed in small volume autoclaves and are thus affected by the variation of pH in the corrosive solution.

Studying corrosion on unirradiated materials was performed using an array of characterization techniques. Firstly conventional SEM was used to observe the sample surface to study pitting corrosion as well as to observe cross-sectional samples to measure oxide thickness. Secondly TEM was performed on FIB-prepared samples in order to observe the various corrosion layers and characterize their crystalline structure using SAED. Micro-Raman was also used on the oxide layers as well as grazing incidence XRD to confirm the overall crystalline structure of the oxide since it is an important parameter to predict the corrosion behavior.

Finally the effect of irradiation was studied using large user facility for ion irradiation or even MTRs and hotcells in the case of neutron-irradiated samples. The advantage of using ion irradiations was clear, in particular to investigate very specific conditions,

similarly to what has been performed to study the corrosion of zirconium alloys in the previous part of this manuscript, as well as the ease of handling non-radioactive samples. Similarities were observed when comparing ion irradiated samples and neutron irradiated samples, in particular the general oxide structure, the crystalline phase present and the increase of the corrosion kinetics. However, some differences were also observed, such as localized Si enrichment for example. This illustrates that, when studying materials for reactor application, it is indispensable to add a step of characterization of neutron-irradiated samples and thus, the use of MTRs is key for the future of nuclear materials research.

3.2 Evolution of the microstructure of 6061-T6 alloy with thermo-mechanical processing and impact of irradiation.

The 6061-T6 aluminum alloy has been a candidate of choice for the JHR core components as mentioned previously. However, in addition to understanding the corrosion behavior of this alloy, such as has been presented in the previous section, it is also necessary to understand the impact of irradiation on the microstructure and nanostructure of the alloy and the impact of these changes on the mechanical properties of the components. Thus, at CEA, several studies were conducted during a period of 10 years, mainly by PhD students as well as post-doctoral fellows. Before understanding the effect of irradiation, it is key to characterize at various scales the material and to understand the impact of varying parameters during the T6 thermo-mechanical treatment on this microstructure. Indeed, it has been observed in the literature that slight variations in temperature, quench rate or ageing durations may have a strong impact on the mechanical properties of the materials, and thus, it likely has an impact on the microstructure as well. During my work at DMN, I have co-supervised two PhD students (V. Garric and T. Petit) and a post-doctoral fellow (K. Buchanan) on these subjects. In addition, being an Atom Probe Tomography (APT) specialist in my department, I have also been involved in C. Flament's PhD thesis to characterize the nanostructure of the alloy in the unirradiated and in the ion-irradiated state.

In Figure 35, I have represented the thermo-mechanical treatment necessary to obtain the T6 condition and have placed the various studies in which I was involved. Figure 36 represents the various precipitates present in the 6061-T6 alloy and their different effects on the material properties. The intermetallics are micronic-sized particles, the dispersoids are sub-micronic particles and the nano-phases (also called hardening phases) are nanometric particles.

The first study that will be detailed in section 3.2.1 is Flament's PhD work that first characterized at the nanometer scale the 6061-T6 alloy and the impact of irradiation on the various precipitates identified in the unirradiated state.

Buchanan's work focused on the Si enrichment that the alloy undergoes under irradiation due to aluminum transmutation and how this enrichment impacted the alloy nanostructure. Using TEM and APT, the regular 6061-T6 alloy was characterized as well as an artificially Si-enriched alloy. Results for this work are presented in paragraph 3.2.2.

Garric's PhD thesis focused on the impact of the varying quench rate that can be seen in the alloy during processing, in particular due to the fact that for reactor core component, thick sections will be manufactured which could induce varying cooling rates through the thickness of the component. Characterization of the microstructure and the mechanical properties were investigated as a function of the quench rate in order to define an optimal quench rate for reactor core components. Results from this work are presented in section 3.2.3.

Petit's PhD thesis had the goal of understanding the evolution of fracture toughness of the alloy with irradiation, in particular understanding the brutal fracture behavior observed in some neutron irradiated alloys called 'pop-ins'. In order to understand the mechanical behavior of the alloy, the microstructure was investigated at many different scales and using many different complex characterization techniques such as synchrotron X-ray tomography, APT and EBSD for example. The work from this PhD study is presented in section 3.2.4.

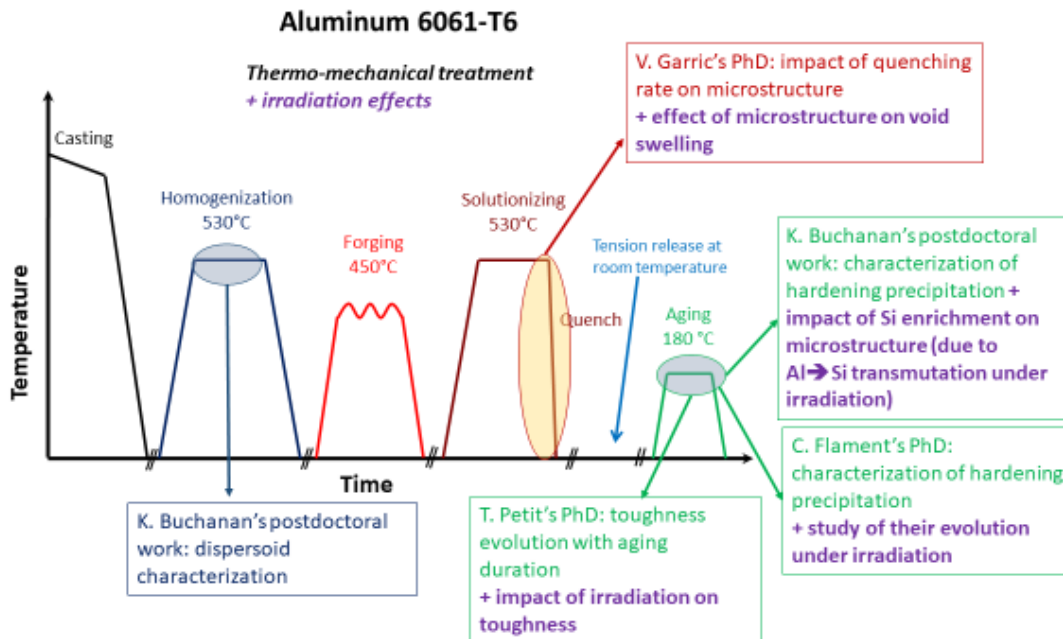


Figure 35 Organization of studies on microstructure evolution during thermo-mechanical processing of the 6061-T6 alloy and the link with the study of the impact of irradiation on the alloy.

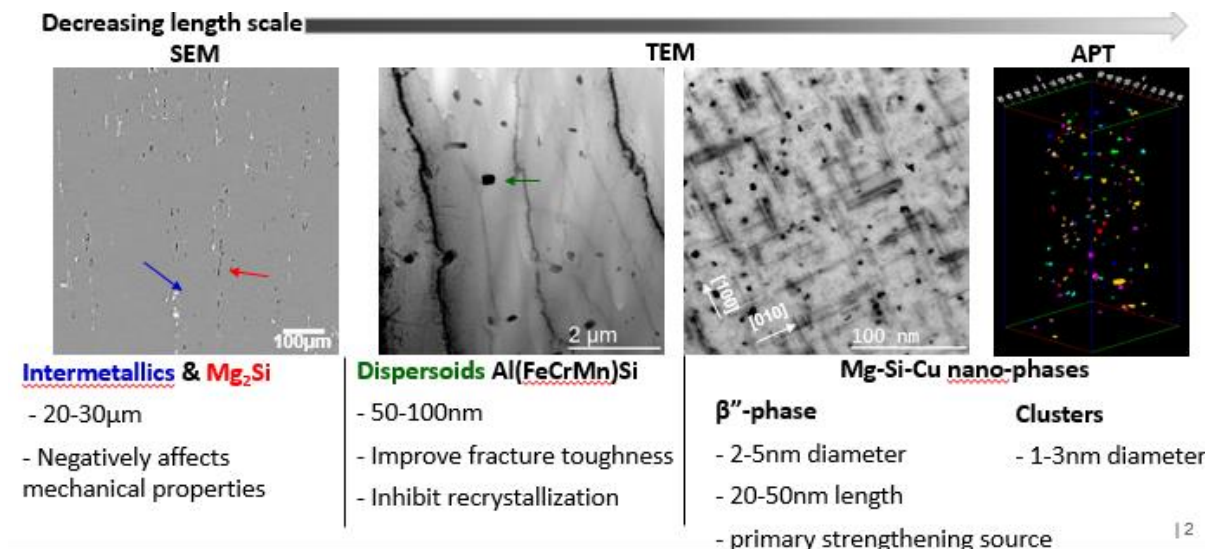


Figure 36 Description of the precipitates present in 6061 alloy at the T6 condition [62].

3.2.1 Characterization of the nanostructure of the 6061-T6 alloy and impact of ion-irradiation (C. Flament)

The high strength of Al-Mg-Si alloys is due to the precipitation of the nano-scaled phases β'' during a T6 heat treatment at $\sim 170^\circ\text{C}$. More generally, the Al-Mg-Si alloy family decomposes from the supersaturated solid solution according to the following sequence (note this is the general precipitation sequence, additional of elements such as copper can modify slightly this precipitation sequence):

Supersaturated solid solution \rightarrow atomic clusters \rightarrow GP zones \rightarrow β'' \rightarrow β' , U1, U2, B' \rightarrow β [63-66]

β'' are metastable needles along the $\langle 100 \rangle_{\text{Al}}$ axes and semicoherent with the matrix [63]. The objective of the study from Flament's PhD thesis in which I participated was to investigate the evolution of the β'' precipitates under controlled ion irradiation at room temperatures and at different doses.

Firstly the characterization of the β'' nano-phases in the unirradiated state was performed by TEM and APT. These investigations led to the conclusions that, in the alloy of study, the β'' precipitates display a centered monoclinic structure and contain Mg, Si, Al and Cu with a Mg: Si ratio approaching 2, close to the ratio of the alloy as illustrated by the HRTEM images in Figure 37 and by the APT analysis in Figure 38.

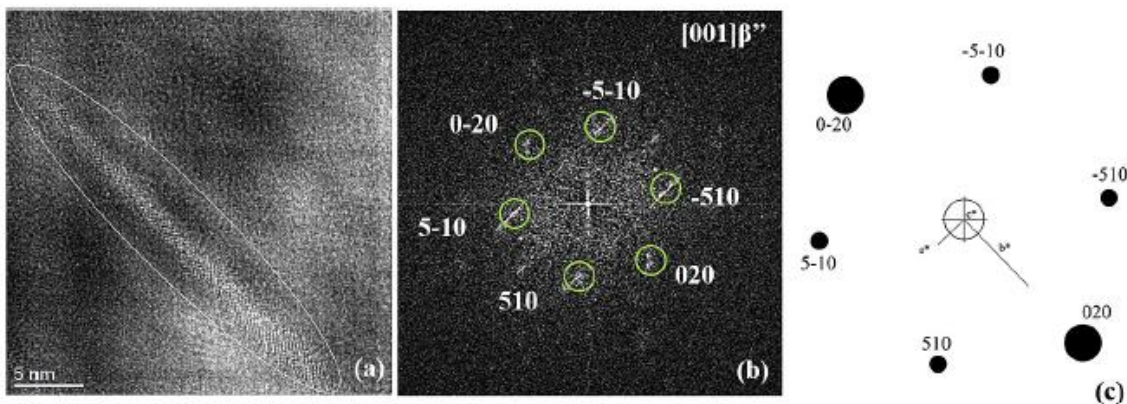


Figure 37 Crystallographic structure of β'' nano-phases (a) HRTEM micrograph of a nano-phase oriented perpendicularly to the electron beam, (b) FFT associated to (a). (c) Simulated diffractogram of a centered monoclinic structure oriented along the [001] zone axis compared to (b) [67].

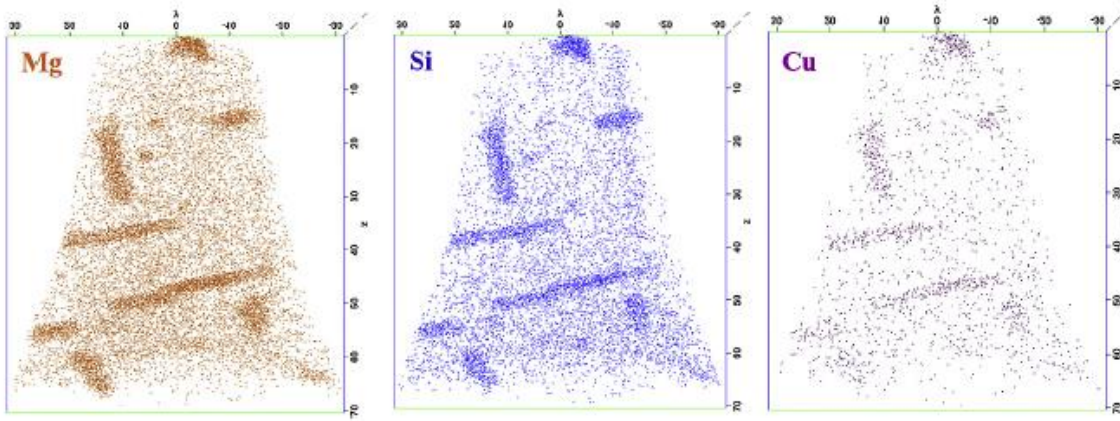


Figure 38 APT reconstruction from the un-irradiated Al 6061-T6 aluminum alloy ($60 \times 60 \times 70 \text{ nm}^3$) [67].

After 95 dpa ion irradiation, a decrease of size and a slight lattice distortion of β'' has been observed although the orientation with the matrix is unchanged. These modified β'' coexist with a new population of particles observed by dark field imaging along the [112] matrix direction as illustrated in Figure 39. Irradiation up to 165 dpa induces the full dissolution of β'' whereas the new particles grow. The microstructure of the alloy irradiated to 165 dpa has also been characterized by atom-probe tomography. An APT reconstructed volume is presented in Figure 40. Consistently with the TEM observations, no β'' needle-shaped precipitate is observed. The only features present in the tip are clusters rich in Mg, Si, Al, Cu and Cr. The Mg: Si atomic ratio is above 1 for all clusters and approaches 5 for larger clusters. Their number density is estimated to be approximately $(8.2 \pm 0.5) \times 10^{23} \text{ m}^{-3}$, which is above the one determined by TEM image analyses ($2.4 \times 10^{21} \text{ m}^{-3}$) by more than two orders of magnitude. This suggests that most of the clusters observed in the APT tip are isostructural clusters which are not observed in TEM, and that only a few of these objects have a defined structure and a common direction with the [112] direction in the Al matrix. This observation highlights the complementarity of TEM and APT when studying complex nanostructures.

TEM and APT observations have shown that these particles induced by ion irradiation do not belong to the β precipitation sequence and that they contain Mg, Si, Cu, Al and Cr. Their formation is likely driven by solute release from the β'' precipitates and from the Cr-containing dispersoids, followed by a strong precipitation driving force of Mg and Si and their growth by solute drag by vacancies or interstitials process.

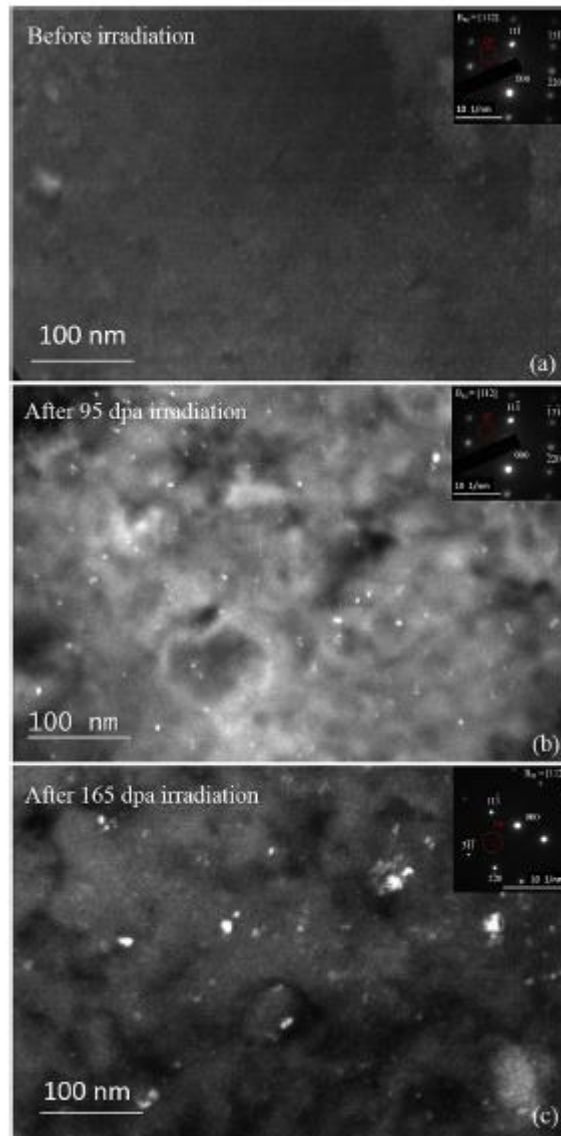


Figure 39 Microstructure of the 6061-T6 alloy along the [112] zone axis. (a) Dark Field (DF) image and diffraction pattern before irradiation. (b) DF image and diffraction pattern after 95 dpa irradiation. (c) DF image and diffraction pattern after 165 dpa irradiation [67].

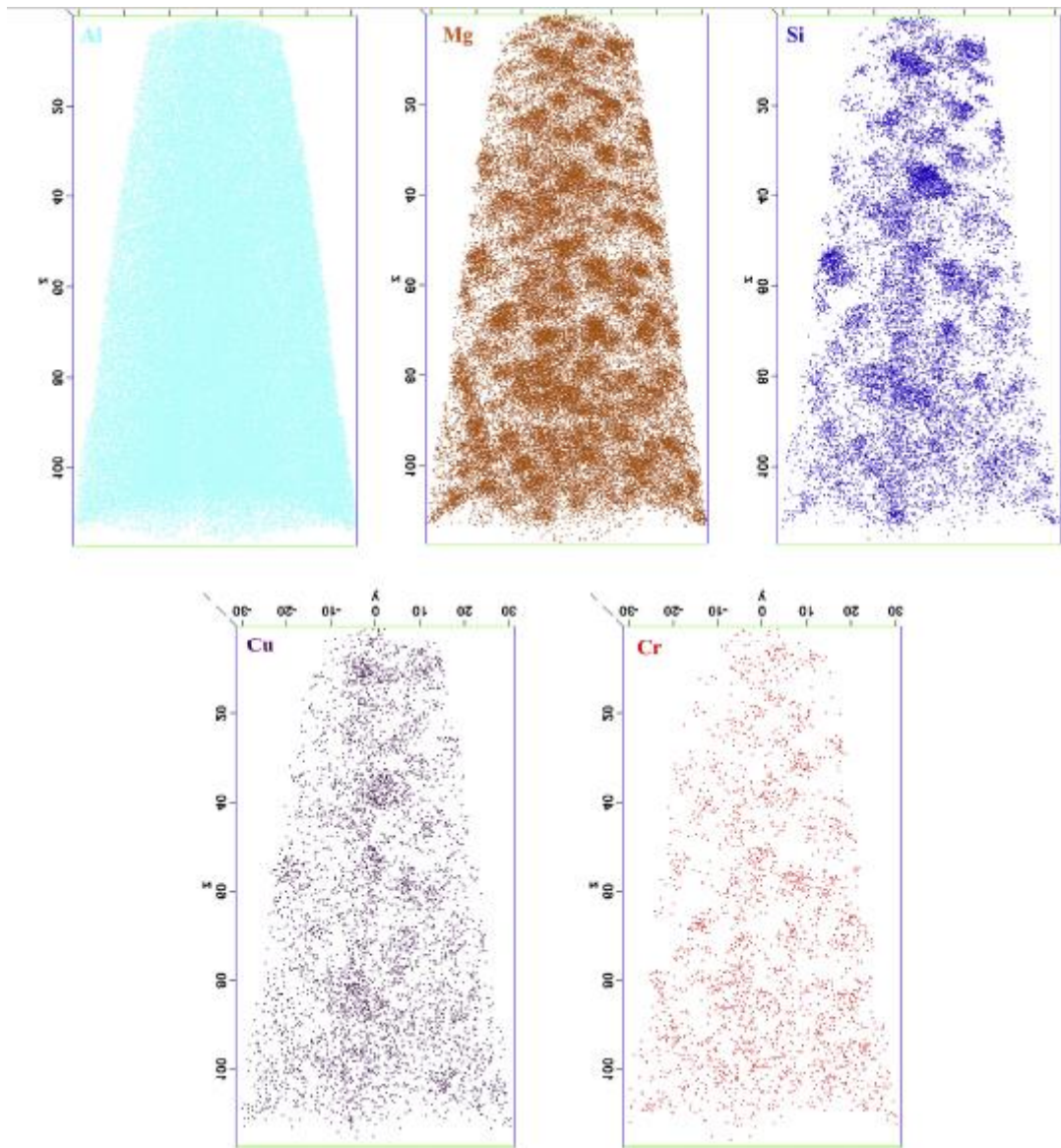


Figure 40 APT reconstruction of the 6061-T6 alloy after 165 dpa irradiation ($60 \times 60 \times 120 \text{ nm}^3$) [67].

3.2.2 Impact of Si enrichment on 6061-T6 microstructure and swelling behavior (K. Buchanan)

In this section and the following section, another physical phenomena encountered in aluminum alloys in reactor is studied: swelling of the components due to irradiation. As mentioned in Flament's work above, the 6061-T6 alloy is hardened structurally by nanometer-sized β'' precipitates (5 nm diameter needles). Chromium and manganese spherical precipitates (approximately 200 nm in diameter) induce a good recrystallization resistance for this alloy. Micron-sized inter-granular precipitates of the type Mg_2Si and iron intermetallic precipitates are also present in the alloy. Under irradiation, the fast component of the neutron spectrum (ie the most energetic neutrons in the spectrum) leads to irradiation cascades in the material which in turn lead to dissolution of the nanometer-sized β'' precipitates [68]. The point defects created by displacement cascades agglomerate into clusters. Auto-interstitial atoms form interstitial dislocation loops and vacancies form cavities [68, 69]. In addition the thermal component of the neutron spectrum (ie the least energetic neutrons in the spectrum) leads to transmutation of aluminum atoms

into silicon atoms. When above the solubility limit, silicon atoms precipitate as diamond-structure nanometer-sized precipitates. The microstructural evolutions described induce changes in the mechanical behavior and irradiation-induced swelling.

The first objective of the study presented below, performed during K. Buchanan's postdoctoral fellowship which I co-supervised, is to bring elements of understanding on the effect of silicon enrichment due to aluminum transmutation on the microstructure and on the mechanical properties of the alloy. This study was conducted on two unirradiated alloys: a standard alloy with typical 6061 composition and a Si-rich alloy which simulates the effect of high dose transmutation.

The nano-scale clusters and precipitate phases that are present in peak-hardness aged Al-Mg-Si(-Cu) alloys based on the 6061 specification have been investigated using TEM and APT for both alloy compositions. Examples of the APT analysis for both alloy are presented in Figure 41 and Figure 42. Needle-shaped precipitates that are orientated in the three orthogonal $\langle 001 \rangle_{Al}$ directions and rich in Mg, Si and Cu are dominant within each alloy's APT volumes. The lath-shaped precipitates observed by TEM are only observed within the Si-enriched alloy's APT volumes. Spheroidal particles containing Mg, Si and Cu and typically less than 5 nm in diameter coexist with the needle-shaped and lath-shaped precipitates in both alloys.

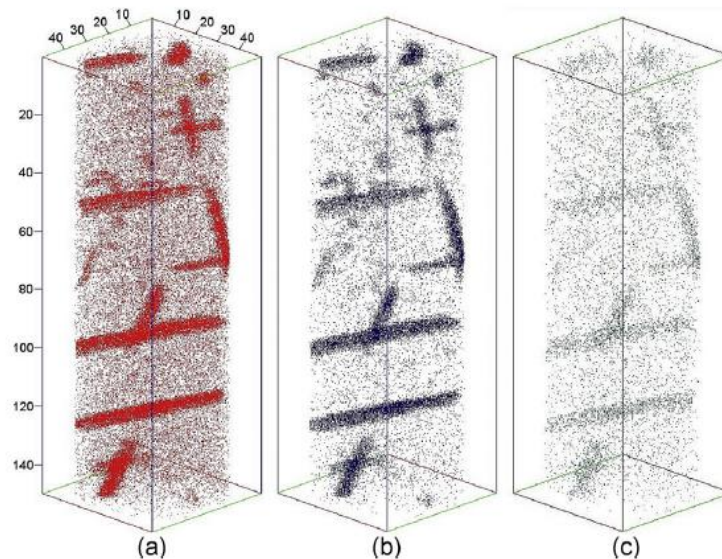


Figure 41 Three-dimensional reconstructions of the (a) Mg, (b) Si and (c) Cu atom positions for the standard 6061-T6 alloy (50 nm diameter x 150 nm length) [70].

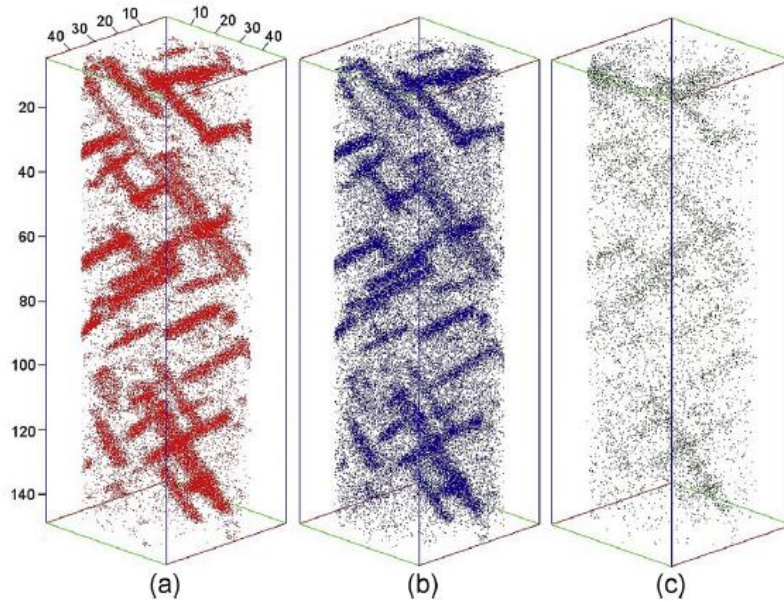


Figure 42 Three-dimensional reconstruction of the (a) Mg, (b) Si and (c) Cu atom positions for the Si-enriched 6061-T6 alloy (50 nm diameter x 150 nm length) [70].

Detailed analysis of the solute clusters observed in APT show that in both alloys the particles have solute enrichments of between 10 and 40% and are primarily composed of Mg and Si with Cu less commonly observed. On average the particles in both alloys were more enriched in Mg than Si. However, as shown in Figure 43, the particle distribution's Mg and Si contents were influenced by each alloy's overall Mg and Si contents. The standard alloy's higher overall Mg:Si ratio resulted in particles with a higher average Mg:Si ratio (1.6:1) in comparison to the particles in the Si-enriched alloy, which often contained almost equal Mg and Si contents (1.1:1).

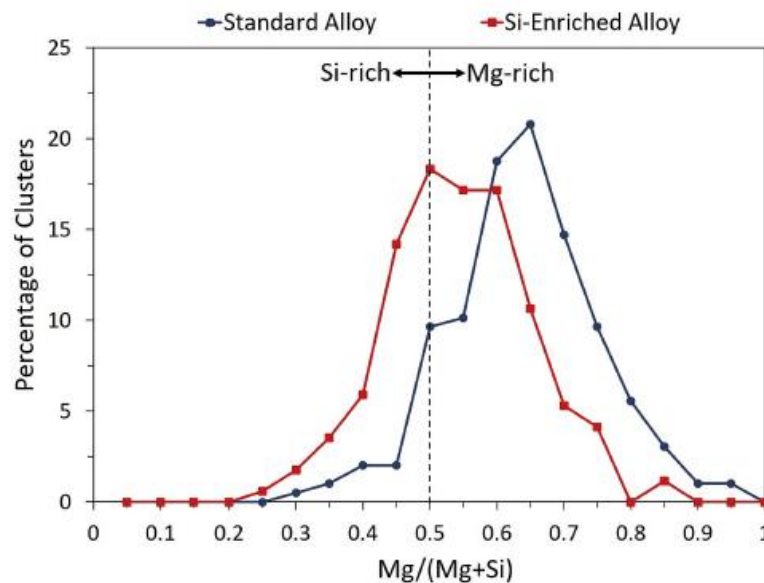


Figure 43 Histogram showing the Mg/(Mg+Si) distribution of the solute clusters in the standard and Si-enriched alloys [70]

Analysis of the needle-shaped precipitates' crystal structures in each alloy was performed using HRTEM and fast Fourier transforms (FFTs). A summary of the phases identified in each alloy is given in Table 5. Figure 44(a)-(d) show representative HRTEM images and FFTs of the needle-shaped precipitates in the standard and Si-enriched alloys respectively (viewed end-on to the needle's length). It should be noted that since the GP-zone/pre- β'' precursor phase and β'' phase share similar needle-shaped morphologies and monoclinic structures [71], the coexistence of these phases cannot be quantitatively determined for either alloy based on the current HRTEM/FFT analysis. The appearance of the precipitate in Fig. 4(b) perhaps shares some resemblance to the pre- β'' phase presented in [71] and, in this case, the unit cell parameters are closer to the pre- β'' precursor phase. However, in other cases, closer agreement with the β'' phase was observed. Previous work on similar Si-rich Al-Mg-Si alloys identified mixed pre- β'' / β'' phase precipitate distributions at the peak-hardness condition [71, 72]. Therefore, these phases are believed to similarly coexist within the Si-enriched alloy. In contrast, the β'' phase reportedly dominates in Mg-rich peak hardness aged alloys [72].

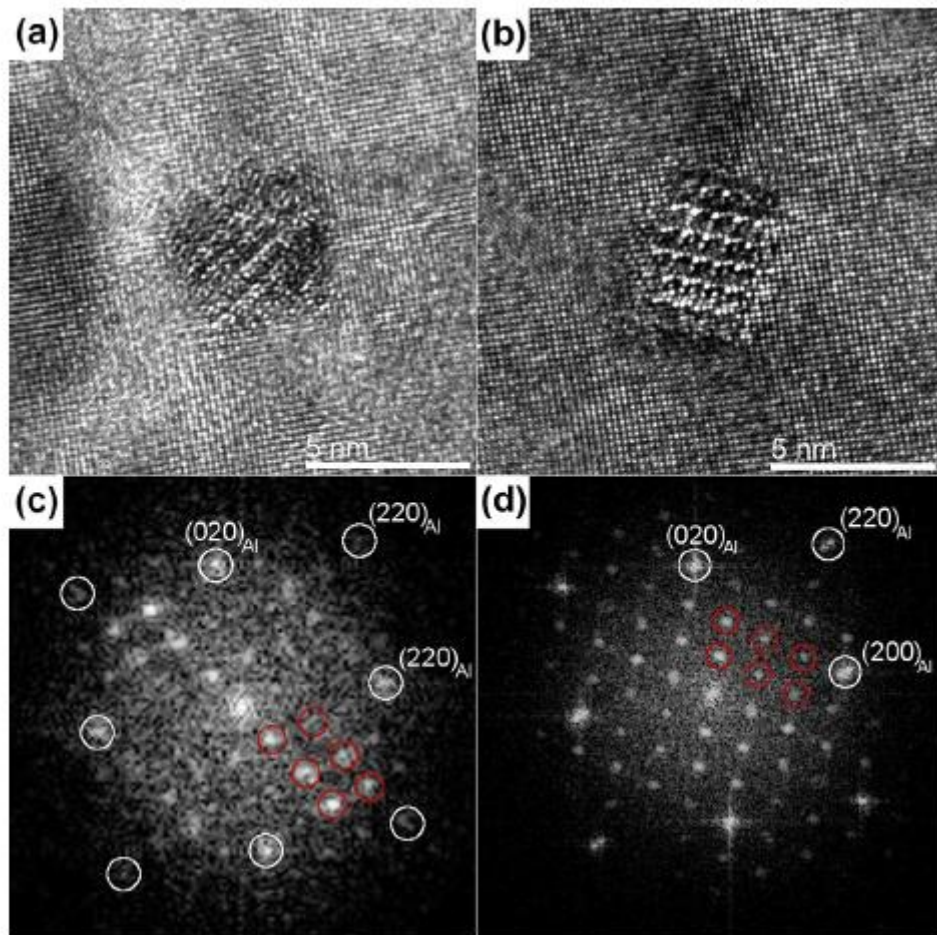


Figure 44 High resolution of TEM images of representative β'' precipitates imaged parallel to their length direction (beam direction parallel to $[001]_{Al}/[010]_{\beta''}$) in the (a) standard 6061-T6 and (b) Si-enriched 6061-T6 alloys. (c) & (d) FFTs for each precipitate, where the red circles indicate reflections from the $[010]_{\beta''}$ zone axis [70].

Table 3 Number of precipitates and their respective phases as identified using HRTEM in the standard and Si-enriched 6061 alloys [70].

	pre- β''/β''	β'	Q'/B'	L	Unidentifiable	Total
Standard Alloy	27	–	–	6	10	43
Si-enriched Alloy	52	5	2	–	5	64

The analyses presented in this study confirmed the coexistence of spherical clusters/GP-zones, needle-shaped precipitates and lath-shape precipitates at the T6 condition. The alloy's overall composition influences the size, number density, chemical composition and crystal structure (in the case of precipitates) of these features.

On average the spheroidal particles, believed to be a mixture of clusters and GP-zones, in both alloys were richer in Mg than Si. However, Si-enrichment of the 6061 alloy caused the Mg:Si ratio of the spheroidal particles to be closer to 1:1. The composition of the largest particles, which are believed to represent GP-zones, converged on the needle-shaped precipitates composition in each alloy.

The average composition of the needle-shaped precipitates in the Si-enriched alloy agrees well with the $Mg_5Al_2Si_4$ stoichiometry (Mg:Si = 1.25). The work presented here determined that the Mg:Si ratio initially increases with increasing precipitate size, which is believed to be caused by the transition between the pre- β'' and β'' phase crystal structures. Cu was unanimously observed within the Si-enriched alloy's precipitates and is believed to similarly substitute at the precipitates Mg+ and/or Si+/Al sites as observed in HAADF-STEM studies.

The high Mg:Si ratios exhibited by the standard alloy's precipitates were found to be caused by a reduction in the precipitate's Si content rather than Mg-enrichment. This observation disagrees with the structural models proposed for high Mg:Si ratio β'' phase precipitates where Mg-enrichment of the phase occurs at the expense of Al. HRTEM analysis of the standard alloy's precipitates revealed features consistent with β'' /disordered needle-shaped precipitates that have been previously observed in Al-Mg-Si(-Cu) alloys, suggesting the high Mg:Si ratio precipitates commonly observed Mg-rich alloys are not solely composed of the β'' phase as reported in previous APT studies. This disorder likely enables the standard alloy's precipitates to contain a lower Si content and higher Cu content than the β'' phase precipitates that are present in the Si-enriched alloy. The cause of the gradual increase of the precipitate's Mg:Si ratio with increasing precipitate size in the standard alloy remains unclear. Though the evolution of this ratio could be similarly linked to a changing Al content within these precipitates or due to preferential growth of the precipitate's disordered region.

Lath-shaped precipitates were also rarely observed within both alloys. Disordered L-phase laths form in the standard alloy, whereas Q' laths form in the Si-enriched alloy. The local distribution Mg and Cu is believed to play a significant role in determining the lath's crystal structure with the Mg-rich solute environment promoting the formation of the disordered L-phase precipitates.

The extensive work of characterization of standard 6061-T6 alloy and Si-enriched alloy have enabled us to better understand the evolving microstructure of the aluminum which gradually gets enriched in Si during irradiation. The precipitation kinetics and each precipitate's interaction with dislocations are influenced by the Mg:Si ratio. Thus the work presented above improves our understanding of the alloy's mechanical properties and our ability to potentially optimize the alloy. In order to maximize the

alloy's Si-induced swelling resistance, an alloy from the 5xxx series could be beneficial since the Mg present in the Al matrix reacts with the transmuted-Si and forms precipitates similar to the β'' phase. However, this alloy is less ductile due to the strengthening induced by these precipitates. For the 6061-T6 alloy, the excess Mg within the matrix potentially has a positive effect on the alloy swelling resistance. The excess Si within the matrix however could cause Si precipitation to occur at lower neutron fluences thus worsening Si-induced swelling.

In addition to these considerations, the second component to swelling is fast neutron-induced void swelling. Thus optimizing the alloy to minimize Si-induced swelling should also take into account this parameter. The following studies, from Garric's PhD work investigate the impact of varying microstructures due to different quenching rates on void swelling.

3.2.3 Impact of quenching rate on microstructure and study of void swelling (V. Garric)

Swelling of metals under irradiation is largely studied in the nuclear industry for its impact on the safe and efficient operation of reactors. However, the case of aluminum alloys remains poorly documented as they are exclusively used in nuclear research reactors which operate at lower temperatures than nuclear power plants. Void swelling in aluminum alloys, which results from the cavities induced by the fast neutron flux in reactor, is measurable only at high fluences, for which few measurement points are available. In this study, samples with various quenching rates were used in order to simulate the variations obtainable during the fabrication of large reactor components.

Using a series of Al-Mg-Si(-Cu) specimens quenched in various fluids, we have monitored the quench carefully and studied the impact of the quenching rate on the microstructure and mechanical properties obtained after aging. Acknowledging the critical quench rate to be about $10\text{ }^{\circ}\text{C s}^{-1}$, quenching was performed in various quenching fluids (water, air and oil) on 10 cm side 6061 alloy cubes. The quench rate was evaluated by thermocouples placed at several locations and by numerical modeling. For each temper, the microstructure and mechanical behavior has been studied at local and macro scales to highlight some correlations. The combination of transmission electron microscopy imaging and related image analysis, chemical and crystallographic mapping, microhardness maps and tensile tests has pointed out many microstructural differences at nanoscale and inhomogeneous mechanical behavior [73]. A summary of some of the microstructural differences observed at various scale by TEM is presented in Figure 45. Results from tensile tests performed on cylindrical section tensile samples extracted from the three quenched cubes are presented in Table 4. Quench rates explored in this study vary from extremely low values (inferior to $0.1\text{ }^{\circ}\text{C s}^{-1}$ for air temper) to values higher than the critical cooling rate (over $30\text{ }^{\circ}\text{C s}^{-1}$ for water temper). Concerning oil temper, as it presented a sufficient density of nanoscaled precipitation and tensile mechanical properties similar to water temper, it is assumed that its cooling rate was near if not over the critical cooling rate of $10\text{ }^{\circ}\text{C s}^{-1}$. According to the literature, mechanical changes are minor above $10\text{ }^{\circ}\text{C s}^{-1}$. The objective of the study was to investigate whether it would be beneficial in terms of swelling to cool above the critical cooling rate. In this study, the water temper sample which presented a gradient of quenching rate above $10\text{ }^{\circ}\text{C s}^{-1}$, showed microstructural differences in the density of nanoscaled precipitation. This observation is partly contradicting the observations from the literature [74]: a quenching rate above $10\text{ }^{\circ}\text{C s}^{-1}$ if not improving the mechanical properties is still modifying the nanoscaled precipitation considering the same artificial aging is applied after quenching. The differences between this study and prior experiments already available in the literature could be attributed to the thickness of the specimens. Concerning the microstructural changes, oil temper and water temper presented differences in dispersoids while both

used to be over $10\text{ }^{\circ}\text{C s}^{-1}$ in terms of quenching rate. Under $10\text{ }^{\circ}\text{C s}^{-1}$, in air temper, the heterogeneity and the composite behavior is emphasized with growing density of dispersoids. It has also been observed that silicon was always present in such particles. Silicon is known to have a low solubility in aluminum. Therefore we propose silicon to be the conditioning element of the precipitation: a slow cooling rate will increase the number of silicon clusters present, which in turn cause a coarser and more heterogeneous precipitation of dispersoids around clusters, leading to less silicon available during the artificial aging and a lower density of nanoscaled precipitates. On the other hand, a higher cooling rate will induce a smaller density of dispersoids and will allow the precipitation of more nanoscaled precipitates during the artificial aging. This would be conditioned by the Mg/Si ratio which is not determined by the chemistry of the material but the available content induced by the quench.

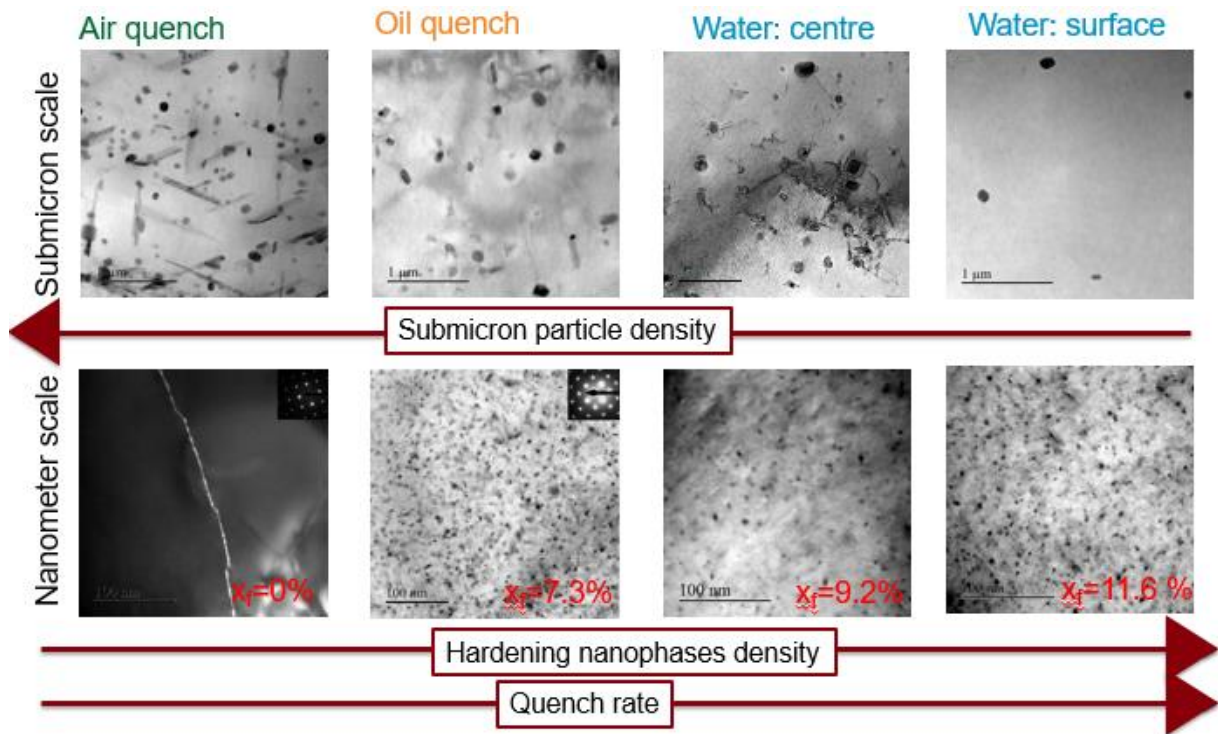
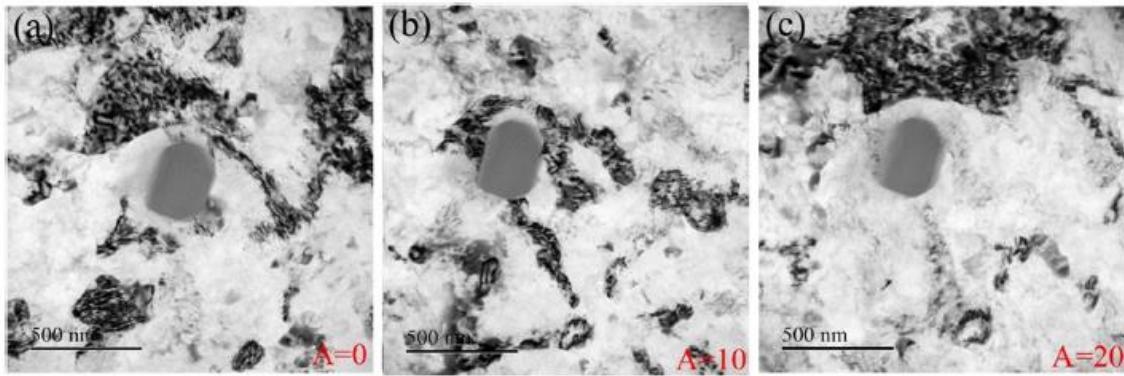


Figure 45 Summary of microstructural evolutions in a 6061 alloy with varying quench rates at various scales (images from [2]).

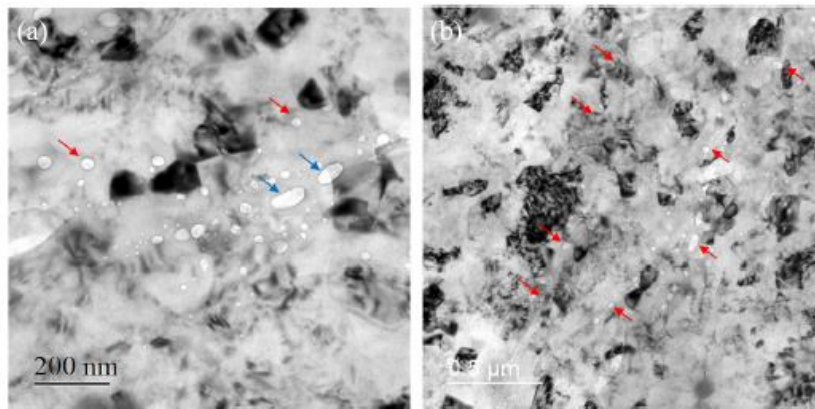
Table 4 Mechanical properties in traction of dogbone samples from the three studied quench rates [73].

	Water	Oil	Air
$Y_{0.2}$ (MPa)	232	230	100
UTS (MPa)	288	275	145
A (%)	13.5	12	11.75

A first series of samples were then irradiated with heavy ions in single beam (Au^{4+}) to understand the impact of the quenched microstructure on void swelling. Samples were investigated at very fine scale and characterized to understand the key mechanisms of swelling. Figure 46 shows examples of the microstructure observed by TEM on water quenched samples irradiated at 100 dpa maximum dose (S-100) and 60 dpa maximum dose (S-60). As can be seen on these figures, for the water-quenched samples, the dispersoids amorphized and some even started to dissolve. The cavities started forming at grain boundaries as well as in the location of dispersoids.



Observed microstructure in a S-100 irradiated water temper sample. Tilting around a submicronic precipitate: (a): $\alpha=0^\circ$, (b): $\alpha=10^\circ$, (c): $\alpha=20^\circ$.



Observation of voids inside the aluminum matrix in a water temper sample in S-60 irradiation conditions. (a): at medium magnification, (b): at low mag

Figure 46 Microstructure of the water quenched sample irradiated in a single beam condition: (first row) Observation of an amorphous precipitate, (second row) Observation of voids (images from [75]).

Observation of some of the nanoscaled particles was performed using APT. For example, Figure 47 shows APT results in a tip-shaped sample at low dpa conditions (15 dpa from masked W irradiation). Due to the highly damaged material, APT could not be performed properly in 60 dpa and 100 dpa single beam conditions because the high density of voids made the tip flash under high voltage. Firstly, clusters of magnesium, copper and silicon are observed. They are seen to be needle shaped which is typical of hardening precipitates. This observation is consistent with the nanoprecipitation observed before irradiation. Very small clusters ($r \sim 1$ nm) are also detected in the analysis. The size of these clusters is equivalent to that of GP zones which are the precursors of β'' precipitation sequence. Clusters of zinc coinciding with Al-Mg-Si-Cu clusters are observed. Before irradiation, zinc is in solid solution and is not measured inside Al-Mg-Si-Cu clusters. The presence of Zn in the Al-Mg-Si-Cu clusters is consistent with the aggregation of zinc toward nanoprecipitates under irradiation. Results from the cluster analysis performed on this tip showed that zinc migrates from a homogeneous solid solution distribution in unirradiated material to co-clustering with existing precipitates under irradiation.

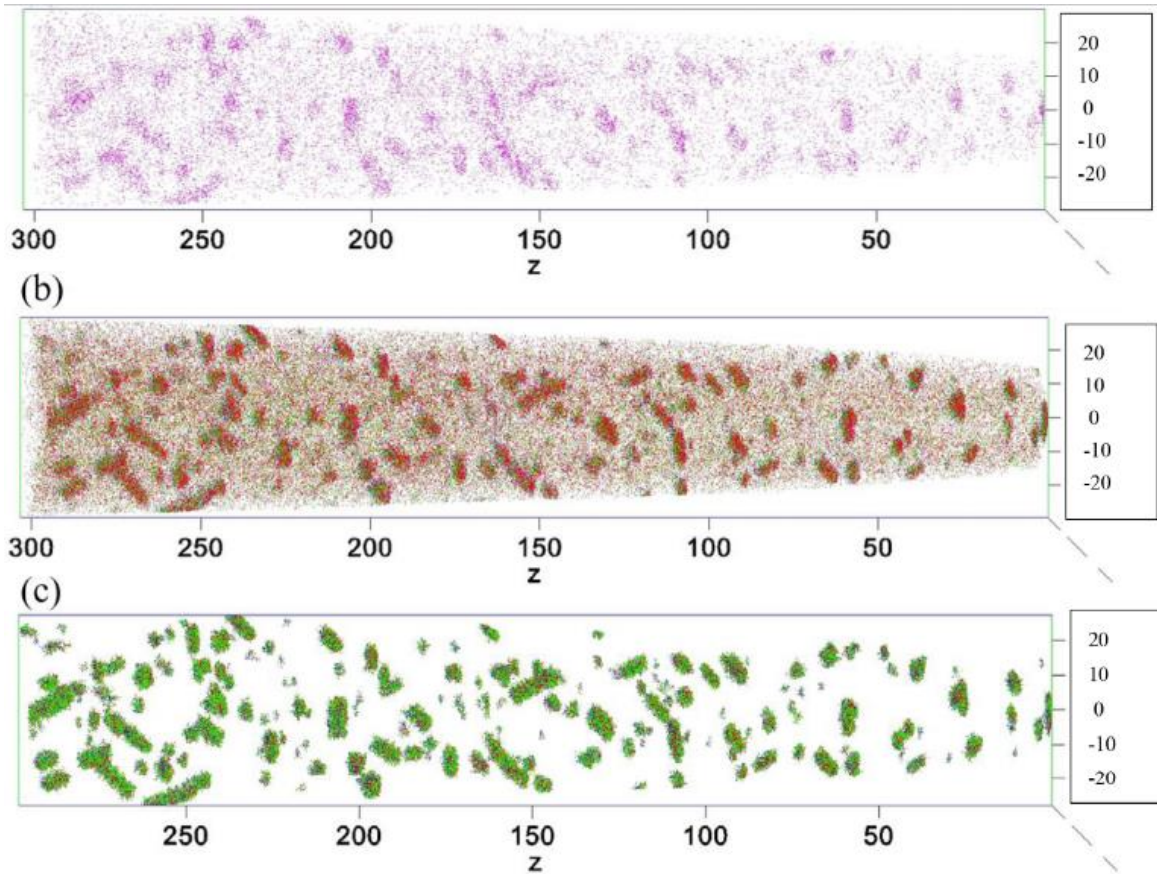


Figure 47 APT experiments in single beam water quenched samples after single beam irradiation under W with varying dpa doses (from 3 to 15 dpa depending on the location on the sample due to ‘masked irradiation’). Display of (a) Zn atoms, (b) Zn, Mg, Si and Cu atoms, (c): result of Zn, Mg, Si, Cu clustering analysis [75].

Figure 48 is a schematized diagram explaining the formation of voids during single beam irradiations in 6000 aluminum alloys as observed in this Garric’s PhD work. Three main microstructures are pictured before and after irradiation. They are described not by the quench fluid but by their quench rate, which is compared with v_{crit} , the critical cooling rate according to the literature. v_{crit} is known to be equal to $10 \text{ } ^\circ\text{C}\cdot\text{s}^{-1}$.

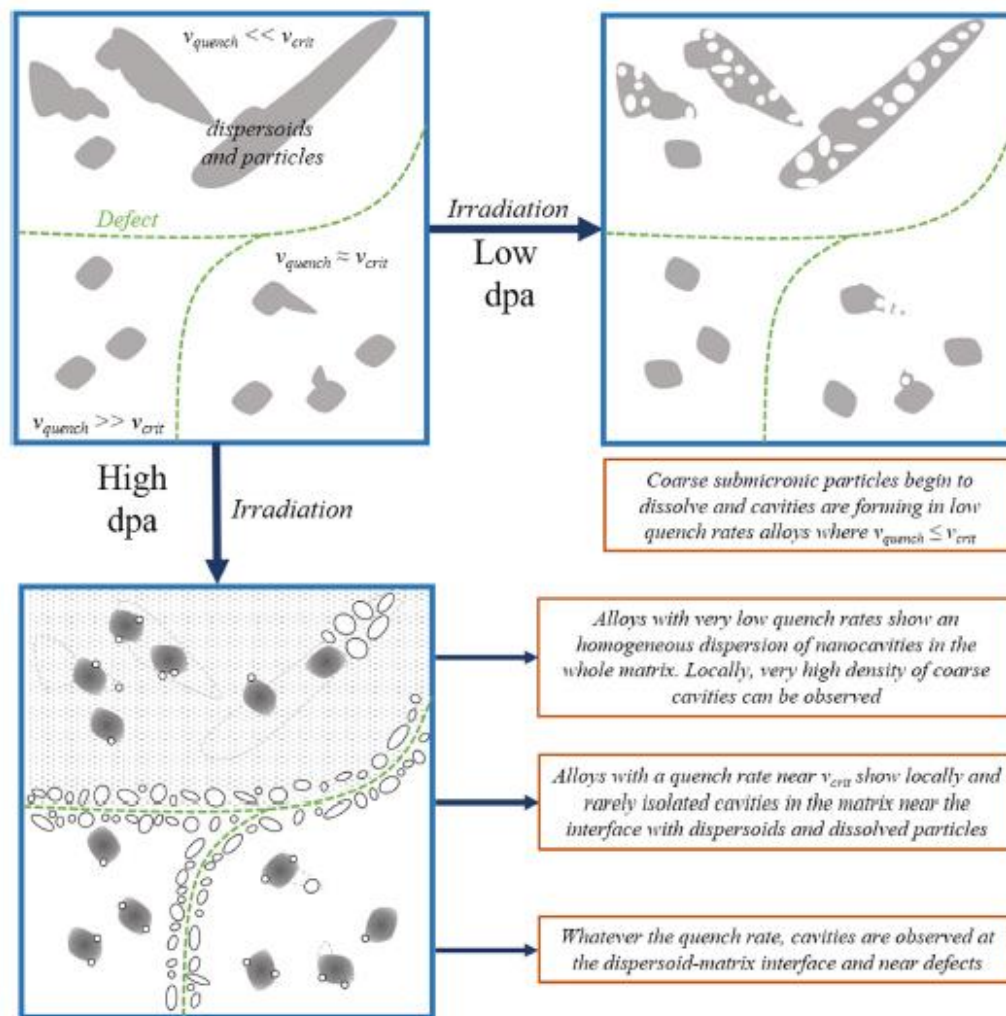


Figure 48 A schematic diagram on the formation of voids in aluminum alloys depending on the initial microstructure. V_{crit} is the critical quenching rate according to the literature $10\text{ }^{\circ}\text{C s}^{-1}$ [75]

A second series of samples were irradiated in a triple beam (W^{9+} , He^{+} and Si^{+}) to simulate the aluminum transmutation occurring inside reactors. The microstructure modifications after triple beam irradiations are notably different from those observed after single beam irradiation. Nano-bubbles are observed in the whole matrix for all tempers as seen for example in water temper samples in Figure 49(a). The EELS analysis, Figure 49(a), reveals helium inside the voids and a statistical analysis shows the bubbles size is directly linked to the amount of helium injected. In the vicinity of the dispersoids present in the matrix, bubbles tend to be rare and coarse as seen in Figure 50. By comparison, after single beam irradiations, voids are not observed to be homogeneously distributed and preferential nucleation sites have been evidenced as reported by Farrell [76] who demonstrated that the helium production under neutron flux leads to an homogeneous dispersion of bubbles in the whole matrix. This was also observed in this study under ion beam. The overall density of nanoprecipitates tends to decrease under irradiation while new ones form. This observation is likely to be linked to silicon implantation. According to Weeks et al. [68], the formation of silicon during neutron irradiation leads to the formation of silicon nano-precipitates. For the study of void swelling, the initial microstructure differences at the submicronic scale is not a key parameter since after helium implantation bubbles nucleate homogeneously in the matrix. Therefore, helium implantation tends to homogenize the formation of voids whatever the

quenching rate. This seems to be beneficial for low quench rate where coarse voids are no longer observed in the place of previously present particles. But for high quench rates, it seems to produce numerous bubbles and homogeneously dispersed voids in the matrix which were not observed after single beam irradiations.

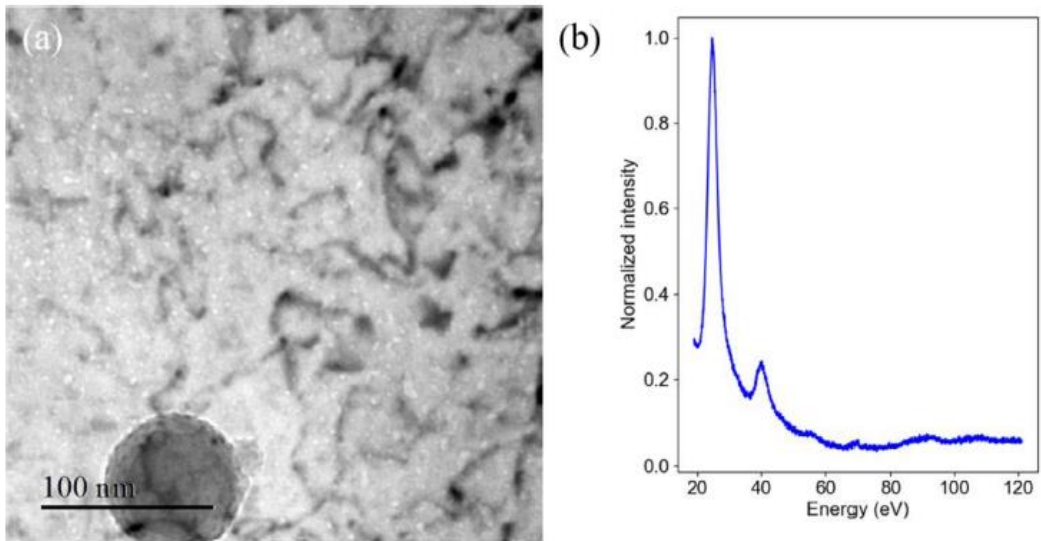


Figure 49 (a) Area with nanoscale cavities inside watered tempered specimen in triple beam conditions, (b) EELS analysis in area containing bubbles [75].

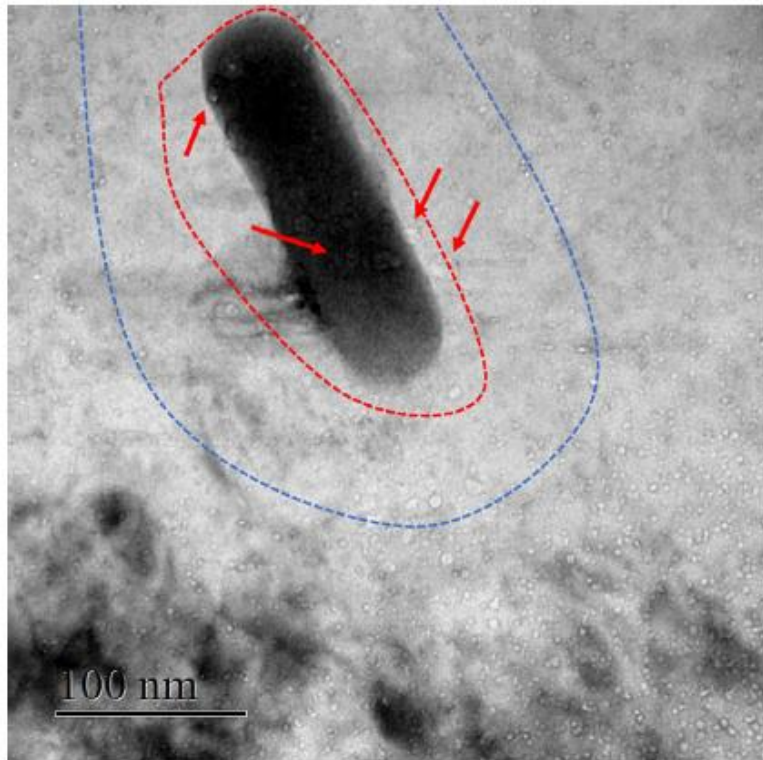


Figure 50 Dispersoid observed in oil temper on a triple beam irradiated sample [75].

Figure 51 represents schematically the same initial state as provided in Figure 48, but adding a representation of the nanometric scale. The influence of the implantation of silicon and helium during irradiation is represented and the microstructure modification is pictured at both scales. The behavior of 6000 aluminum alloys under irradiation is different for various quench rates and the irradiation conditions. Nanoprecipitation remains stable under irradiation whatever the quench rate, except when silicon and helium are implanted. Under triple beam conditions, another kind of nanoprecipitation appears. Dispersoids amorphized under ion flux whatever the temper and the irradiation conditions. However, coarse particles (oxides) and heterogeneous precipitates seen in oil and air tempers totally dissolved in the early stages of irradiation. Different nucleation sites have been identified for voids and bubbles. In all tempers, in single beam conditions, voids aligned suggesting a nucleation on dislocations or grain boundaries and also formed at the dispersoid-matrix interfaces. In air temper in single beam conditions, nanometric voids were observed in the whole matrix and local heavy concentration of irregular voids was rarely observed. With triple beam conditions, nanometric voids were observed in the entire matrix for all tempers. The results from this work globally show a strong link between tempering conditions and behavior under irradiation. In addition, specific irradiation conditions (single beam or triple beam with helium and silicon implantation) will also strongly impact the response of the material. In particular helium implantation seems to have a strong impact on the bubble density, and because of the very high helium concentration implanted in our triple beam study, the void swelling has been measured after simple beam irradiations. In order to quantify the total swelling under neutron flux, modeling has been performed as discussed briefly below.

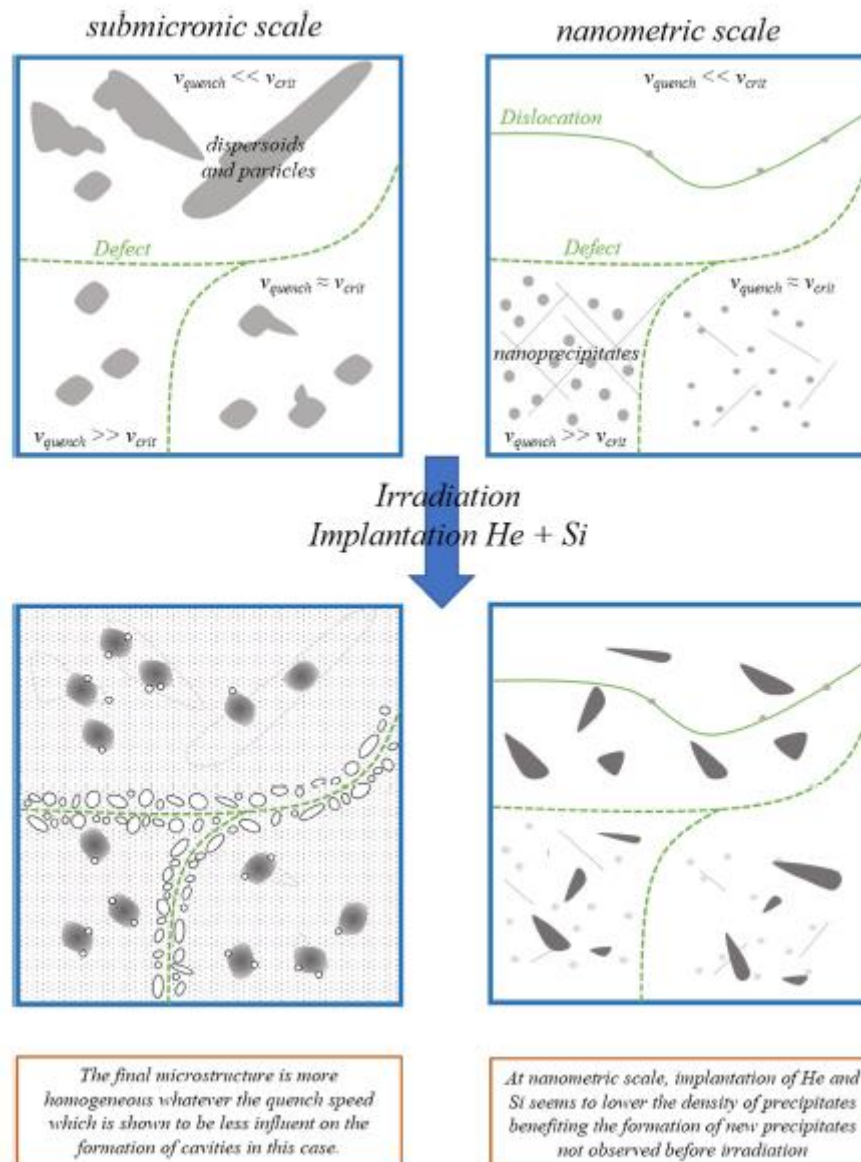


Figure 51 Schematic representation of the influence of silicon and helium in the formation of voids under irradiation [75].

Quantitative measurements of the swelling were performed in each sample studied. A high dispersion of the swelling values and a higher value are observed after ion irradiation compared to neutron irradiation for a similar irradiation dose, which seems to be related to the very high damage rate created by ion-irradiation in a very short time. Considering TEM roughly displays a 100 nm thickness and DPA rate being around 5 dpa.nm⁻¹ for the first 200 nm under single beam, a large range of damage rate was observed. Therefore, it appears relevant to complement the description of swelling in aluminum alloys with a modeling approach. Swelling values from the literature were incorporated into a Brailsford & Bullough swelling model for two different damage rates, after estimating the parameters of the model from the literature. This work aims at a better comprehension of the swelling of aluminum alloys both from a quantitative and qualitative point of view and draws the basics requirements for future swelling models.

Figure 52 is a plot of all data on 6061-T6 retrieved from Farrell after neutron irradiations [77] and from experiments after ion irradiations presented in Garric's work [75]. A high inhomogeneity is observed for our study using ion irradiation, and a decrease of swelling values with increasing dpa. According to Figure 52, the swelling values measured after neutron irradiations also present a high dispersion with three high values, two low values close to the silicon swelling line and one value at low dpa possibly fitting two different lines. This dispersion can be related to the different neutron spectra (r ratio) seen by the samples: at a given dpa, the contributions of the silicon swelling and of the void swelling can vary in a large range. Indeed, the silicon swelling is dependent on the r ratio, and the void swelling on the fast flux level, i.e. the damage rate. That is why, two simulations were performed, using two different damage rates: one fitting the high swelling values measured after neutron irradiations and the other adapted to the low swelling values. Figure 53 pictures the swelling at the maximal damage flux of 1.10^{-6} dpa.s⁻¹. Concerning the temperatures themselves, 90 °C is representative of a high temperature reached in a nuclear research reactor core. Final results presented this figure show an increase of the swelling with the damage level and a swelling peak around 110 °C. For 10 years inside reactors under high fast neutron flux, the range of results (1.7% to 3%) seems reasonable. The larger swelling values measured after ion irradiation in our study can be attributed to the higher damage rates obtained with ions. The difference in terms of damage rates (1.10^{-6} dpa.s⁻¹ for the highest neutron fluxes to 1.10^{-4} dpa.s⁻¹ on average for ions) modifies the swelling kinetics itself. Increasing the damage rate reduces the probability of recombining interstitials and vacancies and therefore increases the swelling. Furthermore, in nuclear reactors, transition periods, stops, reboots, thermal fluxes and neutron flux variations modify and globally lower the swelling compared to ion irradiations performed in one batch. In addition, the chosen high flux and fluence in our ion irradiations lead to a wide damage range (150-400 dpa) in a short thickness (1 μm) which introduces an uncertainty in the determination of a swelling associated to a damage level. Finally, it has been demonstrated earlier in this work that the metallurgical state is conditioning the voids sizes and distribution.

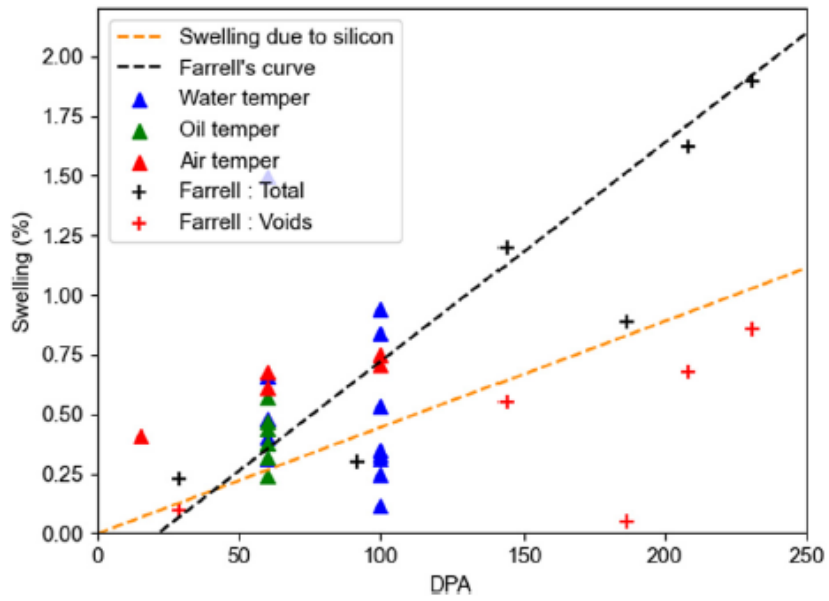


Figure 52 A global overview of swelling values. Crosses are values from Farrell experiments (neutrons)[77]. Triangles are values from Garric's work (Au^+ ions) [75] with the color indicating the quench.

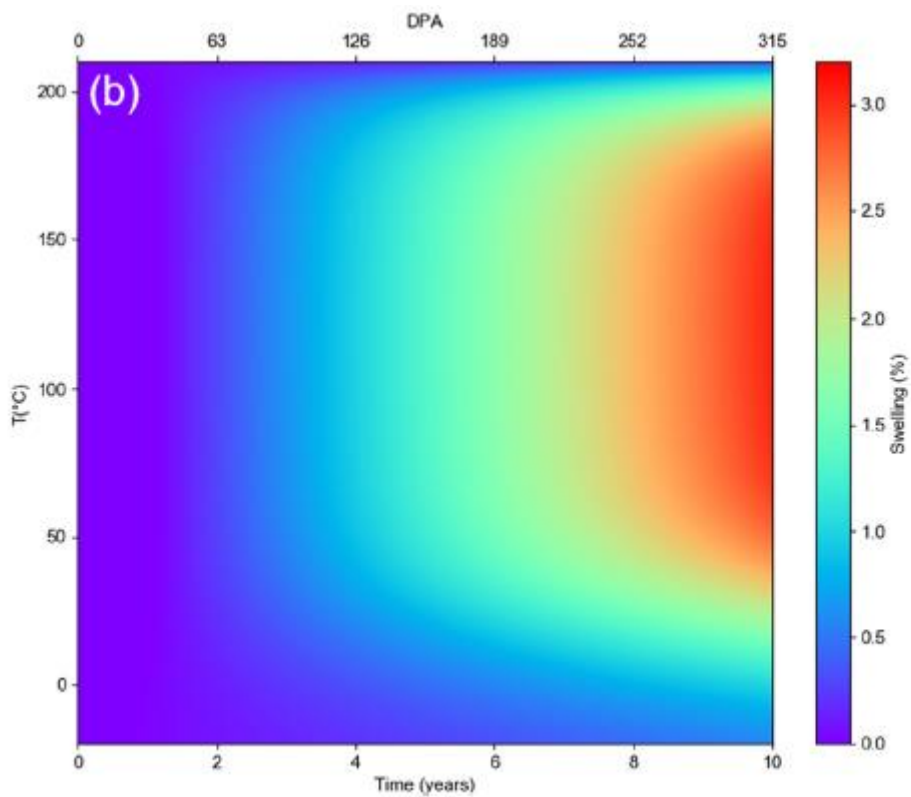


Figure 53 Modelling of the total swelling (silicon + voids) of a 6061-T6 alloy under neutron irradiation during 10 years at $1.10^{-6} \text{ dpa.s}^{-1}$ ($\sim 6.9.10^{14} \text{ n.cm}^{-2}.\text{s}^{-1}$, $E > 0.1 \text{ MeV}$) with a thermal to fast neutron ration of 1/3 [75].

3.2.4 Understanding the fracture toughness evolution with aging duration and irradiation (T. Petit)

The work performed by Petit during his PhD aimed at understanding the link between microstructure evolutions during aging, strength evolutions and associated toughness changes in order to be able to optimize microstructures by modelling and to predict mechanical properties' evolution. In a previous study by Petit et al. [78], a decrease in toughness was observed with aging time in a 6061 aluminum alloy after aging at 175°C during 4, 8, 12 or 16 h. Aging causes hardening and a toughness drop (Figure 54). During toughness tests, the drop in load after the maximum load depends on the material crack growth toughness (which is quantified by the tearing modulus calculation): the faster the load decreases, the faster the crack propagates. The decrease in toughness with aging time is therefore clearly identifiable in Figure 54. It is fundamental to understand whether this decrease results from a change in the coarse particles (responsible for the damage), or in the fracture mechanisms, or whether it is solely due to the hardening of the matrix observed in tensile tests.

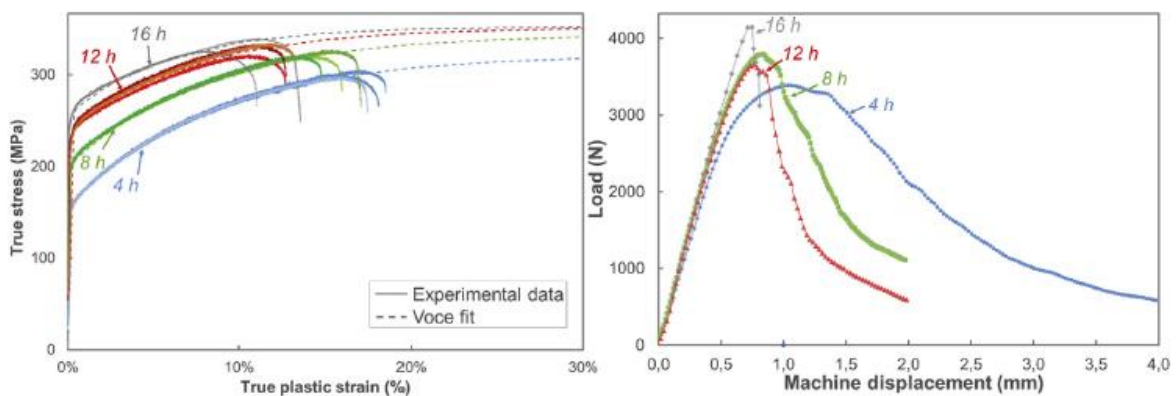


Figure 54 Experimental tensile curves (and fitted curves) on the left, CT-toughness test curves (load as a function of machine displacement) on the right for the four aging times studied (4, 8, 12 or 16h) [78].

The work presented in this section and published in [79] thus was separated into several steps:

- Studying the undamaged material and the effect of aging on the microstructure, using various characterization methods such as Scanning Electron Microscopy (SEM) for coarse particle analysis, electron Backscatter Diffraction (EBSD) for grain distribution investigation, and Atom Probe Tomography (APT) for hardening nanoprecipitation evolution study.
- Identifying fracture mechanisms as a function of aging state using fractography, laminography and EBSD of samples containing interrupted cracks, in order to identify transgranular and intergranular fracture.
- Simulating of decrease in toughness based on the identified damage mechanisms using a stress-based nucleation model.

During this work, I participated in designing, conducting and interpreting the experiments in SEM, APT and synchrotron laminography performed at ESRF. The use of this correlative multiscale approach by combining scanning electron microscopy, atom probe tomography as well as 3D X-ray laminography showed that coarse particles and the characteristic damage mechanisms do not depend on aging time: the fracture mechanism is typically ductile and transgranular as shown by electron backscatter diffraction analysis of sections of compact tension specimens containing interrupted cracks such as presented in Figure 55. Large Mg_2Si inclusions fracture at very low plastic strain, and defects nucleate at large (Fe,Si)-rich inclusions with increasing plastic deformation.

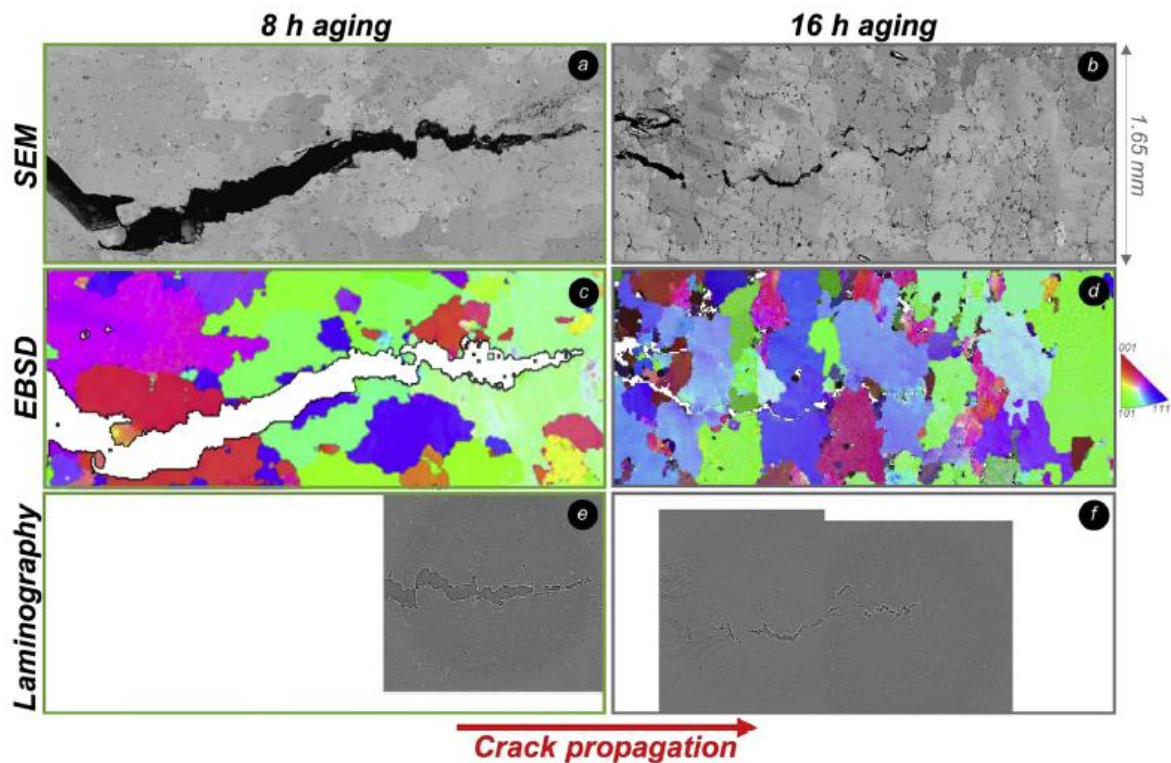


Figure 55 Correlative investigations using SEM (a/b), EBSD (c/d) and synchrotron laminography (e/f) of two slices of CT specimens after interrupted toughness tests (8h aging for a/c/e and 16h aging for b/d/f) [79]

Only the hardening nanoprecipitation increases with aging time: aging favors the precipitation of nm-size Mg_2Si precipitates as illustrated in Figure 56 which causes hardening of the matrix so that damage nucleation at coarse inclusions becomes easier - thus leading to a decrease in toughness. Indeed, larger clusters and a substantially higher area fraction of iron based intermetallic particles are found on the fracture surfaces of the longest aging time CT samples compared to the shortest aging time samples.

Based on these observations, a Gurson-Tvergaard Needleman type model was developed to simulate the tearing tests using Finite Elements. It used damage nucleation kinetics which depend on the maximum principal stress, since a classical strain-based nucleation is not sufficient to reproduce the deterioration of the tearing modulus. The model is not detailed in this manuscript for the sake of brevity and because my participation in its development was minor but results can be found in [79, 80].

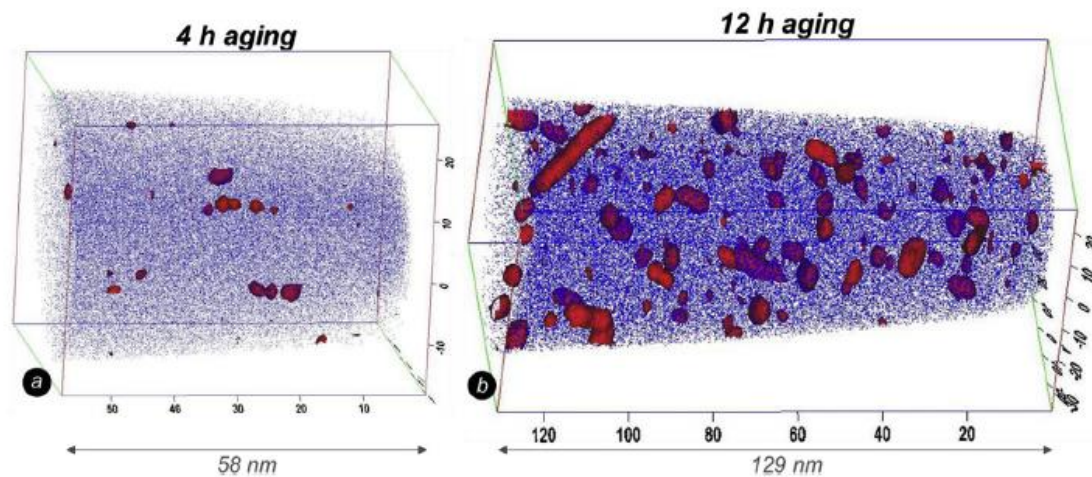


Figure 56 Comparison of two APT tips after 4h (2.1 million ions analyzed) and 12h aging (8 million). The red isosurfaces represent areas of high concentration of Mg (>3%) in the aluminum matrix represented in blue [79].

3.2.5 Conclusions on the impact of thermo-mechanical treatment and irradiation on the microstructure and mechanical properties of the 6061-T6 alloy

The study of the evolution of the 6061-T6 microstructure in reactor involved the use of various complex characterization techniques in order to observe the relevant phenomena which could have a strong impact on the dimensional evolution or mechanical properties changes during life in reactor. Since the processing route to obtain a 6061-T6 alloy is complex, the study of varying parameters such as aging time, quench rate, on unirradiated alloys also had to be conducted prior to studying the effect of irradiation.

The β'' nanoprecipitates were studied extensively using TEM and APT during Flament's PhD work and Buchanan's post-doctoral studies. These hardening precipitates play an important role in optimizing the mechanical properties of the alloy and it was important to understand their evolution under irradiation (ion-irradiation in our case) as well as with Si-enrichment of the matrix due to the transmutation of the Al atoms.

This transmutation also leads to swelling under irradiation. Another factor responsible for irradiation swelling of aluminum alloys is void swelling. This was one of the subjects tackled by Garric during his PhD work. Firstly, he studied the impact of varying quench rates on the microstructure of the 6061 alloy. Indeed, when fabricating large components for reactor cores, the quench rate may vary within the component which would lead to a nanostructure and microstructure evolution through the thickness of the component as seen from his work. These samples were then irradiated using single beam and triple beam ion irradiation in order to study void swelling in the material. Detailed TEM analyses were performed as well as APT when possible in order to characterize and quantify swelling in the material. Based on these observations, a swelling model including both Si-induced swelling and void swelling was developed and used as a basis for the prediction of swelling under irradiation in RRs.

Finally the work of Petit during his PhD focused on the mechanical properties evolution depending on the duration of the aging step of the T6 treatment. An array of characterization techniques was used in order to observe differences in microstructure with increasing aging time (SEM, APT and EBSD). Characterization of the fracture mechanisms at play was also performed using fractography, synchrotron laminography and EBSD. Finally, based on the observation made a stress-based nucleation model was developed and simulated in a satisfactory manner the fracture toughness tests performed on samples with various aging durations.

3.3 Conclusions on studies on aluminum alloys

Aluminum alloys used for RRs were subject of many studies conducted at CEA since it has a history of designing and operating such reactors. In particular, the construction of the JHR reactor at the CEA Cadarache site has fueled many research studies on the behavior of various aluminum alloys in order to optimize the design of the reactor. Several PhDs and post-doctoral fellows, supervised by CEA personnel, have, over a period of 10-15 years, developed a detailed understanding of the behavior of the 6061-T6 aluminum alloy, chosen for the core components of the JHR and of the AlFeNi alloy, chosen for the fuel plates of the reactor.

When studying corrosion, firstly parameters impacting corrosion kinetics were studied in order to better predict the thickness of the corrosion layer on the core components of the reactor. In particular, temperature and pH were found to be two important parameters that can have a strong impact on the corrosion layer that would form in reactor on core internals. Additionally, irradiation was found to increase significantly corrosion kinetics for both AlFeNi and 6061-T6 alloy. Comparison between ion-irradiated samples and neutron irradiated samples that were irradiated in the Osiris reactor have shown that some similarities can be observed between the two types of irradiation such as an increase in corrosion kinetics. Some effects, however were harder to reproduce.

Future studies on corrosion will have to add another parameter: flow rate. Indeed, in the JHR, the flow of water circulating through the reactor core at 15-20 m/s could induce erosion and faster thinning of the aluminum components. Combining irradiation, general corrosion parameters and flow rate into a model would then be the next step in order to have a good capability to predict the corrosion of the core components over several years, or even decades of use.

The thermo-mechanical processing route leading to the 6061-T6 route has also been a subject of many studies, in particular in order to optimize mechanical properties and behavior under irradiation of aluminum components. Studies involving nano-characterization techniques such as TEM and APT have focused on the hardening precipitation and its evolution under irradiation (ion irradiation in the cases presented here), under aging evolution and Si enrichment due to aluminum transmutation. Studies on the swelling due to Si enrichment and void creation under irradiation have also been conducted on samples that has varying microstructures and nanostructure due to undergoing different quench rates during their processing route.

This was done in order to be representative of quench rate variations in thick component in 6061 such as can be found in the nuclear industry. Using TEM characterization of ion-irradiated samples, swelling data was gathered and the basis for a swelling model was proposed in order to anticipate the potential swelling behavior of aluminum components in the reactor core.

Finally, in order to understand an unusual mechanical behavior observed in aluminum alloys: pop-ins during CT tests, a large array of characterization techniques was used in an investigative approach to pin-point which parameters were responsible for this mechanical behavior. It was found that variations at the nanometer scale such as can be created with various aging durations during the T6 process could be responsible for variations in the fracture mechanics of the material. Based on these characterizations, a stress-based nucleation model was proposed and found to simulate well the evolution of the fracture toughness of the material with aging duration.

Future studies would have to include fine characterization of neutron irradiated samples using TEM and APT in order to compare the observations made on ion irradiated samples to the more complex situation encountered in reactor. Additional data is also needed in order to strengthen the swelling model and determine some of its parameters with the proper certainty.

Finally, similarly to what had been done at the end of section 2, a summary of the characterization techniques used in the studies presented in this section 3 are presented in Table 5. This table illustrate the wide range of techniques used, often in a complementary fashion during a same study.

Table 5 Summary of techniques used for aluminum alloys characterization.

Name of the technique	Information gathered from this technique	Approximate dimensions of analyzed area	Application to aluminum alloy characterization
SEM	Microstructure Fracture mechanisms	Lateral resolution in the order of tens of nm	Oxide structure and thickness, hydride microstructure observation
EDS	Chemical information	Probed depth $\sim 1 \mu\text{m}^3$	Precipitate characterization
EBSD	Crystallography	Probed depth $\sim 100 \text{ nm}$	Grain boundary characterization, intra- inter-granular hydrides
FIB	Sample preparation and tomography	Dimensions of samples prepared $0.5 \times 5 \times 10 \mu\text{m}^3$ Analyzed volume \sim tens of microns	Samples prepared at specific locations (metal-oxide interface, implantation peak), APT sample preparation
TEM	Microstructure	Lateral resolution in the order of 0.2 nm (conventional TEM)	Characterization of irradiation damage, crystallographic structure of precipitates, hydrides and other phases
EDX/EDS	Chemical information	Lateral resolution in the order of tens of nm	Chemical identification of precipitates and other phases
TEM - EELS	Chemical information, thickness and coordinance	Lateral resolution comprised between 2 and 0.1 nm (depending on the TEM used)	Thickness information of TEM samples for calculation of dislocation density
HRTEM	Crystallography and atomic structure	Resolution for aberration corrected TEM : 0.05 nm	Phase identification
APT	Chemical information and nanostructure	Lateral resolution in the order of 0.1 nm, depth resolution in the order of the nm Analyzed volume : a few hundreds of nm^3	Observation of smallest precipitates and clusters, diffusion of elements in sample
Synchrotron laminography	3D imaging	Area probed : between a few microns to a few mm	Voids and fracture path in interrupted CT tests
Grazing incident XRD	Crystal structure	Area probed : micron-scale	Oxide phase identification
Raman spectroscopy	Oxide phases	Spatial resolution $\sim 1 \mu\text{m}$	Oxide phase identification

4 Conclusions and Perspectives

General conclusions

The work presented in this manuscript encompasses various metallic alloys used in the nuclear industry and issues they can encounter in reactor. I have focused my work on only a small selection of those issues linked to the environmental degradation of materials in reactor. For zirconium alloys, the main focus of my studies conducted in the USA and at CEA was corrosion and hydriding. Using a large array of characterization techniques, the corrosion of several zirconium alloys used as fuel claddings was studied and parameters incorporated in kinetic corrosion models were determined for unirradiated and irradiated material.

In many of the studies presented in this work, the impact of irradiation was investigated using ion-irradiation. This method presents many advantages such as avoiding activation of the material, being able to choose the irradiating particles and their energy and thus conduct separate effects studies in order to compare the impact of different parameters on the phenomenon of interest. Conducting such experiments requires the use of large user facilities such as Jannus for example which provide access through a proposal-based system. The disadvantage of ion-irradiation experiments is that the damage rate is usually much more important than that observed in reactor. In addition, the actual consequences of in-reactor operation are much more complex than those simulated by ion-irradiation. The irradiating particles are numerous and impact the chemistry and microstructure of the material in very complex ways. Thus, in my opinion, it is essential to combine ion-irradiation studies with neutron irradiated material.

This has been a possibility for some of the work presented in this manuscript because I worked at the CEA Saclay Hotlab which allowed me to have access to facilities able to handle radioactive material. Such studies include the hydride reorientation work performed on cladding irradiated in French and American PWRs and Swiss BWRs. The information extracted from these materials (mechanical properties, hydride microstructure) give data directly usable by the nuclear industry to predict the behavior of similar material in current reactors or already in spent fuel pools or dry storage casks.

Some work on aluminum alloys also tried to understand phenomena observed in radioactive materials, such as an increase of corrosion rate or pop-ins occurring during compact-tension specimens by using unirradiated materials as well as ion-irradiated materials and submitting these materials to detailed characterization. In this case as well, the use of user facilities such as synchrotrons to perform laminography for example were key to the understanding of the fracture mechanics of the studied aluminum.

The work performed on aluminum alloys also required characterization at very small scale since even the smallest particles can impact the mechanical behavior of large components. In these cases, working closely with expert microscopists at CEA and in French Universities, has allowed us to perform various types of observations on our materials. In my case, my expertise in APT has also been used for these studies and it was clear that the complementarity between APT and TEM is key to study nanometer size clusters and chemical variations at very small scale.

In conclusion, I hope that the work presented in this manuscript, which represents approximately 10 years of research as a nuclear materials scientist at CEA, and at Penn State University before, that has shown that no work on such complex phenomena can be performed by one person or with one single technique. It is the combination of various characterization methods, accompanied by expert points of views in different domains, that allows the development of predictive capacities in order to understand material behavior in reactor as well as to develop new alloys for current or future nuclear reactors.

Perspectives and future research projects

Following on the work performed in the NFIR project on reoriented hydride as well as my PhD work, new studies were launched which involved the use of high energy synchrotron diffraction in order to study the impact of pre-existing hydrides on the precipitation kinetics of zirconium hydrides. Additionally, in order to understand the physical phenomena responsible for the variation in zirconium, in-situ TEM studies are also underway to observe the so-called memory effect that induces precipitation of hydrides in their pre-existing dislocation nest, thus lowering the energy needed for their nucleation.

In general, there is an increase of experiments designed to characterize materials in-situ, or in-operando. Indeed, it has been observed that characterizing materials after the fact (out of reactor, out of autoclave, after irradiation, at room temperature) can lead to incorrect interpretations of what has actually happened during the experiment, or what would actually happen in reactor. During my PhD studies, I have reproduced heating and cooling of samples and continuously acquired diffraction data during the thermal cycles in order to study in-situ hydride dissolution and precipitation kinetics. However, these in-situ experiments are difficult to conduct on neutron irradiated materials. I believe that we will see an increase of such experiments however in radioactive materials in the next decade, as instruments get more precise and we can work with smaller sized samples (thus less radioactive than larger samples). Corrosion experiments using in-situ measurement such as pH, impedance spectroscopy, conductivity evolution are also underway at CEA and in Universities. These experiments are key to understand the diffusion of elements through the oxide layer and to formulate a proper corrosion model. Studies underway at several universities are also including specific cells to APTs for examples in order to study hydriding while the APT analysis is underway. Such instrumental developments could also increase the information gathered and help better understand the physical process occurring when samples are hydrides, corroded, etc.

Concerning aluminum corrosion, work is also continuing at CEA, adding the effect of erosion reproducing the fast flow rate that will occur in the JHR reactor. After l'Haridon-Quaireau's PhD a new corrosion loop was linked to the autoclaves used for her studies in order to investigate the effect of the water being treated, cleaned instead of a media being progressively charge in particles due to aluminum oxide corrosion. The flow rate investigations require more experimental design in order to have the proper set-up to corrode the samples while controlling temperature and pH.

During the studies on corrosion, I had been involved with an analytical chemistry laboratory, the LASE (Laboratoire d'Analyse en Soutien aux Exploitants, Analytical Support to Facilities Laboratory) which characterized chemically the autoclave media of samples after corrosion runs, including radioactive water from the autoclave inside the hotcell at CEA hotlab, as well as determining the composition of small samples in particular aluminum alloys after neutron irradiation, in order to measure the Si content for example. I am currently the head of the LASE since the end of 2020 and this has allowed me to develop a better understanding of the chemical characterization of samples, solid and liquid. In this laboratory, several techniques, new to me, are commonly used to measure the elemental composition, the radioactivity and the anion and cation composition of nuclear waste and of samples coming for dismantling operations. The techniques used range from Inductively Coupled Spectroscopy (ICP-AES and ICP-MS) to Chromatography of different types (Ion, Liquid, High Precision) as well as nuclear measurement methods such as gamma, alpha or X spectroscopy, autoradiography, liquid scintillation and also radiochemistry. Using these techniques and combining those with microscopy, large user facilities or other material characterization techniques, the entirety of a system could be characterized and understood.

Future development that are underway is the increase of combined work between material scientists and modeling teams. In the work presented in this manuscript, some models were presented, for example corrosion models for zirconium alloys, swelling models for aluminum alloys and fracture mechanics simulations for aluminum alloys. However, since these models are developed after many years of characterizations, and in the case of many PhD students, at the end of their PhD work, they lack the complexity of models developed by specialized teams. Indeed, such complex models can often be multi-scaled and spread out of various time frames. For the follow up of Garric's PhD, a more detailed model, based on additional separate effect ion-irradiation experiments is currently underway in order to have a more predictive model of swelling in aluminum alloys. I was lucky to work with modelers on the phase-field modeling of zirconium hydrides during my PhD studies and after as well, and this collaboration has led to several interesting publications where TEM, SEM and phase-field modeling are linked to gather a better understanding of the hydride microstructure that forms within a zirconium matrix. An area of application of computer science combined with material science is the use of Artificial Intelligence (AI) in order to treat large data sets such as can be recorded during synchrotron experiments, or in MTRs. This correlation is already underway in some case where neural networks are used to find links between mechanical test results and the actual mechanisms that are in play. I believe that these developments will increase in the next decade and will bring breakthroughs in understanding large data sets.

In terms of experimental developments, the APT I used at the CEA has recently been used to study neutron irradiated materials. Modifying the instrument in order to study highly active samples has been a long undertaking spanned over several years and the recent achievement on neutron irradiated zirconium alloys has been a great step for the CEA Hotlab. Several studies and radioactive samples are now lined up in order to be analyzed with APT and compared with previous results gathered on ion-irradiated samples or on unirradiated samples. Additional development on APTs currently under study by APT manufacturers in collaboration with research teams include an APT coupled with a TEM which would lead to coupled analyses

on a same sample. Indeed, in recent years, we have seen an increase of a single sample being multi-characterized. This difficult experiment presents the advantage of a perfect correlation between various characterization techniques and thus elimination of the potential artifacts that each technique could present. Having instruments linked together could thus be a great advantage for these characterization steps.

Finally some areas of research in the nuclear industry in terms of materials science include accident-tolerant fuel which could withstand the harsh conditions occurring during a loss of coolant accident or a reactivity initiated accident for longer durations and with smaller consequences. Coated zirconium alloys are a solution already developed since several years by the nuclear industry and has yet to be fully put in service. Doped fuel pellets are also some of the components that could be used for accident tolerant fuels. Development of new alloys or more efficient water circulations methods for fuel assemblies are also currently underway. In a more distant future, the design and operation of small modular reactors also seem to be a path taken by the nuclear industry and by governments in order to supply clean and safe energy of a planet struggling with climate change and depletion of natural resources.

5 References

1. CEA, *Elecnucl - Les centrales nucléaires dans le monde*. 2019, CEA.
2. Garric, V., *Etude du gonflement par cavités d'un alliage d'aluminium irradié sous faisceau d'ions*, in *Matériaux, Mécanique, Génie Civil Electrochimie (2MGE)*. 2019, Université Grenoble Alpes.
3. WNA, W.N.A. *Nuclear Fuel and its Fabrication*. 2022; Available from: <https://www.world-nuclear.org/information-library/nuclear-fuel-cycle/conversion-enrichment-and-fabrication/fuel-fabrication.aspx>.
4. Strasser, A., *Fuel Fabrication Process Handbook Report*, A. International, Editor. 2005, ANTI 05-0008R
5. Kapusta, B. *Irradiation effects on 6061-T6 aluminium alloy used for JHR internal structures*. in *IGORR*. 2009.
6. Hu, J., et al., *Identifying suboxide grains at the metal-oxide interface of a corroded Zr-1.0%Nb alloy using (S)TEM, transmission-EBSD and EELS*. *Micron*, (0).
7. Bossis, P., et al. *In PWR Comprehensive Study of High Burn-up Corrosion and Growth Behavior of M5 and Recrystallized Low-Tin Zircaloy*. in *Zirconium in the Nuclear Industry: 15th International Symposium*. 2009.
8. Blat, M. and D. Noel. *Detrimental Role of Hydrogen on the Corrosion Rate of Zirconium Alloys*. in *Zirconium in the Nuclear Industry: 11th International Symposium*. 1996.
9. Blat, M., et al. *Contribution to a Better Understanding of the Detrimental Role of Hydrogen on the Corrosion Rate of Zircaloy-4 Cladding Materials*. in *Zirconium in the Nuclear Industry: 12th International Symposium*. 2000.
10. Kido, T. *A Study of Enhancement Uniform Corrosion of Zircaloy-4 Cladding During High-Burnup Operation in PWRs*. in *Environmental Degradation of Materials in the Nuclear Power System: 6th International Symposium*. 1993.
11. Tupin, M., et al., *Mechanism of corrosion of zirconium hydride and impact of precipitated hydrides on the Zircaloy-4 corrosion behaviour*. *Corrosion Science*, 2015. **98**: p. 478-493.
12. Iltis, X., F. Lefebvre, and C. Lemaignan. *Microstructure Evolution and Iron Redistribution in Zircaloy Oxide Layers: Comparative Effets of Neutron Irradiation Flux and Irradiation Damages*. in *Zirconium in the Nuclear Industry: 11th International Symposium*. 1996.
13. Iltis, X., F. Lefebvre, and C. Lemaignan, *Microstructural study of oxide layers formed on Zircaloy-4 in autoclave and in reactor part 11: Impact of the chemical evolution of intermetallic precipitates on their zirconia environment*. *Journal of Nuclear Materials*, 1995. **224**(2): p. 121-130.
14. Garzarolli, F., Y. Broy, and R.A. Busch. *Comparison of the Long-Time Corrosion Behaviour of Certain Zr Alloys in PWR, BWR and Laboratory Tests*. in *Zirconium in the Nuclear Industry: 11th International Symposium*. 1996.
15. Bossis, P., et al. *Comparison of the High Burn-Up Corrosion on M5 and Low Tin Zircaloy-4*. in *Zirconium in the Nuclear Industry: 14th International Symposium*. 2005. ASTM.
16. Garde, A.M., et al. *Corrosion Behavior of Zircaloy-4 Cladding with Varying Tin Content in High-Temperature Pressurized Water Reactors*. in *Zirconium in the Nuclear Industry: 10th International Symposium*. 1994.
17. Garner, G.L., B.A. Hilton, and E. Mader. *Performance of Alloy M5TM Cladding and Structure*. in *LWR Fuel Performance Meeting/Top Fuel*. 2007. San Francisco, CA, USA.
18. Verlet, R., et al., *Influence of light ion irradiation of the oxide layer on the oxidation rate of Zircaloy-4*. *Corrosion Science*, 2015. **98**(327-338).
19. Verlet, R., *Influence de l'irradiation et de la radiolyse sur la vitesse et les mécanismes de corrosion des alliages de zirconium*, in *Sciences et génie des matériaux*. 2015, Ecole Nationale Supérieure des Mines de Saint-Etienne.
20. Tupin, M., et al., *Effect of ion irradiation of the metal matrix on the oxidation rate of Zircaloy-4*. *Corrosion Science*, 2018. **136**: p. 28-37.
21. Colas, K., et al. *Microstructure Evolution in Ion-Irradiated Oxidized Zircaloy-4 Studied with Synchrotron Radiation Microdiffraction and Transmission Electron Microscopy*. in *Zirconium in the Nuclear Industry: 18th International Symposium*. 2018.
22. Lemaignan, C. and A.T. Motta, *Zirconium Alloys in Nuclear Applications*, in *Materials Science and Technology, A Comprehensive Treatment*, R.W. Cahn, P. Haasen, and E.J. Kramer, Editors. 1994, VCH: New York. p. 1-51.
23. Hauffe, K., *Oxidation of Metals*. 1965: Plenum Press.

24. Cox, B. and J.P. Pemsler, *Diffusion of oxygen in growing zirconia films*. Journal of Nuclear Materials, 1968. **28**: p. 73-78.
25. Jublot, M., et al. *Influence of the hydride precipitation on the corrosion kinetics of Zircaloy-4: Effect of the nanostructure and grain boundaries properties of zirconium oxide layer on the oxygen diffusion flux*. in *Zirconium in the Nuclear Industry: 18th International Symposium*. 2016. Hilton Head, SC, USA.
26. Garvie, R.C. and P.S. Nicholson, *Phase analysis in zirconia systems*. Journal of the American Ceramic Society, 1972. **55**(6): p. 303-305.
27. Yilmazbayhan, A., et al., *Structure of zirconium alloy oxides formed in pure water studied with synchrotron radiation and optical microscopy: relation to corrosion rate*. Journal of Nuclear Materials, 2004. **324**: p. 6-22.
28. Motta, A.T., et al. *Microstructure and growth mechanism of oxide layers formed on Zr alloys studied with micro-beam synchrotron radiation*. in *Zirconium in the Nuclear Industry: 14th International Symposium*. 2005.
29. Bechade, J.L., et al., *Studies of Zirconium Alloy Oxide Layers Using Synchrotron Radiation*. Materials Science Forum, 2000. **347**(1): p. 471-476.
30. Bossis, P., et al. *Multi-Scale Characterization of the Metal-Oxide Interface of Zirconium Alloys*. in *Zirconium in the Nuclear Industry: 12th International Symposium*. 2000.
31. Petigny, N., et al., *In situ XRD analysis of the oxide layers formed by oxidation at 743 K on Zircaloy-4 and Zr-1NbO*. Journal of Nuclear Materials, 2000. **280**: p. 318.
32. Kim, H.G., T.H. Kim, and Y.H. Jeong, *Oxidation characteristics of basal (0002) plane and prism (1120) plane in HCP Zr*. Journal of Nuclear Materials, 2002. **306**.
33. Vrtlikova, V., et al. *Corrosion of Zirconium Alloys*. in *International topical meeting on LWR fuel performance*. 2000. Park City, UT, USA.
34. Tupin, M., et al. *Understanding of corrosion mechanisms of zirconium alloys after irradiation: effect of ion irradiation of the oxide layers on the corrosion rate*. in *Zirconium in the Nuclear Industry: 17th International Symposium*. 2013.
35. Ziegler, J.F., J.P. Biersack, and M.D. Ziegler, *SRIM - The Stopping and Range of Ions in Matter*. 2008, SRIM Co.: Chester, MD.
36. Colas, K.B., *Fundamental Experiments on Hydride Reorientation in Zircaloy*, in *Department of Nuclear Engineering*. 2012, The Pennsylvania State University: University Park.
37. Colas, K.B., et al., *In-situ study of hydride precipitation kinetics and re-orientation in Zircaloy using synchrotron radiation*. Acta Materialia, 2010. **58**: p. 6565-6583.
38. Colas, K.B., et al. *Mechanisms of Hydride Reorientation in Zircaloy-4 Studied In-Situ in Zirconium in the Nuclear Industry: 17th International Symposium*. 2013. Hyderabad, India: ASTM.
39. Heo, Tae W., et al., *A phase-field model for hydride formation in polycrystalline metals: Application to δ -hydride in zirconium alloys*. Acta Materialia, 2019. **181**: p. 262-277.
40. Auzoux, Q., et al., *Hydride reorientation and its impact on ambient temperature mechanical properties of high burn-up irradiated and unirradiated recrystallized Zircaloy-2*. Journal of Nuclear Materials, 2017. **494**: p. 114-126.
41. CEA-Saclay, *Method of analyzing an image of hydrides in a metal alloy, in particular in a nuclear fuel cladding alloy*, E. Patent, Editor.
42. Colas, K., et al., *Characterization Techniques to Quantify Hydrogen Content, Hydride Morphology and Orientation on Unirradiated and Irradiated Zirconium Alloy Cladding*, in *2nd Zirconium Alloy Cladding/Hydride Workshop*. 2014: Jackson Hole, WY, USA.
43. Colas, K., *Des techniques de pointes aux grands instruments*. 2018.
44. Vargel, C., *Corrosion de l'aluminium*. Matériaux. 1999: Dunod.
45. Wefers, K. and C. Misra, *Oxides and Hydroxides of Aluminium*. 1987, ALCOA Laboratories.
46. Hart, R.K., *The formation of films on aluminium immersed in water*. Trans. Faraday Society, 1956. **53**: p. 1020-1025.
47. Griess, J.C., H.C. Savage, and J.L. English, *Effect of heat flux on the corrosion of aluminum by water. Part I: Experimental Equipment and Preliminary Results*. 1960, ORNL: Oak Ridge, TN, USA.
48. Wintergerst, M., et al., *Corrosion of the AlFeNi alloy used for the fuel cladding in the Jules Horowitz research reactor*. Journal of Nuclear Materials, 2009. **393**: p. 369-380.
49. Nabhan, D., et al., *Effects of pH, surface finish and thermal treatment on the corrosion of AlFeNi aluminum alloy. Characterization of oxide layers*. Journal of Nuclear Materials, 2015. **457**: p. 196-204.
50. L'Haridon-Quaireau, S., et al., *Effects of temperature and pH on uniform and pitting corrosion of aluminium alloy 6061-T6 and characterisation of the hydroxide layers*. Journal of Alloys and Compounds, 2020. **833**: p. 155146.

51. Chivot, J., *Solubilité de la boehmite et de la bayérite et spéciation de l'aluminium en solution aqueuse en fonction du pH et de la température*. 1997, CEA/FAR - CEREM.
52. Pawel, S.J., et al., *The development of a preliminary correlation of data on oxide growth on 6061 aluminium under ANS thermal-hydraulic conditions*. 1990, ORNL-TM (Oak Ridge National Laboratory).
53. Griess, J.C., H.C. Savage, and J.L. English, *Effect of heat flux on the corrosion of aluminum by water. Part III: Final Report on Tests Relative to the High-Flux Isotope Reactor*. 1961, ORNL: Oak Ridge, TN, USA.
54. Kim, Y.S., et al., *Aluminum cladding oxide growth prediction for high flux research reactors*. Journal of Nuclear Materials, 2020. **529**: p. 151926.
55. Griess, J.C., H.C. Savage, and J.L. English, *Effect of heat flux on the corrosion of aluminum by water. Part II: Influence of Water Temperature, Velocity and pH on Corrosion-Product Formation*. 1961, ORNL: Oak Ridge, TN, USA.
56. Pawel, R.E., et al., *The corrosion of 6061 aluminum under heat transfer conditions in the ANS corrosion test loop*. Oxidation of metals, 1991. **36**(1/2): p. 175-194.
57. Griess, J.C., H.C. Savage, and J.L. English, *Effect of heat flux on the corrosion of aluminum by water. Part IV: Tests relative relative to the advanced test reactor and correlation with previous results*. 1964, ORNL: Oak Ridge, TN, USA.
58. Nabhan, D., et al. *Effect of ion irradiation on the corrosion of an AlFeNi aluminium alloy*. in *International Group on Research Reactors IGORR-RRFM*. 2016. Berlin, Germany.
59. L'Haridon-Quaireau, S., *Etude des mécanismes de corrosion et des effets d'irradiation sur la corrosion d'un alliage d'aluminium utilisé dans les réacteurs nucléaires expérimentaux*, in *Chimie-Physique*. 2020, Université Paris-Saclay.
60. L'Haridon-Quaireau, S., et al., *Impact of ion and neutron irradiation on the corrosion of the 6061-T6 aluminium alloy*. Journal of Nuclear Materials, 2021. **553**: p. 153051.
61. Nabhan, D., *Etude de la corrosion aqueuse de l'alliage d'aluminium AlFeNi utilisé comme gainage de combustible nucléaire : effet de l'état de surface, du pH et d'une irradiation aux ions*. . 2014, Université Montpellier 2.
62. Buchanan, K., et al., *Atom Probe Tomography and Transmission Electron Microscope Analyses of Peak-Aged Al-Mg-Si-Cu alloys*, in *NuMat*. 2016: Montpellier, France.
63. Andersen, S.J., et al., *The crystal structure of the beta' phase in Al-Mg-Si alloys*. Acta Materialia, 1998. **46**: p. 3283-3298.
64. Vissers, R., et al., *The crystal structure of the beta' phase in Al-Mg-Si alloys*. Acta Materialia, 2007. **55**: p. 3815-3823.
65. Andersen, S., et al., *Crystal structure of the orthorhombic U₂-Al₄Mg₄Si₄ precipitate in the Al-Mg-Si alloy system and its relation to the beta' and beta'' phases*. Material Sciences Engineering, 2005. **390**: p. 127-138.
66. Andersen, S.J., et al., *The structural relation between precipitates in Al-Mg-Si alloys, the Al-matrix and diamond silicon, with emphasis on the trigonal phase U₁-MgAl₂Si₂*. Material Sciences Engineering, 2007. **444**: p. 157-169.
67. Flament, C., et al., *Stability of beta'' nano-phases in Al-Mg-Si(-Cu) alloy under high dose ion irradiation*. Acta Materialia, 2017. **128**: p. 64-76.
68. Weeks, J.R., *Effect of high thermal and high fast fluences on mechanical properties of type 6061 aluminum irradiated on HFBR*, in *ASTM STP 1046*. 1990. p. 441-452.
69. Kapusta, B., et al. *Mechanical characteristics of 5754-NET-O aluminum alloy irradiated up to high fluences : neutron spectrum and temperature effects*. in *1st Joint Meeting of the National Organization of Test, Research and Training Reactors And The International Group on Research Reactors*. 2005. Gaithersburg, USA.
70. Buchanan, K., et al., *Analysis of the metastable precipitates in peak-hardness aged Al-Mg-Si(-Cu) alloys with differing Si contents*. Acta Materialia, 2017. **132**: p. 209-221.
71. Marioara, C.D., et al., *Atomic model for GP-zones in 6082 Al-Mg-Si system*. Acta Materialia, 2001. **49**: p. 321-328.
72. Marioara, C.D., et al., *The influence of alloy composition on precipitates of the Al-Mg-Si system*. Metallurgical and Materials Transactions A, 2005. **36**: p. 691-702.
73. Garric, V., et al., *Correlation between quenching rate, mechanical properties and microstructure in thick sections of Al-Mg-Si(-Cu) alloys*. Materials Science and Engineering A, 2019: p. 253-261.
74. Lodgaard, L. and N. Ryum, *Precipitation of dispersoids containing Mn and/or Cr in Al-Mg-Si alloys*. Materials Science and Engineering A, 2000. **283**(1-2): p. 144-152.
75. Garric, V., et al., *Impact of the microstructure on the swelling of aluminum alloys: Characterization and modelling bases*. Journal of Nuclear Materials, 2021. **557**: p. 153273.

76. Farrell, K., *Effects of Structural Imperfections on Voids in Aluminium - Microstructure Impurity Effects on Void Formation Characteristics in Neutron Irradiated Aluminium*. 1971, Oak Ridge National Laboratory.
77. Farrell, K., *Assessment of Aluminum Structural Materials for Service within the ANS Reflector Vessel*. 1995, Oak Ridge National Laboratory.
78. Petit, T., et al., *Impact of machine stiffness on "pop-in" crack propagation instabilities*. Engineering Fracture Mechanics, 2018. **202**: p. 405-422.
79. Petit, T., et al., *Effect of hardening on toughness captured by stress-based damage nucleation in 6061 aluminum alloy*. Acta Materialia, 2019. **180**: p. 349-365.
80. Petit, T., *Compréhension et modélisation d'essais de ténacité avec pop-in : application à l'aluminium 6061-T6 et influence de l'irradiation neutronique*, in *Sciences et Génie des Matériaux*. 2018, Université de recherche Paris Sciences et Lettres.

6 Appendices

6.1 Detailed Curriculum Vitae

Curriculum Vitae

Kimberly COLAS

Née le 6 Décembre 1985
Nationalité : France USA
Titulaire du permis B, 2 enfants



DEN/DANS/DMN/SEMI/LM2E
91191 Gif-sur-Yvette
+33-7-85-62-95-80
kimberly.colas@cea.fr

Formation

- **2009-2012** Pennsylvania State University, Doctor of Philosophy Nuclear Engineering (State College PA USA). Date d'obtention du diplôme: Aout 2012 (soutenance: Mai 2012, directeur de these: Dr Arthur Motta, jury : Dr Marc Daymond, Dr Jack Brenizer, Dr Long-Qin Chen, Dr Raymond Howell)
- **2007-2009** Pennsylvania State University, Master of Science Nuclear Engineering (State College PA USA)
- **2005-2009** Ecole Centrale de Lyon, diplôme d'Ingénieur (promotion 2008), (Lyon, France)
- **2003-2005**. Classe Préparatoire Math Sup et Spé filière MP au Lycée Henri IV (Paris 5^{ème}, France)
- **2003**. Diplôme du Baccalauréat Général, série Scientifique option Mathématiques Mention très bien (Lycée Victor Duruy, Paris 7^{ème}, France)

Collaborations internationales :

- Collaboration avec groupes de recherche Argentins et Canadiens sur la cinétique de précipitation des hydrures de zirconium étudiés par rayonnement synchrotron : papier résultant de la collaboration : **2010: In situ study of hydride precipitation kinetics and re-orientation in Zircaloy using synchrotron radiation**, Colas, K.B. ; Motta, A.T.; Almer, J.D.; Daymond, M.R.; Kerr, M.; Banchik, A.D.; Vizcaino, P.; Santisteban, J.R. , *Acta Materialia*, v 58, n 20, p 6575-6583, December 2010
- Collaboration avec les industriels du nucléaire dans le Nuclear Fuel Industry Research Program (NFIR) coordonné par l'EPRI depuis 2013 : meetings semi-annuels, rapports semi-annuels. Production scientifique associée : **2017: Hydride reorientation and its impact on ambient temperature mechanical properties of high burn-up irradiated and unirradiated recrystallized Zircaloy-2 nuclear fuel cladding with an inner liner**, Q. Auzoux, P. Bouffieux, A. Machiels, S. Yagnik, B. Bourdilliau, C. Mallet, N. Mozzani, K. Colas, *Journal of Nuclear Materials*, v494 pp. 114-126

Activités liées à la recherche et à l'enseignement:

- 2016 Journées des Sciences de l'Ingénieur au Féminin : présentation du métier et du parcours de chercheuses auprès des jeunes collégiennes et lycéennes.
- Expert niveau 2 au CEA depuis 01/01/2018 dans le domaine « Matériaux, physique du solide & des semi-conducteurs » avec la spécialité « Matériaux nucléaires ».
- 2019-présent Conseil d'administration de la SF2M
- 2021-présent Mentore dans l'association Femmes&Sciences
- 2022 Membre de l'Association des Femmes Dirigeantes dans l'Enseignement Supérieur et la Recherche (AFDESRI)

6.2 List of publications and communications

Publications avec referee:

- **2022 : Development of a compact alpha and beta camera for dismantlement applications**, S. Leblond, P. Fichet, R. Laumonier, S. Billon, P. Sardini, K. Colas, *Journal of Radioanalytical and Nuclear Chemistry*, <https://doi.org/10.1007/s10967-021-08172-2>
- **2021 : Impact of ion and neutron irradiation on the corrosion of the 6061-T6 aluminum alloy**, S. L'Haridon-Quaireau, K. Colas, B. Kapusta, B. Verhaeghe, M. Loyer-Prost, G. Gutierrez, D. Gosset, S. Delpech, *Journal of Nuclear Materials*, v553, pp. 153051
- **2021 : Impact of the microstructure on the swelling of aluminum alloys: Characterization and modelling bases**, V. Garric, K. Colas, P. Donnadiou, M. Loyer-Prost, F. Leprêtre, V. Clouté-Cazalaa, B. Kapusta, *Journal of Nuclear Materials*, v557, pp. 153273
- **2020 : Effects of temperature and pH on uniform and pitting corrosion of aluminum alloy 6061-T6 and characterization of the hydroxide layers**, S. L'Haridon-Quaireau, M. Laot, K. Colas, B. Kapusta, S. Delpech, D. Gosset, *Journal of Alloys and Compounds*, v833, pp. 155146
- **2019 : A phase-field model for hydride formation in polycrystalline metals: Application to δ -hydride in zirconium alloys**, T-W. Heo, K. Colas, A. Motta, L-Q. Chen, *Acta Materialia*, v181, pp. 262-277
- **2019 : Effect of hardening on toughness captured by stress-based damage nucleation in 6061 aluminum alloy**, T. Petit, J. Besson, C. Ritter, K. Colas, L. Helfen, T. Morgeneyer, *Acta Materialia*, In Press, Journal Pre-Proof, September 2019
- **2019 : Correlation between quenching rate, mechanical properties and microstructure in thick sections of Al-Mg-Si(-Cu) alloys**, V. Garric, K. Colas, P. Donnadiou, G. Renou, S. Urvoy, B. Kapusta, *Materials Science and Engineering A*, v753, pp253-261
- **2018 : Microstructure Evolution in Ion-Irradiated Oxidized Zircaloy-4 Studied with Synchrotron Radiation Microdiffraction and Transmission Electron Microscopy**, K. Colas, R. Verlet, M. Tupin, Z. Cai, K. Wolski, M. Jublot, P. Bossis, *Zirconium in the Nuclear Industry*, ASTM STP 1597 (2018)

- **2018 : Understanding of Corrosion Mechanisms after Irradiation: Effect of Ion Irradiation of the Oxide Layers on the Corrosion Rate of M5**, M. Tupin, R. Verlet, K. Wolski, S. Miro, G. Baldacchino, M. Jublot, K. Colas, P. Bossis, A. Ambard, D. Kaczorowski, M. Blat-Yrieix, I. Idarraga, *Zirconium in the Nuclear Industry*, ASTM STP 1597 (2018)
- **2018 : Effect of ion irradiation of the metal matrix on the oxidation rate of Zircaloy-4**, M. Tupin, R. Verlet, K. Colas, M. Jublot, G. Baldacchino, K. Wolski, *Corrosion Science*, v136 pp. 28-37.
- **2017: Hydride reorientation and its impact on ambient temperature mechanical properties of high burn-up irradiated and unirradiated recrystallized Zircaloy-2 nuclear fuel cladding with an inner liner**, Q. Auzoux, P. Bouffieux, A. Machiels, S. Yagnik, B. Bourdilliau, C. Mallet, N. Mozzani, K. Colas, *Journal of Nuclear Materials*, v494 pp. 114-126
- **2017: Stability of β'' nano-phases in Al-Mg-Si(-Cu) alloy under high dose ion irradiation**, C. Flament, J. Ribis, J. Garnier, Y. Serruys, F. Leprêtre, A. Gentils, C. Baumier, M. Descoins, D. Mangelinck, A. Lopez, K. Colas, K. Buchanan, P. Donnadiou, A. Deschamps, *Acta Materialia*, v128, pp64-76
- **2017: Analysis of the metastable precipitates in peak-hardness aged Al-Mg-Si(-Cu) alloys with differing Si contents**, K. Buchanan, K. Colas, J. Ribis, A. Lopez, J. Garnier, *Acta Materialia*, v132, pp209-221
- **2016: Identification of monoclinic θ -phase dispersoids in a 6061 aluminum alloy**, K. Buchanan, J. Ribis, J. Garnier, K. Colas, *Philosophical Magazine Letters*, v96, issue 4, pp 121-131
- **2015: Influence of light ion irradiation of the oxide layer on the oxidation rate of Zircaloy-4**, R. Verlet, M. Tupin, G. Baldacchine, K. Wolski, S. Miro, D. Gosset, K. Colas, M. Jublot, F. Jomard, *Corrosion Science*, v98 pp 327-337
- **2014: Effects of pH, surface finish and thermal treatment on the corrosion of AlFeNi aluminum alloy. Characterization of oxide layers**, D. Nabhan, B. Kapusta, P. Billaud, K. Colas, D. Hamon, N. Dacheux, *Journal of Nuclear Materials*, v 457 pp197-204
- **2013: Mechanisms of Hydride Reorientation in Zircaloy-4 Studied in Situ**, K. B. Colas, A. T. Motta, M. R. Daymond, J. D. Almer, *Zirconium in the Nuclear Industry*, ASTM STP 1543 (2013).
- **2013: Effect of thermo-mechanical cycling on zirconium hydride reorientation studied in situ with synchrotron X-ray diffraction**, K. B. Colas, A. T. Motta, M. R. Daymond, J. D. Almer, *Journal of Nuclear Materials* 440 (2013) 586-595
- **2011: Hydride platelet reorientation in Zircaloy studied with synchrotron radiation diffraction**, Colas, K. B., Motta, A.T.; Daymond, M. R.; Kerr, M.; Almer, J. D. , *Journal of ASTM International*, v 8, n 1, January 2011
- **2010: In situ study of hydride precipitation kinetics and re-orientation in Zircaloy using synchrotron radiation**, Colas, K.B. ; Motta, A.T.; Almer, J.D.; Daymond, M.R.; Kerr, M.; Banchik, A.D.; Vizcaino, P.; Santisteban, J.R. , *Acta Materialia*, v 58, n 20, p 6575-6583, December 2010
- **2009: Fracture of a minority phase at a stress concentration observed with synchrotron X-ray diffraction**, Kerr, M.; Daymond, M.R.; Holt, R.A.; Almer, J.D.; Stafford, S.; Colas, K.B., *Scripta Materialia*, v 61, n 10, p 939-942, November 2009.

Publications sans referee:

- **2016 : Effect of ion irradiation on the corrosion on an AlFeNi aluminum alloy**, D. Nabhan, B. Kapusta, K. Colas, N. Dacheux, *Proceedings of IGORR-RRFM 2016 conference*, Berlin, Germany, Mars 13-17, 2016
- **2011: Hydride behavior in Zircaloy-4 during Thermomechanical Cycling**, Colas, K. B., , A. T. Motta, M. R. Daymond, Cai, Z., *15th International Conference on Environmental Degradation of Materials in Nuclear Power Systems*, Colorado Springs, Août 2011

Congrès:

- **2022** Co-auteur d'une presentation orale à DEM 2021, Septembre 2021, Avignon, France
- **2019** Co-auteur d'une presentation orale à 6th International Conference on Computational Modeling of Fracture and Failure of Materials and Structures, Juin 2019, Braunschweig, Allemagne
- **2019** Co-auteur d'une présentation orale et d'un poster à l'ASTM International Symposium on Zirconium in the Nuclear Industry, Manchester, UK
- **2019** Co-auteur de deux présentations à International Group on Research Reactors, Jordanie
- **2018** Co-auteur d'un poster à Hotlab, Helsinki, Finlande
- **2018** Co-auteur de deux présentations à International Conference on Aluminum Alloys, Montreal, Canada
- **2017** Co-auteur d'une présentation orale à International Group on Research Reactors IGORR, Sydney, Australie
- **2017** Co-auteur d'une présentation orale à : 14th International conference on Fracture, 2017, Rhodes, Grèce.
- **2016** Co-auteur d'une presentation orale à Numat 2016, Montpellier, France
- **2016** Présentation orale à l'ASTM 18th International Symposium on Zirconium in the Nuclear Industry, Hilton Head, SC, USA
- **2016** Présentation orale à International Group on Research Reactors IGORR-RRFM conference, Berlin, Allemagne
- **2014** Co-auteur d'une présentation orale au 51st annual meeting of HOTLAB, Baden, Suisse (présentateur B. Verhaeghe)
- **2014** Présentation orale à l'ASTM 2nd zirconium alloy cladding/hydride workshop, Jackson Hole, WY, USA
- **2013** Présentation orale à l'ASTM 17th International Symposium on Zirconium in the Nuclear Industry, Hyderabad, India
- **2013** Présentation orale au 8ème Colloque "Matériaux, Mécanique, Microstructure", INSTN - CEA Saclay
- **2012** Poster à NuMat 2012, Osaka, Japan
- **2011** Présentation orale à la 15ème conference internationale de l'Environmental Degradation of Materials in Nuclear Power Systems, Colorado Springs, CO, USA
- **2011** Co-auteur d'une présentation orale au 140ème colloque du TMS, San Diego, CA, USA (présentateur A. Motta)
- **2010** Présentation orale à l'ASTM 16th International Symposium on Zirconium in the Nuclear Industry, Chengdu, Chine

- **2008** Présentation orale à la 7ème rencontre internationale du MRS Brésilien, Guaruja, Brésil

Brevet:

- **2016** Dispositif et procédé de fabrication d'échantillons pour SAT à partir d'une plaque fin BD16640

Ouvrage:

- **2018** : Corrosion et protection des matériaux à haute température, Tome 2, Commission Haute Température du CEFRACOR, Presses des MINES, collection Sciences de la matière, *Chapitre : Des grands instruments aux techniques de pointe* pp. 157-171.

Prix et Distinctions

- **2019** Médaille Jean Rist de la Société Française de Métallurgie et de Matériaux (SF2M)
- **2019** Prix Jacques Gaussens de la Société Française de l'Energie Nucléaire (SFEN)
- **2010** Obtention d'une bourse de la société des Femmes dans la Science et l'Ingénierie (WISE)
- **2009** Prix Fem'energia pour les femmes dans le Nucléaire d'EDF et WiN, Catégorie Bac +4/5
- **2008-2009** Obtention de deux bourses du Centre International pour la Recherche en Matériaux (ICMR)
- **2009-2011** Appartenance à Alpha Nu Sigma, société honorifique d'ingénieurs en nucléaire
- **2008-2011** Appartenance à Tau Beta Pi, société honorifique d'ingénieurs

Expériences d'encadrement et production scientifique associée

Thèses :

- **2017-2020** Encadrement de la thèse de Sarah L'Haridon-Quaireau (encadrement à 100%), direction : S. Delpech, INPO « Etude de la corrosion de l'alliage d'aluminium 6061-T6 utilisé dans les réacteurs nucléaires de recherche ». Production scientifique associée :
 - 2021 : Impact of ion and neutron irradiation on the corrosion of the 6061-T6 aluminum alloy, S. L'Haridon-Quaireau, K. Colas, B. Kapusta, B. Verhaeghe, M. Loyer-Prost, G. Gutierrez, D. Gosset, S. Delpech, Journal of Nuclear Materials, v553, pp. 153051
 - Effect of ion irradiation on aluminum hydroxide on an Al-Mg-Si alloy, L'Haridon-Quaireau, S., Colas, K., Kapusta, B. ; Delpech, S., Verhaeghe, B., Cloute-Cazalaa, V., Gutierrez, G., Loyer-Prost, M., Gosset, D. ; Conférence : International Group on Research Reactors, Jordanie, mars 2019
 - Study of the influence of initial pH on the aqueous corrosion of an Al-Mg-Si alloy at 70°C, International Conférence on Aluminum Alloys, ICAA16, 2018, Montréal, Canada
- **2016-2019** Co-encadrement de la thèse de Victor Garric avec B. Kapusta (encadrement à 50%), direction : P. Donnadiou Université de Grenoble SiMaP « Etude du gonflement par cavités de l'alliage 6061-T6 irradié sous faisceau d'ions » → Post doc au GPM, Rouen. Production scientifique associée :
 - 2021 : Impact of the microstructure on the swelling of aluminum alloys: Characterization and modelling bases, V. Garric, K. Colas, P. Donnadiou, M. Loyer-Prost, F. Leprêtre, V. Clouté-Cazalaa, B. Kapusta, Journal of Nuclear Materials, v557, pp. 153273
 - The influence of the thermomechanical process on the behavior of 6xxx aluminum alloys under ion irradiation, Garric, V., Colas, K., Donnadiou, P., Kapusta, B. ; Conférence : International Group on Research Reactors, Jordanie, mars 2019

- 2019 : Correlation between quenching rate, mechanical properties and microstructure in thick sections of Al-Mg-Si(-Cu) alloys, V. Garric, K. Colas, P. Donnadiou, G. Renou, S. Urvoy, B. Kapusta, *Materials Science and Engineering A*, v753, pp253-261
- **2015-2018** Co-encadrement de la thèse de Tom Petit avec C.Ritter (encadrement à 50%), collaboration avec les Mines Paris (T. Morgeneyer, J. Besson) « Evolution des propriétés de traction et de ténacité du métal de base d'un alliage d'aluminium 6061-T6 avec l'irradiation et modélisation d'essais avec pop-in » →Embauché comme ingénieur de recherche au CEA. Production scientifique associée :
 - 2019 : Effect of hardening on toughness captured by stress-based damage nucleation in 6061 aluminum alloy, T. Petit, J. Besson, C. Ritter, K. Colas, L. Helfen, T. Morgeneyer, *Acta Materialia*, In Press, Journal Pre-Proof, September 2019
 - Impact of heat treatment of an Al-Mg-Si alloy on instabilities during crack propagation in fracture toughness tests, T. Petit, C. Ritter, K. Colas, J. Besson, T. Morgeneyer, Conférence: 14th International conference on Fracture, 2017, Rhodes, Grèce.
 - Effect of hardening on toughness : stress-dependent nucleation in the case of 6061 aluminum, T. Petit, J. Besson, C. Ritter, K. Colas, L. Helfen, T. Morgeneyer, Conférence: 6th International Conference on Computational Modeling of Fracture and Failure of Materials and Structures, Juin 2019, Braunschweig, Allemagne.
- **2013-2016** Co-encadrement avec J. Garnier et J. Ribis du post-doc de Karl Buchanan (encadrement à 50%) « Study of the impact of silicon content on mechanical behavior and irradiation swelling of aluminum alloy 6061 – T6 » →Embauché comme ingénieur chez Framatome. Production scientifique associée :
 - 2017: Analysis of the metastable precipitates in peak-hardness aged Al-Mg-Si(-Cu) alloys with differing Si contents, K. Buchanan, K. Colas, J. Ribis, A. Lopez, J. Garnier, *Acta Materialia*, v132, pp209-221
 - 2016: Identification of monoclinic θ -phase dispersoids in a 6061 aluminum alloy, K. Buchanan, J. Ribis, J. Garnier, K. Colas, *Philosophical Magazine Letters*, v96, issue 4, pp 121-131
 - Atom probe tomography and transmission electron microscope analysis of peak-aged Al-Mg-Si-Cu alloys K. Buchanan, K. Colas, J. Ribis, A. Lopez, J. Garnier, CEA, Conférence NuMat, Montpellier, France
- **2012-2015** Participation à l'encadrement de la thèse de R. Verlet avec M. Tupin (encadrement à 30%) « Influence de l'irradiation et de la radiolyse sur la vitesse et les mécanismes de corrosion des alliages de zirconium » →Embauché comme ingénieur à EDF. Production scientifique associée :
 - 2015: Influence of light ion irradiation of the oxide layer on the oxidation rate of Zircaloy-4, R. Verlet, M. Tupin, G. Baldacchine, K. Wolski, S. Miro, D. Gosset, K. Colas, M. Jublot, F. Jomard, *Corrosion Science*, v98 pp 327-337
 - 2018 : Microstructure Evolution in Ion-Irradiated Oxidized Zircaloy-4 Studied with Synchrotron Radiation Microdiffraction and Transmission Electron Microscopy, K. Colas, R. Verlet, M. Tupin, Z. Cai, K. Wolski, M. Jublot, P. Bossis, *Zirconium in the Nuclear Industry*, ASTM STP 1597 (2018)
 - 2018 : Understanding of Corrosion Mechanisms after Irradiation: Effect of Ion Irradiation of the Oxide Layers on the Corrosion Rate of M5, M. Tupin, R. Verlet, K. Wolski, S. Miro, G. Baldacchino, M. Jublot, K. Colas, P. Bossis, A. Ambard, D. Kaczorowski, M. Blat-Yrieix, I. Idarraga, *Zirconium in the Nuclear Industry*, ASTM STP 1597 (2018)
- **2012-2014** Co-encadrement avec B. Kapusta de la thèse de Diana Nabhan (encadrement à 50%) en collaboration avec l'Université de Montpellier « Etude de la corrosion aqueuse de l'alliage d'aluminium AlFeNi utilisé comme gainage de combustible nucléaire » →Professeur de Physique-Chimie à l'Université Américaine du Liban. Production scientifique associée :
 - 2014: Effects of pH, surface finish and thermal treatment on the corrosion of AlFeNi aluminum alloy. Characterization of oxide layers, D. Nabhan, B. Kapusta, P. Billaud, K. Colas, D. Hamon, N. Dacheux, *Journal of Nuclear Materials*, v 457 pp197-204
 - Study of the impact of ion irradiation on the corrosion kinetics and the oxide layer microstructure of AlFeNi Aluminum alloy, Conférence International Group on Research Reactors, IGORR-RRFM, Berlin, mars 2016

Stages M2:

- **2019** Stage de Sami Meddeb (Phelma INP Grenoble, 6 mois). Production scientifique associée :
 - European APT conference : Poster, Rouen 2019
- **2018** Stages de Matthew Grimes (Master EMINE, INP Grenoble, 6 mois)
- **2016** Stages de Sarah l'Haridon-Quaireau (Mines Saint-Etienne, 6 mois), de Thomas Soyez (Master MNE, INSTN, 6 mois)
- **2014** Stages de Florence Jacques (Centrale Lyon, 6 mois)